Interaction of Charge Carriers with Defects at Interfaces and Grain Boundaries in Compound Semiconductors

by

Abhinav Chikhalkar

A Dissertation Presented in Partial Fulfillment
of the Requirements for the Degree
Doctor of Philosophy

Approved April 2021 by the
Graduate Supervisory Committee:

Richard R. King, Chair
Christiana Honsberg
Nathan Newman
Sefaattin Tongay

ARIZONA STATE UNIVERSITY

May 2021

ABSTRACT

Realization of efficient, high-bandgap photovoltaic cells produced using economically viable methods is a technological advance that could change the way we generate and use energy, and thereby accelerate the development of human civilization. There is a need to engineer a semiconductor material for solar cells, particularly multijunction cells, that has high (1.6-2.0 eV) bandgap, has relatively inactive defects, is thermodynamically stable under normal operating conditions with the potential for cost-effective thin-film growth in mass production.

This work focuses on a material system made of gallium, indium, and phosphorus – the ternary semiconductor GaInP. GaInP based photovoltaic cells in single-crystal form have demonstrated excellent power conversion efficiency, however, growth of single-crystal GaInP is prohibitively expensive. While growth of polycrystalline GaInP is expected to lower production costs, polycrystalline GaInP is also expected to have a high density of electronically active defects, about which little is reported in scientific literature. This work presents the first study of synthesis, and structural and optoelectronic characterization of polycrystalline GaInP thin films.

In addition, this work models the best performance of polycrystalline solar cells achievable with a given grain size with grain-boundary/surface recombination velocity as a variable parameter. The effects of defect characteristics at the surface and layer properties such as doping and thickness on interface recombination velocity are also modeled.

Recombination velocities at the free surface of single-crystal GaInP and after deposition of various dielectric layers on GaInP are determined experimentally using

time-resolved photoluminescence decay measurements. In addition, experimental values of bulk lifetime and surface recombination velocity in well-passivated single crystal AlInP-GaInP based double heterostructures are also measured for comparison to polycrystalline material systems.

A novel passivation method – aluminum-assisted post-deposition treatment or Al-PDT – was developed which shows promise as a general passivation and material improvement technique for polycrystalline thin films. In the GaInP system, this aluminum post-deposition treatment has demonstrated improvement in the minority carrier lifetime to 44 ns at 80 K. During development of the passivation process, aluminum diffusivity in GaInP was measured using TEM-EDS line scans. Introduction, development, and refinement of this novel passivation mechanism in polycrystalline GaInP could initiate the development of a new family of passivation treatments, potentially improving the optoelectronic response of other polycrystalline compound semiconductors as well.

Dedicated to Sharon, Avinash, Daaji, Aai and Madhulika.

Aaji & Aaba, you will always be remembered...

ACKNOWLEDGEMENTS

First and foremost, I would like to thank Dr. Richard King, for giving me the opportunity to explore this exciting field. Thank you for believing in me, guiding me, and sometimes pushing me. Thank you for giving me the freedom to explore some of my crazy ideas. Hopefully, this work lays the platform for many more exciting research opportunities.

I would like to thank my committee: Prof. Christiana Honsberg, Prof. Nathan Newman, and Prof. Sefaattin Tongay. Their inputs and suggestions have helped improve the quality of this dissertation.

I would like to thank my funding agency QESST. QESST stands for Quantum Energy and Sustainable Solar Technology. It is an NSF-DOE funded Engineering Research Center led by Arizona State University. Started in 2009, QESST has created a unique environment to facilitate development of next generation solar cells. Through collaborations with research groups from all over the world, QESST has helped me appreciate the role of various components that go into deployment of solar cell technology: from scientific research to educational outreach. QESST also facilitated engagement with fellow research scholars working on solar technologies and has created an excellent community.

I have been lucky to have colleagues in the King lab and the Solar Power Lab (SPL) that I could call friends. I cannot thank Bill Dauksher at SPL enough. His dedication and discipline at work has helped me carry out experiments in safe and timely manner. Bill, you make SPL so much more productive.

I would also like to acknowledge our collaborators, for providing samples to characterize (Dr. Eric Armour from Veeco Instruments, research group of Dr. Shafarman

at University of Delaware, and Dr. Javey at UC Berkeley). Collaborative study with research groups of Dr. Ponce and Dr. Smith at ASU for specialized characterization methods involving cathodoluminescence spectroscopy and transmission electron microscopy respectively, helped develop a deeper understanding of the defect passivation mechanisms. I would also like to thank Dr. Michael Goryll, who helped me set up the admittance spectroscopy tool, and helped understand and analyze the admittance spectroscopy data.

I learnt basics of molecular beam epitaxy handling and maintenance through Dr. Nikolai Faleev, Dr. Chaomin Zhang, Dr. Aymeric Maros and Prof. Nathan Newman. I am extremely grateful for their patience with me through the learning process.

Finally, I would like to thank my friends and family who have been pillars of support through this fascinating journey of Ph.D. research.

TABLE OF CONTENTS

Page

LIST OF TABLES

LIST OF FIGURES

Figure Page

CHAPTER 1

INTRODUCTION

1.1. Motivation

Electricity is one of the most versatile forms of energy. It is a low-entropy form of energy which can be converted into other forms of energy with minimal losses. Electricity can also be transported over large distances with high efficiency. Therefore, the ability to harness electricity is observed to be directly correlated to the development of economic productivity and quality of life in communities, and indeed of countries and civilizations. Access to abundant and inexpensive electric power not only helps widespread deployment

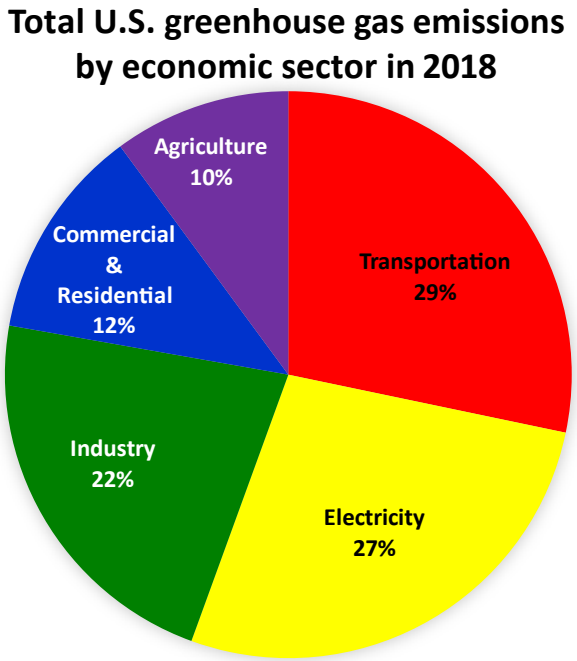

Fig. 1.1 Total greenhouse gas emissions in the United States by economic sector in 2018, as reported by United States Environment Protection Agency. Percentages may not add up to 100% due to independent rounding.

of current technology but also enables development of novel technology to improve our lives further.

There is an increasing consensus that humans need to find sustainable ways of development while reducing the greenhouse gas emissions in the atmosphere. The contribution of different economic sectors in United States towards greenhouse gas emissions in the year 2018 is summarized in Fig. 1.1. According to the United States Environmental Protection Agency (EPA) report of 2018 [1], electricity production generates about 27% of the total greenhouse gas emissions of the country. One of the most promising technologies for inexpensive and sustainable electricity generation is photovoltaics, or solar cell technology. Cost of electricity generation using solar cells is steadily decreasing over the past three decades. The generation costs have increasingly become competitive with other sources of electricity generation. This has led to an increase

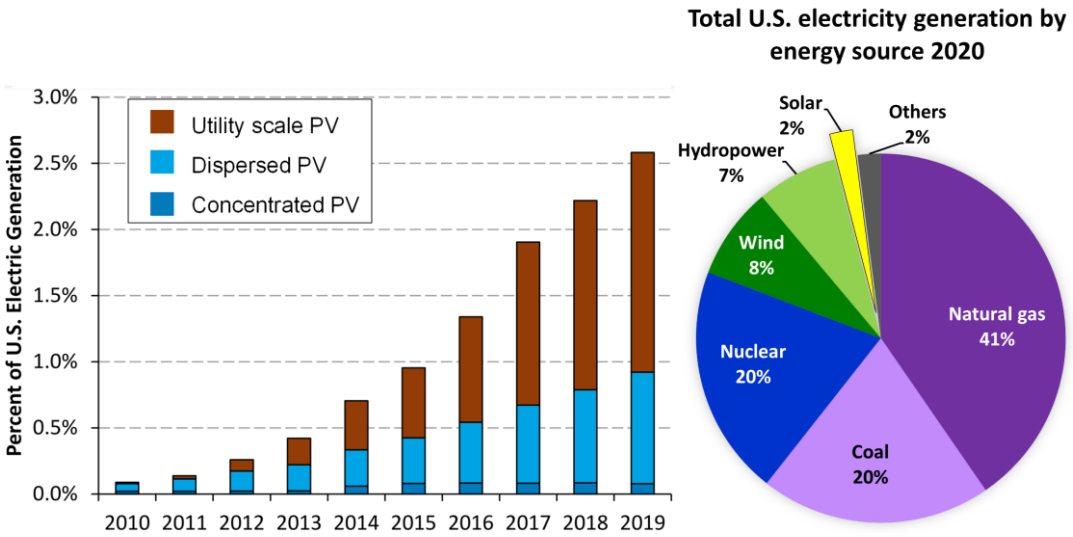

Fig. 1.2. (left) Rise in the share of PV technology for electricity generation in the United States from 2010 to 2019, and (right) pie chart summarizing the total electricity generation in the United States by energy source in 2020.

in acceptance of solar cell technology as one of the preferred sources of electricity generation in many communities. As shown in Fig. 1.2, share of solar technology in the United States electricity generation has increased from less than 0.1% in 2010 to over 2.5% in 2020 [2].

Approximately 95% of the solar cells currently used for electricity production have silicon as the primary light absorber semiconductor. The manufacturing cost of silicon-based solar cells has been steadily falling over the past 30 years to the point that it is currently one of the most cost-effective ways to generate electricity in many applications. According to the U.S. solar photovoltaic system cost benchmark published in 2021 by National Renewable Energy Laboratory [3], solar module production costs account for approximately 30% of the total cost of electricity from solar power plants at utility scale (Fig. 1.3). Other factors like land costs, installation costs, inverter costs, and operation and maintenance costs account for the remaining 70%. Many of these secondary costs scale proportionately with the area of solar cells required to produce a unit of power.

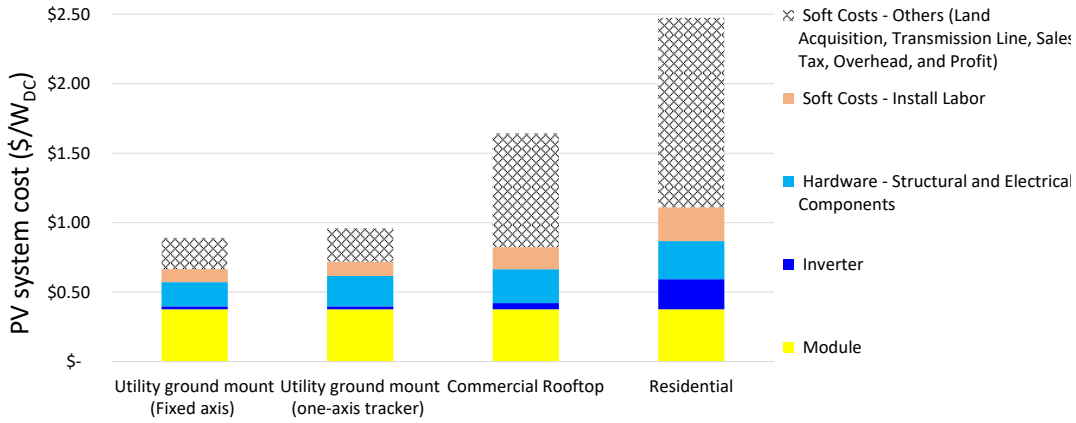

Fig. 1.3. Breakdown of the cost of electricity from solar power plants at residential, commercial and utility scale (with fixed axis and one axis tracker)

Increasing the efficiency of solar cells results in more electricity production from the same area of solar cells. This reduces the area required to generate a unit of electric power. This reduces the module costs as well as the other soft costs that scale with area of the power plant. Therefore, increasing solar cell efficiency has a strong impact on the overall cost of electricity.

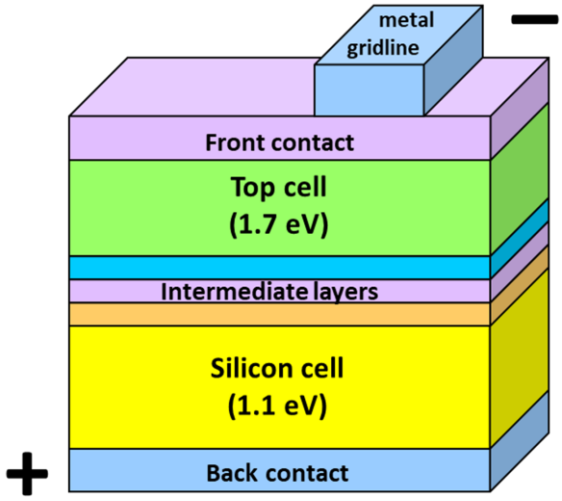

Fig. 1.4. Schematic of a typical 2-junction silicon-based tandem solar cell architecture.

Silicon based single-junction solar cells are fast approaching their maximum possible efficiency limits. While silicon is excellent at converting the near infrared part of the solar spectrum to electricity, thermalization losses limit its conversion efficiency of the ultraviolet and visible part of the spectrum. One device architecture to improve the conversion efficiency of high energy photons is a multijunction solar cell having a top cell with a wide-bandgap absorber layer positioned over a silicon bottom cell (Fig. 1.4). This type of solar cell that has two subcells with different absorber layers stacked on top of each other is called a tandem solar cell, a special case of multijunction cells which have 2 or more component cells. It is attractive to make the bottom subcell of the tandem solar cell

out of silicon since silicon cell technology is highly evolved and has reached a low cost in manufacturing. Scientists are still searching for a semiconductor material with the appropriate bandgap and electronic quality to make the top cell. The top cell needs to effectively convert the visible and ultraviolet part of sunlight to electricity, to be inexpensive to fabricate and to be stable and operational for over 25 years in ambient environmental conditions. Some candidate materials considered for the top cell of the tandem solar cell either degrade over time or are too expensive to fabricate.

GaInP in its single-crystalline form is also being studied for use in indoor low-power harvesting applications. With the advent of the internet of things (IoT) we are surrounded by low-power electronic devices that need to be charged regularly. A photovoltaic device that effectively converts ambient indoor light to electricity can help power such devices. This would not only improve effectiveness and convenience of using these devices but could also enable development of novel devices that do not require regular maintenance, make our everyday lives easier, and improve the security and safety of our homes, and commercial and public buildings.

Ambient indoor light is usually dominated by shorter wavelengths than the spectrum from the sun. GaInP and its aluminum alloys (called AlGaInP), with their higher bandgap than the conventional silicon or GaAs based photovoltaic cells, are prime candidates for converting this indoor light into electric power.

1.2. Overview of this dissertation

This dissertation explores several potential material systems that could be used to make the top cell. One material system worked on in detail is a semiconductor compound formed by the elements gallium, indium, and phosphorus, called gallium indium phosphide ($Ga_xIn_{1-x}P_2$). GaInP based solar cells in their single-crystal form have demonstrated high efficiency at converting visible part of spectrum to electricity. The highest power conversion efficiency reported for GaInP-based solar cell is 20.8% [4] by Geisz *et. al.* But it is expensive to fabricate single crystalline layers of GaInP. Polycrystalline GaInP is expected to be significantly less expensive to fabricate, but before this work had not been studied in detail. Single crystal GaAs and InP based solar cells have demonstrated a power conversion efficiency of 27.6% [5] and 21% [6] respectively. This has encouraged scientists to explore these binary compounds in their polycrystalline form, demonstrating a power conversion efficiency of over 19.5% using GaAs with less than 4 mm grain size [7] and nearly 12.3% efficiency using InP [8] with less than 50 microns grain

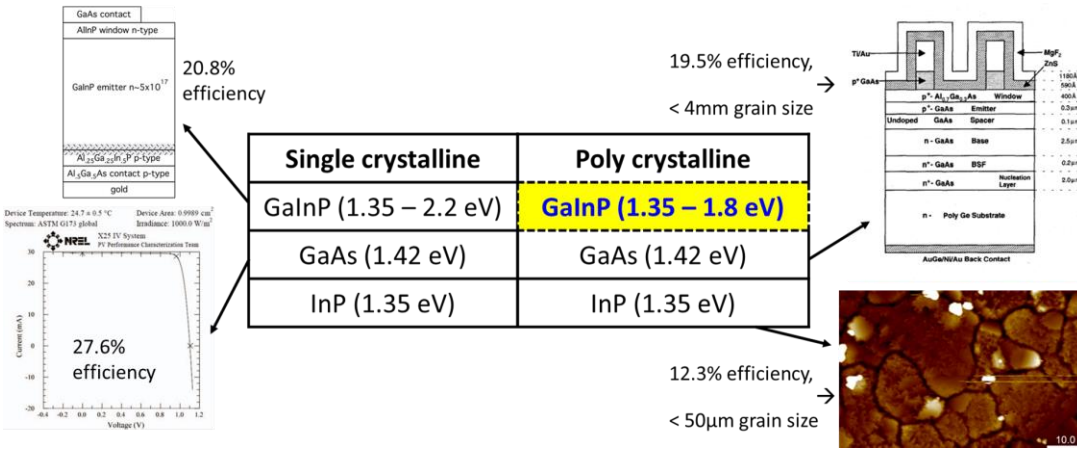

Fig. 1.5 Best demonstrated solar cell efficiencies of GaInP, GaAs, and InP in their single crystalline and polycrystalline form. Author could not find a report demonstrating polycrystalline a GaInP-based solar cell.

size (Fig. 1.5). Polycrystalline GaInP also would have much larger density of defects than the single-crystal form, due to the presence of grain boundaries. There is very little understanding of the defect characteristics of this material system, and potential ways to mitigate their effects, *i.e.*, to passivate them. Defects in some polycrystalline materials are known to limit the efficiency of solar cells. Understanding the defect characteristics in GaInP could help us develop novel paths to reduce the impact of these defects on the overall performance of solar cells. There are also certain semiconducting materials that, despite having high defect density, can efficiently convert the infrared region of the sunlight to electricity, such as the widely deployed polycrystalline thin film solar cell materials: CdTe and $Cu(In,Ga)Se_2$. In this work, I have drawn analogies from processes and structures in these successful polycrystalline solar cell technologies, and adapted and generalized them to GaInP, to significantly improve its opto-electronic response. This is a key initial step to realize high efficiency polycrystalline GaInP-based solar cells.

Single-crystal GaInP photovoltaic cells generally have a layer of AlInP at the top. This layer reduces the defect density at the surface of GaInP, significantly increasing the lifetime of charge carriers in the absorber layer. This allows efficient collection of electron and holes, and the voltage of the GaInP-based solar cell to be higher. Reducing the number of surface defects and interface state density, the presence of surface charge, doping of capping layer, and atomic hydrogen at solar cell interfaces are also known to reduce carrier recombination and thus increase carrier lifetime. This research uses studies from other widely explored material systems to understand and improve the electronic characteristics of GaInP surface defects, experimentally and through modeling. This study helps to place individual experimental results on GaInP layers and devices in a broader context showing the interdependence of interface charge, conduction and valence band bending, and defect

energy level distribution and density, to explain and predict interface recombination and its profound effect on solar cell efficiency. Although the aluminum-assisted post deposition treatment developed here focuses on passivation of grain boundaries and surface of polycrystalline GaInP thin films, the principles of this method can be applied to any material – particularly III-V based compound semiconductors like GaAs, InP, InAs, GaP, etc.

1.3. Dissertation outline

Chapter 1 provides the motivation for studies presented in the dissertation. Chapter 2 introduces the experimental tools used for synthesis and characterization of thin films.

Chapter 3 presents modeling the effect of charge at the surface, and energy states of defects on band bending the GaInP-based test double heterostructures. Effect of surface recombination velocity on the expected performance of single junction solar cell is modeled. This study is further expanded to include effect of recombination rate at the grain boundaries on performance of polycrystalline solar cells. Finally, a preliminary estimate of performance of polycrystalline solar cells is made with varying grain size for four different surface recombination velocities. This study would help estimate the grain size needed to develop an efficient device if the recombination velocity is known. Or, it helps quantify the maximum surface and grain boundary recombination velocity that could realize a high efficiency solar cell with a given grain size.

Chapter 4 quantifies surface and bulk properties of single crystalline GaInP thin films using time resolved photoluminescence decay measurements. Bulk lifetime in GaInP, and recombination velocity at the surface of well passivated AlInP-GaInP double heterostructure is initially measured. The bulk lifetime measured in GaInP is used to

extract recombination velocity of free GaInP surface. Finally, effect of dielectric layers on the surface recombination velocity is also quantified.

Chapter 5 explores three different polycrystalline material systems that have demonstrated high conversion efficiency CdTe, $CuIn_{1-x}Ga_xSe_2$ and InP. Defects in these high performing materials are probed using Kelvin probe force microscopy, conductive atomic force microscopy, and admittance spectroscopy. Even though these material systems have high density of defects – some of which could act as recombination centers – the structure, and atomic composition around the defects seem to restrict their interaction with the minority charge carriers. Scanning probe microscopy measurements were used to probe and develop an understanding of surface potential close the grain boundaries – most defective regions in polycrystalline thin films – in material systems that have demonstrated solar cells with power conversion efficiency. Learning from these studies are used to develop novel passivation method in Chapter 6.

Chapter 6 presents the first study on synthesis and characterization of polycrystalline GaInP thin films. Objective of this study is to develop a polycrystalline GaInP thin film that has appropriate bandgap and has good optoelectronic characteristics that include – integrated photoluminescence intensity and minority carrier lifetime. A wide range of growth temperature and gallium content were explored to study the evolution of the crystal structure and optical properties of these thin films.

Based on the learnings from modeling and passivation studies of single-crystal GaInP, it is hypothesized that creation a high bandgap aluminum alloy of GaInP at the surface and grain boundaries could help passivate elongated 2D defects. To realize the proposed structure, a novel passivation method called aluminum assisted post deposition treatment

is developed and explored in this chapter. TEM-EDS and cathodoluminescence studies carried out on these structures confirm diffusion of aluminum along the grain boundary. Improvement in carrier lifetime indicates successful implementation of this novel proposed passivation method.

Finally, Chapter 7 summarizes the key findings of this research.

CHAPTER 2

EXPERIMENTAL METHODS

2.1. Molecular Beam Epitaxy

All the polycrystalline $Ga_xIn_{1-x}P_2$ films in this work have been grown using solid-source molecular beam epitaxy (MBE). MBE is an ultra-high vacuum (UHV) physical vapor deposition method that allows the growth of semiconductor materials with extreme control over composition of the grown films and their growth kinetics.

2.1.1. System details

The equipment used in this work was a Veeco Applied Epi Gen III system. The UHV in the growth chamber is achieved by using an ion pump and two closed-cycle cryogenic pumps. Liquid nitrogen was used to fill the cryogenic chamber which shrouds the growth

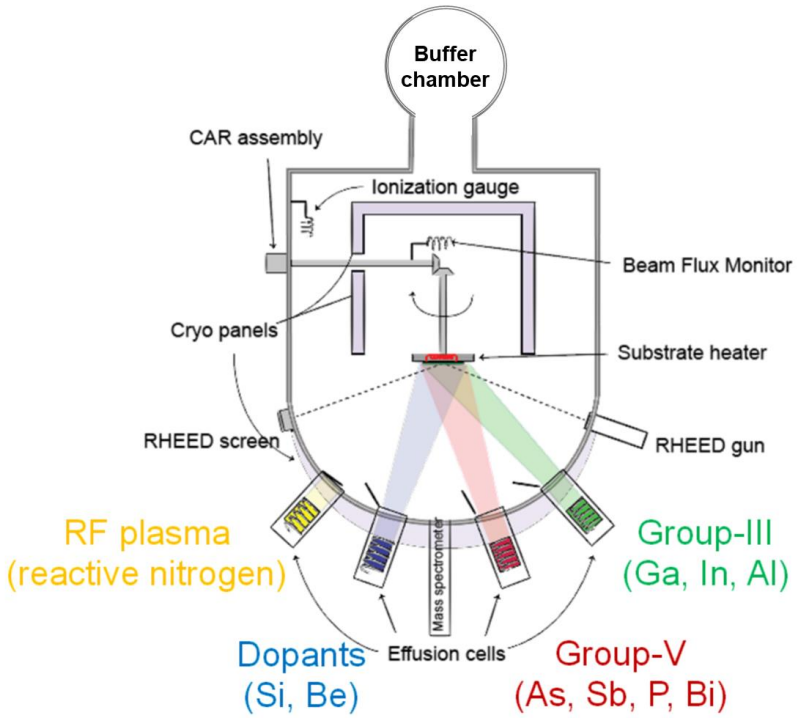

Fig. 2.1. Schematic of the molecular beam epitaxy reactor used in this work.

chamber. Walls of this cryogenic chamber act as an additional trap and decreases the partial pressure of oxygen-containing molecules such as CO, CO_2 and O_2 [9]. The Veeco Gen III system has three more chambers, that are used to load/unload the wafers into/ from the main chamber as well as pre-heat and bake the wafers before growth. A schematic of the MBE [10] used in this work is shown in Fig. 2.1.

During thin film growth with MBE, elements are thermally evaporated by heating the solid sources to very precise temperatures. Group-III elements (Al, Ga and In) are loaded in Knudsen effusion cells that have two heating coils – one near the base and the other coil near the tip of the crucible. The beam flux of group-III elements is controlled by changing the temperature of the base and tip of the effusion cell. Group-V elements (P and As) are loaded in crucibles with an attached cracker tube. During growths, the crucible is heated to a base temperature. Elements evaporate as As_4 and P_4 molecules and pass through the cracker valve. These molecules then pass through a cracker tube that is typically heated to 960°C. This breaks down As_4 and P_4 to As_2 and P_2 respectively. This process reduces the consumption of materials as dimer molecules typically have higher incorporation than their quaternary forms. The beam flux of group-V elements is controlled by adjusting the opening of a pin valve located at the head of the cracker tube.

The substrate is mounted on a continual azimuthal rotation (CAR) sample stage, that allows constant rotation of the substrate during growth and radiatively heats the substrate to the desired temperatures.

2.1.2. Auxiliary sensors

An ion gauge, hereafter referred to as beam flux monitor (BFM), is mounted on the back of substrate holder on the CAR to measure the beam equivalent pressures of the

elements to be deposited. Before each growth, this is used to accurately calibrate the fluxes of each of the Group III and group V elements which are to be used during growths.

MBE is also equipped with a residual gas analyzer (RGA) which is used to estimate the composition of the UHV. It is particularly useful during the venting process of the MBE. Before venting, all the phosphorus and arsenic deposited on cryogenic shrouds needs to be evaporated. RGA helps to detect any trace amounts of P or As being evaporated from the chamber walls.

MBE is also equipped with a reflection high energy electron diffraction (RHEED). It is primarily used to monitor the deoxidation temperature of GaAs substrate and qualitatively understand the type of thin film growth mechanism. Streaky RHEED pattern suggests Frank-van der Merwe (layer-by-layer) growth mechanism while spotty RHEED pattern suggests Volmer-Weber (island) growth mechanism. Occasionally, RHEED was also used to calibrate Ga and Al fluxes.

2.2. X-ray diffraction

X-ray diffraction is a non-destructive technique that is used to characterize lattice parameter, mismatch and thickness of epitaxial films, and crystal structure. In this study, $\omega - 2\theta$ scan is used in high resolution mode to extract lattice parameter of the epitaxially grown film. If the studied film is of ternary compound semiconductor like $Ga_xIn_{1-x}P$ and $Al_yIn_{1-y}P$, Vegard's law [11] could then be used to precisely estimate composition of the grown films from the measured lattice parameter.

Bragg diffraction occurs when radiation, with a wavelength comparable to the lattice spacing, is scattered in a specular fashion by the atoms of a crystalline system and undergoes constructive interference. The path difference between two waves undergoing

interference is given by $2d \sin\theta$. For constructive interference, this path difference needs to be an integer multiple of the incident radiation wavelength. Bragg's law, that describes the condition on theta for the constructive interference to be at its strongest is given by:

$$n\lambda = 2d \sin\theta \tag{2.1}$$

where n is a positive integer, d is the interplanar distance, λ is the wavelength of incident wave and θ is the angle of diffraction.

Table 2.1. Allowed and forbidden x-ray reflections in various cubic Bravais lattice

Bravais lattice	**Allowed reflections**	**Forbidden reflections**
Simple cubic	any h, k, l	None
Body-centered cubic	$h + k + l =$ even	$h + k + l =$ odd
Face-centered cubic	h, k, l all odd or all even	h, k, l mixed odd and even
Diamond FCC	All odd, or all even with $h + k + l = 4n$	h, k, l mixed odd and even, or all even with $h + k + l \neq 4n$

2θ scans are used to characterize polycrystalline thin films. In this mode, ω is kept fixed and 2θ is varied to measure the angle of diffraction. The diffraction pattern is used to

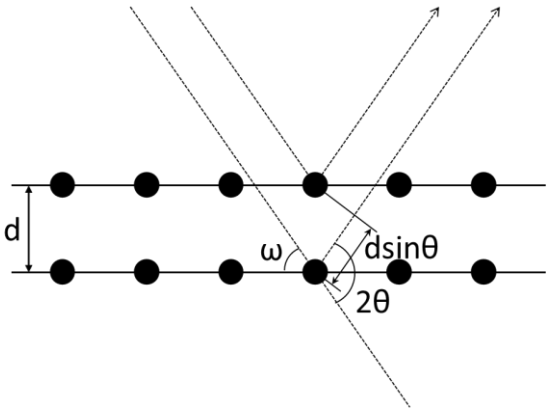

Fig. 2.2. Geometry of the incident and diffracted beam in X-ray diffraction

predict a likely crystal structure and lattice constant of the grown film. In case of cubic crystal structure, the interplanar distance measured using XRD, is related to the lattice parameter by the following equation:

$$d = \frac{\mathrm{a}}{\sqrt{h^2 + k^2 + l^2}} \tag{2.2}$$

where a is the lattice spacing, and h, k, and l are Miller indices of the Bragg plane. Selection rule for Miller indices of different cubic Bravais lattice are tabulated in Table 2.1. These selection rules, along with the interplanar distance extracted from XRD is used to decipher the probable crystal structure of the grown polycrystalline films.

2.3. Time-resolved photoluminescence decay measurements

Time-resolved photoluminescence spectroscopy is an experimental technique used to study the spectral and temporal evolution of photoluminescence from a sample following its illumination by a short pulse of light. In a semiconductor, the light pulse generates electron and hole pairs, some of which subsequently recombine to emit light. This decay in photoluminescence over time could be used to estimate important material and interface properties that include minority carrier radiative and non-radiative lifetime, and front and back interface recombination velocities. Improvement of these material properties is crucial to realize high performance devices.

To facilitate the discussion of the experimental results, some essential features of the theory developed by Nelson and Sober are outlined here [12]. Effective minority carrier lifetime is given by the following equation:

$$\frac{1}{\tau_{eff}} = \frac{1}{\tau_r} - \frac{F}{\tau_r} + \frac{1}{\tau_{nr}} + \frac{S_{front} + S_{back}}{W} \tag{2.3}$$

$$\frac{1}{\tau_{eff}} = \frac{1}{\phi\tau_r} + \frac{1}{\tau_{nr}} + \frac{2S}{w}$$

where τ_r is the minority carrier radiative recombination lifetime, F is the fraction of photons from radiative recombination that lead to electron-hole pair generation due to photon recycling, $\phi = 1/(1-F)$, τ_{nr} is the nonradiative recombination lifetime, S is the front and back interface recombination velocity, and w is the sample thickness.

In case of low-level injection, which is when photogenerated charge carrier concentration is lesser than equilibrium majority charge carrier concentration p_0 (for p-type semiconductor), $\tau_r = 1/(Bp_0)$, where B is the radiative recombination constant. The value of B can be calculated by measuring temperature dependence of PL peak intensity at steady state conditions.

2.4. Steady state photoluminescence spectroscopy

Photoluminescence spectroscopy is a widely used technique for the characterization of optical and electronic properties of semiconductors. In a typical steady state photoluminescence measurement, the laser pump power (P_{PL}) that is absorbed by the active region is proportional to the electron-hole pair photoexcitation density which is equal to the total electron-hole recombination rate within the active region. Also, the total PL intensity integrated over energy (L_{PL}) is proportional to the spontaneous emission rate per unit area per unit length from the active region. In case of low-level injection, Shockley-Read-Hall recombination rate is directly proportional to n, radiative recombination rate is proportional to n^2, and Auger recombination rate is proportional to n^3. Equation (2.4) summarizes the above-mentioned relationships.

$$P_{PL} = c_a[An + (1 - \gamma_r)Bn^2 + Cn^3] \tag{2.4}$$

$$L_{PL} = c_b Bn^2$$

Here, γ_r is the fraction of the spontaneous emission that is reabsorbed by the active region, and c_a and c_b are constants of proportionality that are determined by sample and measurement geometry. The terms associated with A, B and C represent rate of recombination through various physical processes namely Shockley-Read-Hall (SRH) recombination, radiative recombination, and Auger recombination, respectively [13].

The assumptions implied in equation (2.4) are that the fraction of the spontaneous emission recycled and the fraction of the pump power that photoexcites electron-hole pair are independent of injection level, which are , respectively valid under low level injection and when the pump photon energy is substantially larger than the active material bandgap.

2.5. Kelvin probe force microscopy

Kelvin probe force microscopy (KPFM) is a scanning probe microscopy technique that measures the local surface potential with respect to the probing tip. The two major KPFM detection techniques are amplitude modulated KPFM (AM-KPFM) and frequency modulated KPFM (FM-KPFM). In the past, the technique has been used for spatially resolved imaging of the surface potential in polycrystalline CIGS material system. This section will briefly introduce the basic physics this technique is built upon. Also, qualitative variances in the difference between surface potential at grain core and at grain boundaries in various compound semiconductors is also presented.

2.5.1. Physics and instrumentation

Work function of a material is defined as the energy needed to move an electron from Fermi level to vacuum level. When two conductors with different work functions are brought into electrical contact with each other, electrons flow from conductor with lower work function to the one with higher work function, in the process equalizing the Fermi energies. If they are made into a parallel plate capacitor, equal and opposite charge is induced on the surfaces. The potential established between these two surfaces is called contact potential difference, or simply surface potential.

$$V_{CPD} = \frac{\varphi_{sample} - \varphi_{tip}}{e} \tag{2.5}$$

As the conductive probe/tip and a conductive sample form a capacitor, the electrostatic force between them is given by the equation:

$$F_{el} = -\frac{1}{2}\frac{\partial C}{\partial z}(\Delta V)^2 \tag{2.6}$$

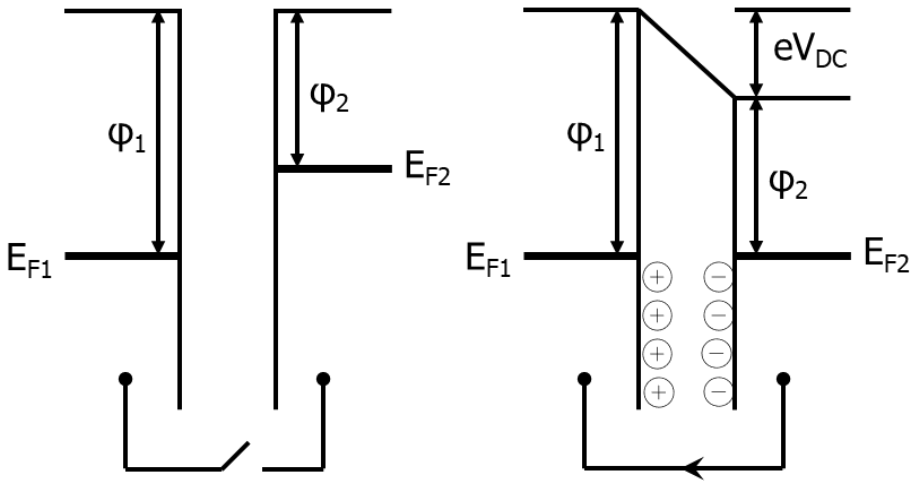

Fig. 2.3. Energy and charge diagram illustrating the Kelvin probe technique principle.

where F_{el} is the electrostatic force, ΔV is the potential difference between the tip and the sample. Also, ΔV is sum of the intrinsic CPD, an externally applied V_{DC} and the AC voltage.

$$\Delta V = V_{DC} - V_{CPD} + V_{AC}\sin(\omega t) \tag{2.7}$$

Combining the two equations, we get:

$$F_{el} = \frac{\partial C}{\partial z}((V_{DC} - V_{CPD})^2 + \frac{1}{2}V_{AC}^2) + \frac{\partial C}{\partial z}(V_{DC} - V_{CPD})V_{AC}\sin(\omega t) + \frac{1}{4}\frac{\partial C}{\partial z}V_{AC}^2\cos(2\omega t) \tag{2.8}$$

The term $\frac{\partial C}{\partial z}((V_{DC} - V_{CPD})^2 + \frac{1}{2}V_{AC}^2)$, will be referred to as the DC term, the one associated with $\sin(\omega t)$ as the ω term and the one associated with $\cos(2\omega t)$ as 2ω term. The equation suggests that the applied AC bias at a frequency of ω causes the electric force to modulate at both ω and 2ω, which could be measured directly using cantilever deflection. It is also evident that when the applied DC voltage is equal to the surface potential, the oscillation amplitude at ω goes to zero. This idea of "nulling" of the electric force amplitude at ω is used in amplitude modulated KPFM.

The electric force gradient is associated with the electric force by the equation,

$$F'_{el} = \frac{\partial F_{el}}{\partial z} \tag{2.9}$$

Therefore,

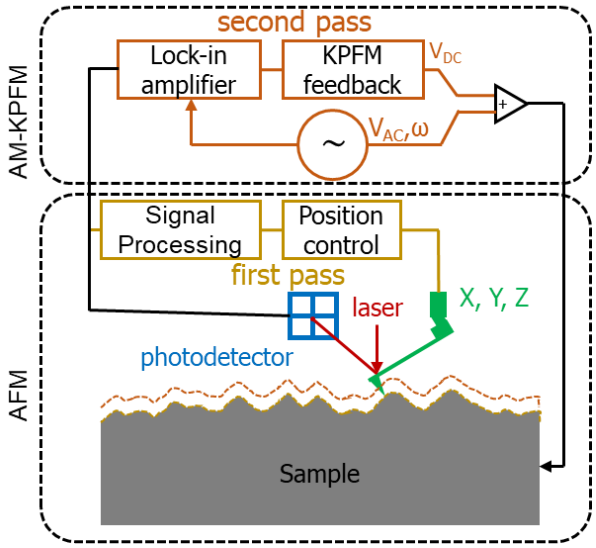

Fig. 2.4. Block diagram of signals in KPFM

$$F'_{el} = \frac{\partial^2 C}{\partial z^2}((V_{DC} - V_{CPD})^2 + \frac{1}{2}V_{AC}^2) + \frac{\partial^2 C}{\partial z^2}(V_{DC} - V_{CPD})V_{AC}\sin(\omega t) + \frac{1}{4}\frac{\partial^2 C}{\partial z^2}V_{AC}^2\cos(2\omega t) \tag{2.10}$$

The modulation amplitude of electric force gradient at ω also drops to zero at V_{DC} = V_{CPD}. This is used as the basis for nulling the electric force gradient to find surface potential in frequency modulated KPFM.

2.6. Admittance spectroscopy and drive level capacitance profiling

Admittance spectroscopy is used to measure activation energy of defects in copper indium selenide and its gallium alloys by Walter *et al.* [14]. This technique was further used to measure the evolution of defect activation energy due to the addition of gallium and sulfur [15]. The activation energy of the defects was used to predict the electronic

activity of the defects in these alloys. But the drive level defect density is thought to provide a more accurate measure of the defect state density and spatial location [16].

Drive level capacitance profiling (DLCP) is used to measure the drive level defect density, defined as the sum of the carrier concentration and the defect density. DLCP determines the amount of charge that responds to the oscillating voltage by fitting the dependence of the capacitance to the amplitude of the applied ac signal as described in [16]:

$$C = C_0 + C_1\delta V + C_2(\delta V)^2 \tag{2.11}$$

The drive level density (N_{DL}) as obtained from the first two coefficients is the sum of the free carrier concentration and the defect density located at position $\langle x \rangle = \varepsilon A/C_o$ having an emission energy of $E_e = k_B T\, ln(\nu/2\pi f)$:

$$N_{DL} = -\frac{C_0^3}{2q\varepsilon A^2 C_1} \tag{2.12}$$

where ε is the permittivity of the solar cell absorber layer, A is the area of the device and ν is the thermal emission prefactor. By varying the temperature and frequency, we can determine the spatial distribution of the sum of the free carrier concentration and the defect density.

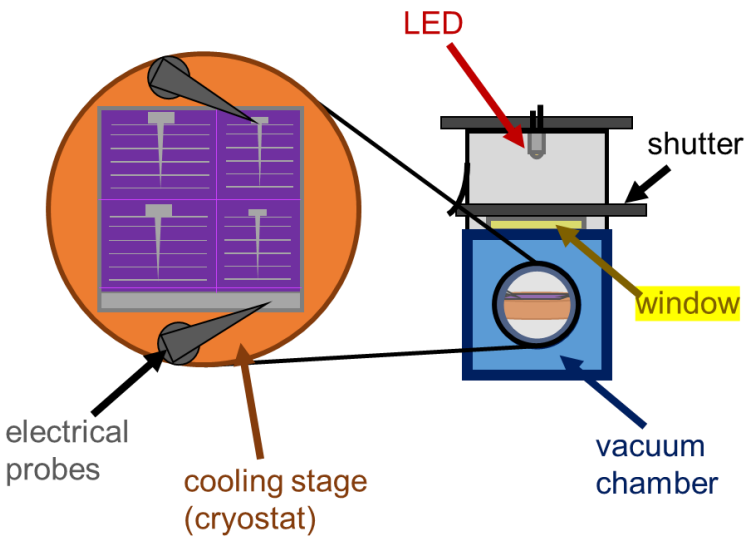

Fig. 2.5 Schematic of the experimental setup used for measuring the admittance spectroscopy and drive level capacitance profiling.

CHAPTER 3

MODELING INTERACTION OF CHARGE CARRIERS WITH DEFECTS AT THE INTERFACE

3.1. Introduction

Energy state distribution, and capture cross-section area of the defects present at an interface primarily control the recombination rate at that interface. In addition to these defect characteristics, defect activity is also governed by the properties of layers present in the device structure. Some of the layer properties that affect the defect activity are bandgap, electron affinity, doping, and thickness. Since the recombination rate in a layer is dependent on the entire structure, it is important to model and quantify the effect of each of these parameters on recombination rates in the studied device structures.

A common device architecture known as a double heterostructure (DH), is used to quantify recombination rate in the bulk as well as at the surface of a particular layer. In a double heterostructure, charge carriers are confined in a particular layer to be studied – called the “base” layer. One of the common ways the charge carriers are confined is by creating type-I heterojunction at both the interfaces of the base layer. The layers adjoining the base layer that create this heterojunction are called barrier layers. In addition to quantifying the basic material characteristics like bulk carrier lifetime, minority charge carrier diffusivity and recombination rate at the layer interfaces, a double heterostructure also helps in optimization of layer properties like thickness and doping of the barrier and base layers. These learnings can be used to predict and improve the performance of the studied devices.

In this chapter, we quantify the effect of defect and layer properties on charge carrier distribution and recombination in GaInP-based double-heterostructures. Presence of charge at various interfaces of a DH affects the minority carrier distribution and therefore changes the defect activity. In addition, energy state of defects also governs their activity/ charge state and therefore the rate of recombination at the defect site. These effects are quantified by solving the drift diffusion Poisson equations using a finite difference method.

3.2. Background

Depending on the activation energy and capture cross-section, defects present at the surface of a semiconductor can act as recombination centers. In an excellent study on AlGaInP/GaInP quantum wells, Dekker *et al.* [17] correlated deep level trap concentrations measured using deep level transient spectroscopy with steady state photoluminescence intensity and carrier lifetimes calculated using time resolved photoluminescence decay measurements. While DLTS measurements help quantify the density and activation energy of the electrically active defects in the space charge region, and TRPL measurements help quantify the recombination velocity due to the presence of these defects, electronic structure of these defects is predicted using inferences from indirect characterizations, correlations developed between process parameters and defect densities and atomic simulations that predict the structure of defects that have thermodynamically favorable energies of formation. One of the prominent characterization techniques that measures the charge state of the defect is electron paramagnetic resonance (EPR). Bardeleben *et al.* [18] measured the origin of EL2 defect in GaAs using EPR and deduced the structure to be a complex $As_{Ga} + As_i$. The work also correlates this defect structure to the activation energy and density of the defect using

DLTS. Huang *et al.* [19] also inferred the structure of a deep level defect in GaInP to be vacancy of phosphorus using thermal-electric effect spectroscopy. In addition to the charge and activation energy of the defects, energy of formation of various defects are can also be calculated to predict the stability of one defect state over another. Extensive studies by Zhang *et al.* [20] and Colleoni [21] predict the formation energies of defects in various III-V based compound semiconductors.

W. Walukiewicz developed a theory on Fermi level dependent formation of native defect in semiconductors [22, 23]. According to the theory, introduction of large concentrations of defects in III-V based compound semiconductors lead to the stabilization of the Fermi level. The Fermi-level energy is observed to correspond to the average energy of the sp^3 hybrid. The stabilization energy is observed to be independent of the type of doping and the doping level. This stabilization or "pinning" of Fermi level is also observed to be constant with respect to the vacuum level in various III-V based compound semiconductors. Amongst several mechanisms proposed to explain this phenomenon, formation of native acceptor-like and donor-like defects at the interface explains most of the experimental observations. Accordingly, the theory predicts that the native defects in GaInP would be very close to the middle of the bandgap. In addition to the native defects, surface recombination velocity is also shown to be governed by the surface charge [24]. While defect states at the interface are expected to dominate the recombination rate in most cases, there have been cases where presence of ad-atoms have reduced the defect density [25].

This chapter presents simulations quantifying the effect of surface charge on distribution of potential energy of the minority charge carrier in a GaInP-based double heterostructure. This can be used the derive equilibrium minority charge carrier

distribution, and therefore estimate the surface recombination velocity. In addition, Effect of recombination velocity at surfaces and grainsize of polycrystalline GaInP on its expected solar cell performance are also quantified.

3.3. Experimental Methods

3.3.1. Physics behind Sesame

Effect of defect parameters on recombination rate in the double heterostructure is modeled using an open source Python3 package called Sesame [26]. Sesame is used to solve the drift diffusion Poisson equations for multi-dimensional systems using finite difference method. The software computes the steady state of a semiconductor between two contacts, and subject to voltage bias and/ or illumination.

The steady state of the system under non-equilibrium conditions is governed by the following drift diffusion Poisson equations:

$$\begin{aligned} \vec{\nabla} \cdot \vec{J}_n &= -q(G \cdot R) \\ \vec{\nabla} \cdot \vec{J}_p &= q(G \cdot R) \\ \vec{\nabla} \cdot (\epsilon \vec{\nabla} \phi) &= -\rho/\epsilon_0 \end{aligned} \tag{3.1}$$

with the currents:

$$\begin{aligned} \vec{J}_n &= -q\mu_n n \vec{\nabla} \phi + qD_n \vec{\nabla} n \\ \vec{J}_p &= -q\mu_p p \vec{\nabla} \phi - qD_p \vec{\nabla} p \end{aligned} \tag{3.2}$$

Here, $n(p)$ is the electron (hole) number density, ϕ is the electrostatic potential and $\vec{J}_{n(p)}$ is the charge current density of electrons (holes). q is the absolute value of the electronic charge and ρ is local charge, ϵ is the dielectric constant of the material, and ϵ_0 is the

permittivity of free space. $\mu_{n(p)}$ is electron (hole) mobility and is related to the diffusivity $D_{n(p)}$ by $D_{n(p)} = k_B T \mu_{n(p)}/q$ where k_B is the Boltzmann constant and T is the temperature.

3.3.1.1. *Recombination in the bulk of semiconductor*

The three mechanisms modeled for bulk recombination are: radiative, Auger, and trap-assisted recombination – particularly Shockley-Read-Hall (SRH). Equation governing the trap-assisted recombination is:

$$R_{SRH} = \frac{np - n_i^2}{\tau_p(n + n_1) + \tau_n(p + p_1)} \tag{3.3}$$

Here $n_i^2 = N_C N_V e^{-E_g/k_B T}$, $n_1 = n_i e^{E_T/k_B T}$, $p_1 = n_i e^{-E_T/k_B T}$. E_T is the energy level of trap state measured from intrinsic energy level, and $N_C(N_V)$ is the conduction (valence) band density of states. The equilibrium Fermi energy level at which $n = p = n_i$ is the intrinsic energy level E_i. $\tau_{n(p)}$ is the bulk lifetime for electrons (holes) given by the equation:

$$\tau_{n(p)} = \frac{1}{N_T \upsilon_{n(p)}^{th} \sigma_{n(p)}} \tag{3.4}$$

Here N_T is the trap density, $\upsilon_{n(p)}^{th}$ is the thermal velocity of the charge carriers and $\sigma_{n(p)}$ is the capture/ emission cross-section of electrons (holes).

The radiative recombination is modeled using the following equation:

$$R_{rad} = B(np - n_i^2) \tag{3.5}$$

Here, B is the radiative recombination coefficient of the material. Finally, Auger recombination is modeled by the equation:

$$R_A = (C_n n + C_p p)(np - n_i^2) \tag{3.6}$$

where C_n (C_p) electron (hole) Auger coefficient.

3.3.1.2. *Recombination at surfaces, interfaces, and grain-boundaries*

Additional extended defects at the sample surface or interfaces are also modeled. The extended defects can have either discrete or continuous energy levels. For defects with discrete energy levels, a subscript d is used. The occupancy of the defect level f_d is given by:

$$f_d = \frac{(S_n n_d + S_p p_d)}{S_n(n + n_d) + S_p(p + p_d)} \tag{3.7}$$

where $n(p)$ is the electron (hole) density at the location of the defect, and $S_{n(p)}$ is the recombination velocity parameter for electron (hole). n_d and p_d are given by:

$$\begin{aligned} n_d &= n_i e^{E_d/k_B T} \\ p_d &= n_i e^{-E_d/k_B T} \end{aligned} \tag{3.8}$$

where E_d is calculated from the intrinsic energy level E_i. The defect recombination is of SRH type:

$$R_d = \frac{S_n S_p (np - n_i^2)}{S_n(n + n_d) + S_p(p + p_d)} \tag{3.9}$$

The charge density q_d by a single defect state depends on the defect type:

$$q_d = q\rho_d \times \begin{cases} (1 - f_d) & \text{donor} \\ f_d & \text{acceptor} \end{cases} \tag{3.10}$$

where ρ_d is the density of states due to defects at energy E_d. S_n, S_p and ρ_d are related to capture cross-sections σ_n and σ_p of the defect level by $S_{n(p)} = \sigma_{n(p)} v_{n(p)}^{th} \rho_d$ where $v_{n(p)}^{th}$ is the electron (hole) thermal velocity.

For a given system, Sesame first solves the equilibrium problem. In equilibrium, the quasi-Fermi level of electrons and holes are equal and spatially constant. The code choses an energy reference such that in equilibrium, $E_F = E_{F_p} = E_{F_n} = 0$. This simplifies the equation. Charge at the boundary is assumed to be dictated by the doping density of the material at the surface.

3.3.2. Study outline

As seen from the equations in the previous section, the rate of recombination depends on the carrier concentration at the location where defects are present. In addition to all the layer properties, defect characteristics could also alter the charge carrier concentration around it. Therefore, the primary areas studied in this chapter are:

1. Variation in charge carrier concentration near the top barrier-base interface due to change in top-barrier thickness and doping for different surface charge densities.

2. Variation of charge carrier concentration near the top barrier-base interface due to change in defect energy state density at the top-barrier surface upon illumination.

In addition, the effect of minority charge carrier lifetime on solar cell efficiency is also modeled and quantified. This dependence of carrier lifetime on solar cell performance is used to estimate the effect of recombination velocity on the upper limit of practically achievable solar cell efficiency for various GaInP grain sizes.

3.3.2.1. *Structure details*

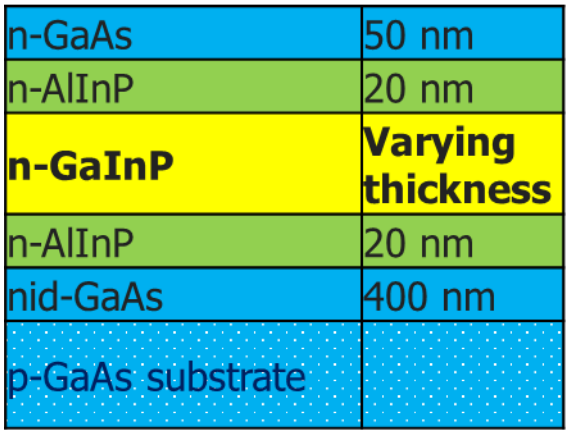

Fig. 3.1 Schematic of typical GaInP-based double heterostructure.

This modeling study focuses on understanding recombination in GaInP-based double-heterostructures. A schematic of the baseline structure studied is shown in Fig. 3.1. Based on the functionality, the layers in the double-heterostructure can be categorized into five types: (1) Substrate layer, (2) buffer layer, (3) barrier layers, (4) base layer, and (5) cap layer.

The substrate is assumed to be the bottom-most layer of the structure. Cap layer is the layer that is grown on top of the top barrier layer. All the structures in this study have GaAs as substrate and buffer layer. Also, when present, the cap layer is a 50-nm thick GaAs that is heavily doped either p- or n-type. Unless otherwise specified, the primary structure discussed in this study has $Ga_{0.51}In_{0.49}P$ as the base layer. One of the barrier layers is AlInP which is present above the buffer layer. $Ga_{0.51}In_{0.49}P$-base layer is present on top of this AlInP-barrier layer. In the baseline configuration, another layer of AlInP is present on top the GaInP-base as a top-barrier layer which is capped with a heavily doped GaAs cap layer. Various layer and defect properties as well as external stimuli could affect the recombination in GaInP.

Table 3.1 Summary of material properties used during modeling the distribution of charge carriers in a GaInP-based double heterostructure.

Parameters	**GaInP [27]**	**AlInP [28]**	**GaAs [29]**
L [nm]	Variable	Variable	400 nm
ϵ	10	10	13.1
N_C [cm^{-3}]	7.72×10^{17}	1.45×10^{18}	4.7×10^{17}
N_V [cm^{-3}]	1.41×10^{19}	1.31×10^{19}	7.0×10^{17}
E_g [eV]	1.88 [30]	2.244 [31]	1.424
χ [eV]	4.1 [33]	4.0 [32]	4.07
Doping [cm^{-3}]	Variable	Variable	8.0×10^{17}

Material properties used during simulations are summarized in Table 3.1 [27, 28, 29, 30, 31, 32, 33]. These material parameters have been measured by various research groups in the past and are widely agreed upon. There are also some other material characteristics that affect charge carrier distribution and recombination kinetics. These parameters are electron and hole effective mass, electron and hole mobility (also correlated to their respective diffusivity), effective carrier lifetime, and energy level of the bulk defects. The value of these parameters is observed to depend on the doping concentration and other growth parameters. Therefore, typical material values reported in literature that are expected to maximize the performance of solar cell are chosen. This is expected to help focus the study on parameters of interest.

Table 3.2 Summary of defect properties used during modeling the distribution of charge carriers in this study.

Parameters	**GaInP surface**	**AlInP surface**
Defect energy [eV]	-0.94 – +0.94	-1.1 – +1.1
Density [cm^{-2}]	$10^9 - 10^{15}$	$10^9 - 10^{15}$
Electron capture cross – section area [cm^2]	1×10^{-15}	1×10^{-15}
Hole capture cross – section area [cm^2]	1×10^{-15}	1×10^{-15}
Transition	0/+1 or 0/-1	0/+1 or 0/-1

Planar defects modeled in this chapter are assumed to have characteristics summarized in Table 3.2. Much less information is reported on defect characteristics of high bandgap ternary III-V compound semiconductors like GaInP and AlInP, than for GaAs and Si. Therefore, the effect of these various intrinsic defect characteristics on externally detectable properties – like electron/ hole potential energy distribution,

recombination velocity, etc. – is modeled. The defect energy level is defined with respect to the intrinsic energy level. The bandgap of GaInP is taken to be 1.88 eV. The defect energy level is varied between the valence band edge (-0.94 eV) and the conduction band edge (+0.94 eV). The free surface of GaAs or GaInP is expected to have an atomic density of ~1.25×10^{15} cm^{-2} [34]. Therefore, the studied defect densities are in the range 10^{9} – 10^{15} cm^{-2}.

3.4. Results

3.4.1. Baseline simulations

3.4.1.1. *Band diagram of baseline double heterostructure*

The baseline structure studied, and the expected band diagram is shown in Fig. 3.2 (a) and (b) respectively. For baseline calculations, it is assumed that there are no defects at any interfaces or surfaces, including the AlInP surface and AlInP-GaInP

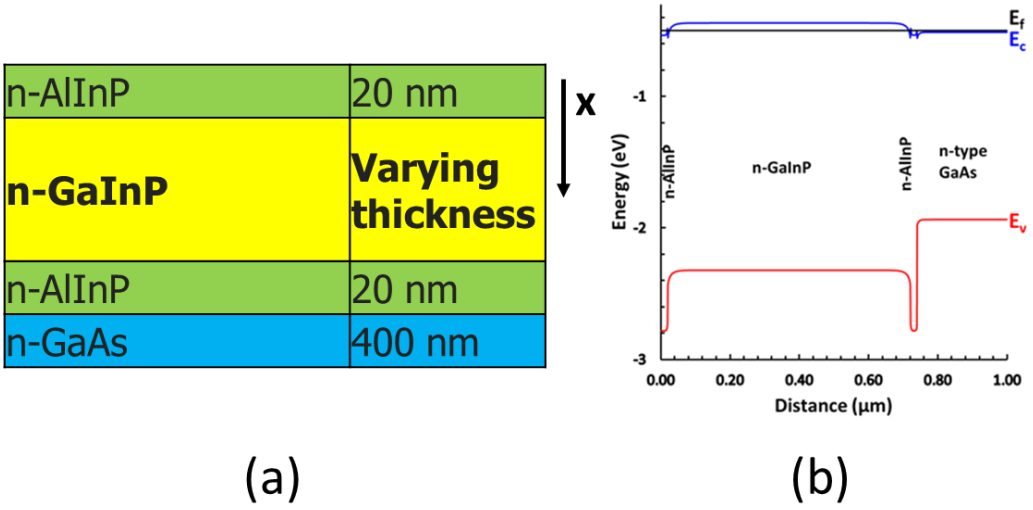

Fig. 3.2 (a) Structure of double heterostructure modeled in this study, and (b) band diagram of the GaInP-based double heterostructure with a base thickness of 700 nm

interfaces. The top-barrier AlInP layer is usually capped with GaAs, and the defect density at AlInP surface is also assumed to be zero.

The double heterostructure studied here forms two type-I (straddling) hetero-interfaces. In n-type DH structure as presented here, holes – which are minority charge carriers – are repelled away from interfaces. Since interfaces are expected to have a relatively higher density of defects when compared to that in the bulk, reducing the concentration of minority charge carrier near the interfaces is expected to reduce the SRH recombination rate.

3.4.1.2. *Effect of defect energy state distribution on recombination rate at the surface*

Some theories used to explain the origin of Fermi-level pinning assume a presence of high density of defect states within the bandgap. The energy level of these defect states is expected to govern the position of Fermi level pinning. For example, the Fermi-level in GaAs shows evidence that it is pinned at about $E_g/3$ above the valence band [35]. Similarly, defect states at the InP surface seem to pin its Fermi level $E_g/3$ below the conduction band [35][36].

Figure 3.3 summarizes the change in recombination rate in a GaInP-based double heterostructure with change in defect energy at the AlInP surface. Varying the energy level of the defect at the AlInP changes the minority charge carrier distribution throughout the structure. As the defect energy state gets closer to the middle of the bandgap, the recombination rate is seen to increase. It can also be observed that the Fermi level splitting is much lesser near the defect sites than in the bulk material. This simulation demonstrates the apparent "pinning" of the Fermi level at the position of the defect energy levels. Appropriate doping and thickness of AlInP barrier layer can limit recombination due to Fermi level pinning. These parameters are explored in detail in the next few sections.

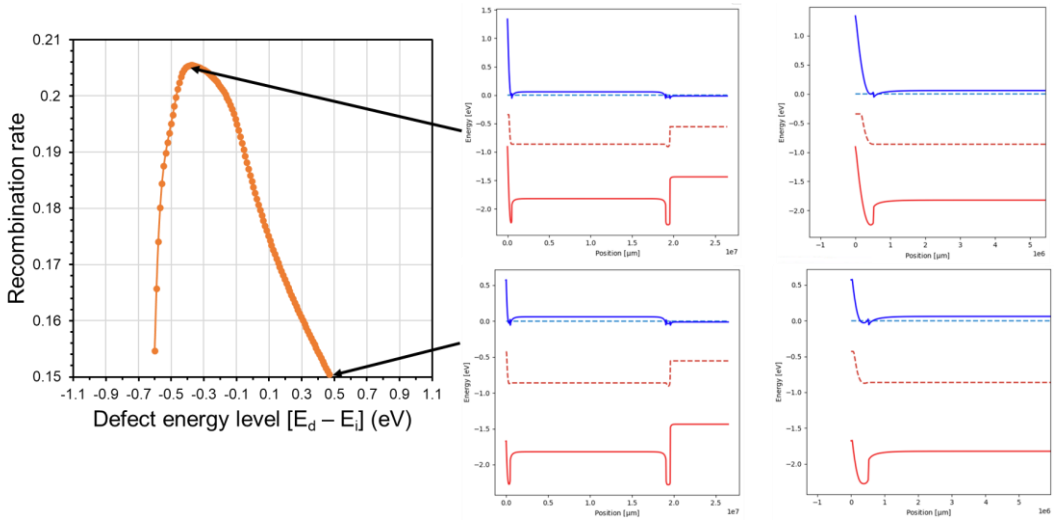

Fig. 3.3 (a) Effect of surface defect energy level on band-bending in AlInP layer and GaInP layer near AlInP-GaInP interface.

3.4.2. Effect of varying surface charge, thickness and doping of the barrier layer on band bending near AlInP-GaInP interface

This section discusses the effect of various top-barrier layer properties on band-bending in the top-barrier AlInP layer as well as in the base GaInP layer close to the AlInP-GaInP interface.

The presence of dangling bonds at the surface or in the bulk of barrier layer can induce a fixed charge. This charge may increase or decrease the minority charge carrier distribution at the surface of AlInP. To simulate the presence of positive fixed charge, planar defects with defect energy level of +10 eV and an allowed transition of 0/+1 are chosen. Similarly, to simulate negative fixed charge, planar defects with defect energy level of -10 eV and an allowed transition of -1/0 are chosen.

In n-type DH structure, presence of negative charge on AlInP surface would attract holes – the minority charge carriers. This would lead to the creation of a depletion layer in the AlInP layer. The thickness of this depletion layer is expected to be directly dependent on the density of the surface charge and the doping level in the AlInP layer. Fig. 3.4 shows variation of the valence band edge – which is also a representation of charge carrier concentration – near the AlInP-GaInP interface with change in charge density on AlInP surface. The surface charge density is varied from $1 - 12 \times 10^{12}$ cm^{-2}.

As seen in previous section, presence of defect at the AlInP surface changes the Fermi-level splitting under illumination (Fig. 3.3). This alters the recombination rate at the AlInP surface, and in some cases – as outlines later in the section – could alter the charge carrier distribution throughout the studied structure.

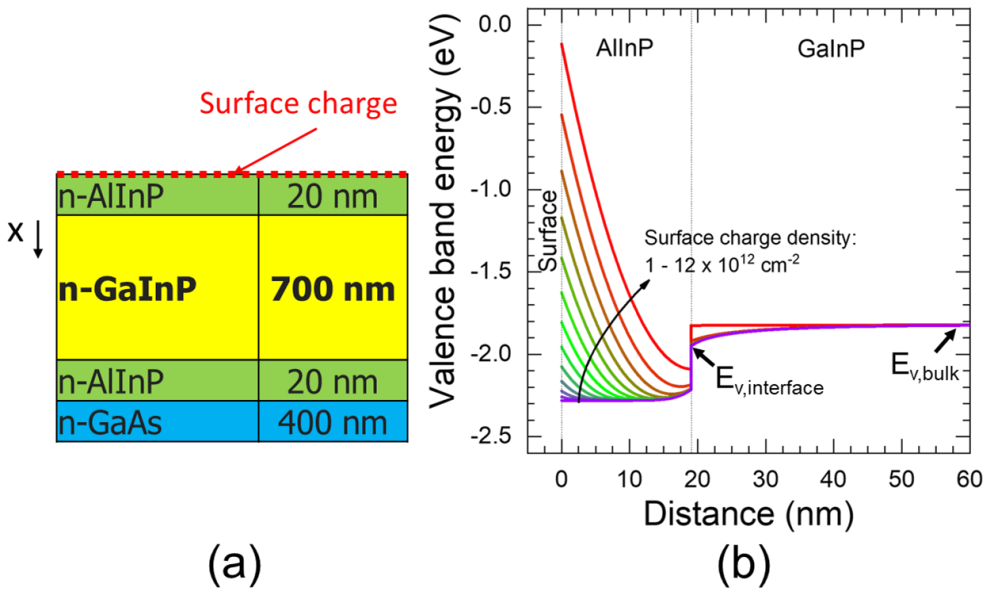

Fig. 3.4 (a) Schematic of the modeled structure, and (b) effect of surface charge on band-bending in AlInP layer and GaInP layer near AlInP-GaInP interface.

Figure 3.4 (a) shows a schematic of the double heterostructure simulated in this study with different amounts of negative surface charge at the AlInP surface. As seen in Fig. 3.4(b), it can be observed that the valence band edge in GaInP starts varying only when the surface charge increases beyond the value at which AlInP is completely depleted. Variation in the valence band edge in GaInP is also indicative of the change in distribution of minority charge carrier concentration. This variation in valence band edge in GaInP is hereafter referred to as band-bending in GaInP. Numerically, we define band bending as the difference in the value of valence band edge of GaInP at AlInP-GaInP interface (also referred to as GaInP surface) and 500 nm beneath the GaInP surface (also referred to as GaInP bulk region). A negative value for band bending in GaInP implies lesser concentration of holes at the GaInP surface compared to that in the GaInP bulk region, and a positive value of band bending in GaInP indicates accumulation of holes at GaInP

surface. Therefore, by changing the sign of charge at the surface, we can alter the concentration of minority charge carriers in different regions of the structure. Engineering this surface charge to reduce the concentration of minority charge carrier concentration near the most defective regions of the structure could drastically reduce the overall rate of trap assisted form of recombination. Conversely, presence of undesired surface charge could significantly increase trap-assisted recombination, and therefore limit the performance of the device.

For a constant surface charge density, increase in the doping of top-barrier AlInP layer reduces the width of the depletion region. Therefore, to reduce the effect of surface charge, either the thickness or the doping of the top-barrier layer needs to be increased. Fig. 3.5 summarizes effect of three different AlInP doping levels and two different AlInP thicknesses on band bending in GaInP for a fixed surface charge density of 2×10^{13} cm^{-2}. The three studied doping levels of n-type doped AlInP are 8×10^{18} cm^{-3}, 4×10^{18} cm^{-3}, and 8×10^{17} cm^{-3}. The two studied AlInP thicknesses are 20 nm and 40 nm. It can be observed that, in the case of AlInP doping level of 8×10^{18} cm^{-3}, thickness of the depletion layer is less than 20 nm. Therefore, there is no appreciable band bending in GaInP in both the studied cases of AlInP thickness of 20 nm and 40 nm. This AlInP doping level is one of the highest reported value in the literature. If the AlInP doping level is reduced to 4×10^{18} cm^{-3}, the thickness of the depletion is larger than 20 nm but slightly less than 40 nm. Therefore, we observe a significant band bending in the structure with 20 nm AlInP layer thickness; no significant band bending is observed in the case with 40 nm AlInP layer thickness. In case of AlInP doping level of 8×10^{17} cm^{-3}, the thickness of the depletion layer is much larger than either of the AlInP layer thickness that were modeled. Therefore, there is appreciable band bending in both cases, but the amount of band bending in the case

with AlInP thickness of 20 nm was much larger than the case with AlInP thickness of 40 nm.

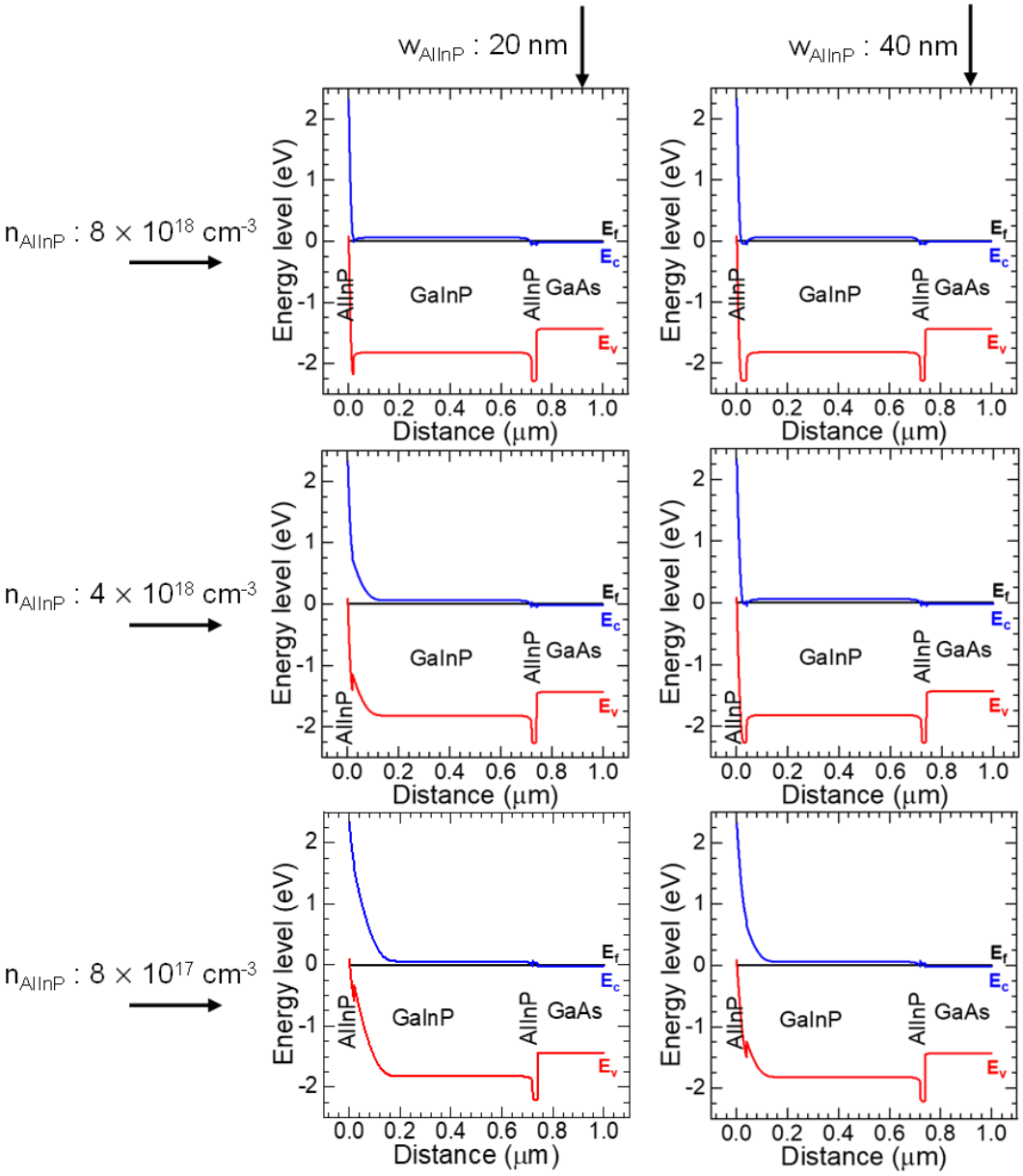

Fig. 3.5 Band diagram of double heterostructures with a fixed negative surface charge of 2×10^{13} cm^{-2} and varying AlInP-barrier thickness and doping level.

The effect of various surface charge densities and AlInP doping on band bending in GaInP is quantified in much more detail and plotted in a 2D contour plot as seen in Fig. 3.6. Fig. 3.6 (a) and (b) represent two cases with AlInP thickness of 20 nm and 40 nm, respectively.

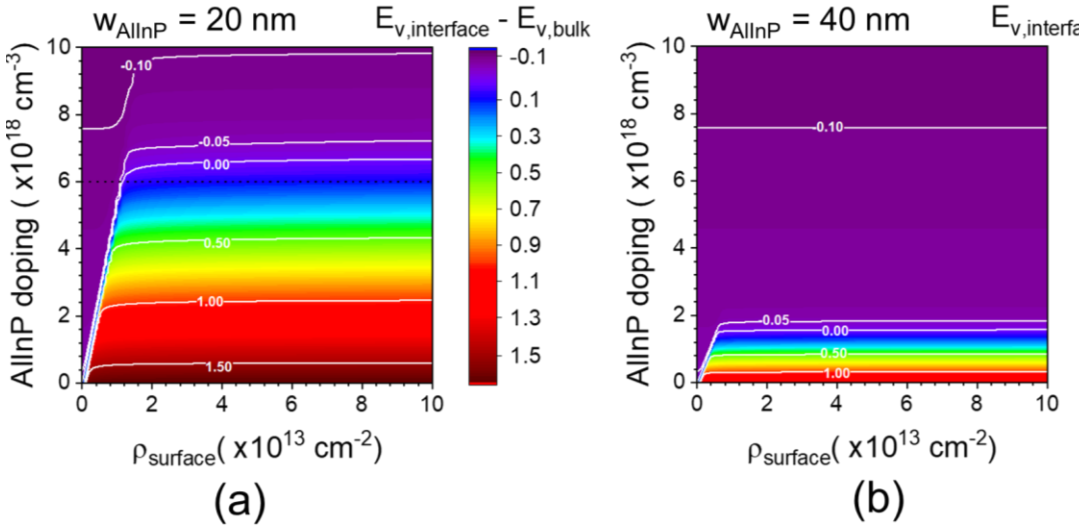

Fig. 3.6 Effect of surface charge density and AlInP doping density on band-bending in GaInP layer for (a) 20 nm, and (b) 40 nm thick AlInP layer

For an AlInP thickness of 20 nm, band bending in GaInP is negative for all AlInP doping levels above 6.4×10^{18} cm^{-3}. This suggests that an AlInP barrier layer with doping level greater than 6.4×10^{18} cm^{-3} and thickness of 20 nm would shield most of the surface charge effects on band bending in GaInP. In the case with AlInP thickness of 40 nm, the minimum AlInP doping level that is needed for positive band bending in GaInP is 1.8×10^{18} cm^{-3}.

Given a particular AlInP thickness, this 2D plot visually tells the minimum doping required to avoid hole accumulation at AlInP- GaInP interface. This study indicates that if the AlInP layer is doped to the highest reported level of 8×10^{18} cm^{-3}, a 20 nm thick AlInP barrier layer will be able to shield the effect of negative surface charge of at least up to

1×10^{14} cm^{-2}. AlInP is prone to oxidation. Thickness of the native oxidation layer on AlInP is approx. 10-15 nm. Therefore, a 40 nm thick AlInP with doping concentration of 8×10^{18} cm^{-3} is expected to be an effective barrier layer even after oxidation.

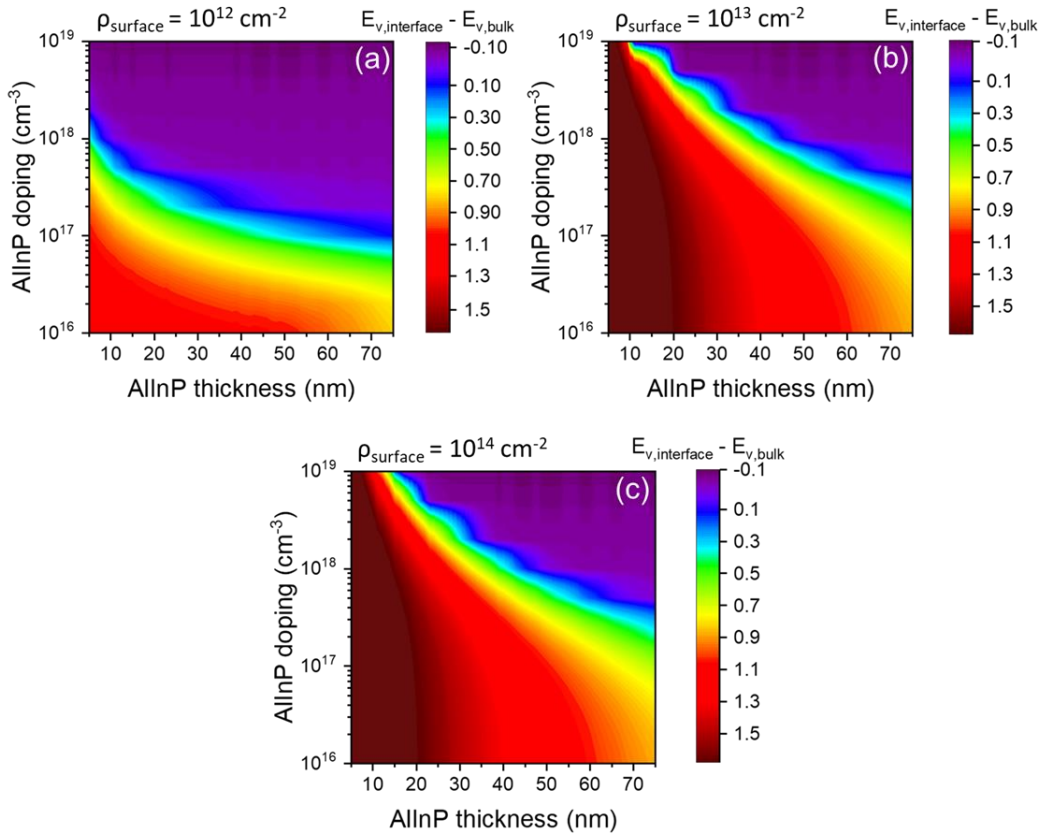

Fig. 3.7 2D plots quantifying band-bending in GaInP as a function of AlInP thickness and AlInP doping for three levels of negative charge densities at the AlInP surface of (a) 10^{12} cm^{-2}, (a) 10^{13} cm^{-2}, and (a) 10^{14} cm^{-2}

If charge at the AlInP surface is assumed to be constant, the effect of varying AlInP doping concentration and its thickness on band bending in GaInP is summarized in Fig. 3.7. Three cases with surface charge density of 1×10^{12} cm^{-2}, 1×10^{13} cm^{-2} and 1×10^{14} cm^{-2} are studied.

If we assume a fixed surface charge on a semi-infinite layer of AlInP with uniform doping concentration, the minimum thickness of the depletion region is given by:

$$w_{depletion} = \frac{\rho_{surface}}{n_{AlInP}} \tag{3.11}$$

The equation suggests that, at constant surface charge density, the thickness of the depletion layer is inversely proportional to the doping concentration of AlInP. The white contour line in 2D plots of Fig. 3.7 indicate a band bending of 0 eV. It can be observed that in each of the three studied cases, to reduce the band bending in GaInP, a thicker AlInP is required if the doping concentration of AlInP is reduced. As shown earlier, since band bending in GaInP is initiated only after completely depleting the top-barrier AlInP layer, the band bending contours seem to follow a trend as suggested by Eq. (3.11).

This section investigated effect of surface charge, thickness, and doping level on equilibrium charge carrier distribution in a double heterostructure. Band bending for a fixed thickness and doping level of AlInP layer remains almost fixed for surface charge value above 2×10^{13} cm^{-2}. This indicates that Fermi level remains pinned for surface charge above a particular level. Reducing the surface charge density below a certain value dramatically reduces the band bending recombination in GaInP.

3.4.3. Effect of recombination velocity at the surface and grain boundary on solar cell performance

In this section, first, the effect of carrier lifetime on solar cell performance is modeled by varying the bulk carrier lifetime and assuming that there is no recombination at the surfaces. A pn-type homojunction of GaInP is simulated with 100 nm heavily doped n-type emitter (6×10^{18} cm^{-3}) and 900 nm thick lightly doped (8×10^{16} cm^{-3}) base layer. The electron and hole mobility and lifetime are assumed such that their diffusion lengths are

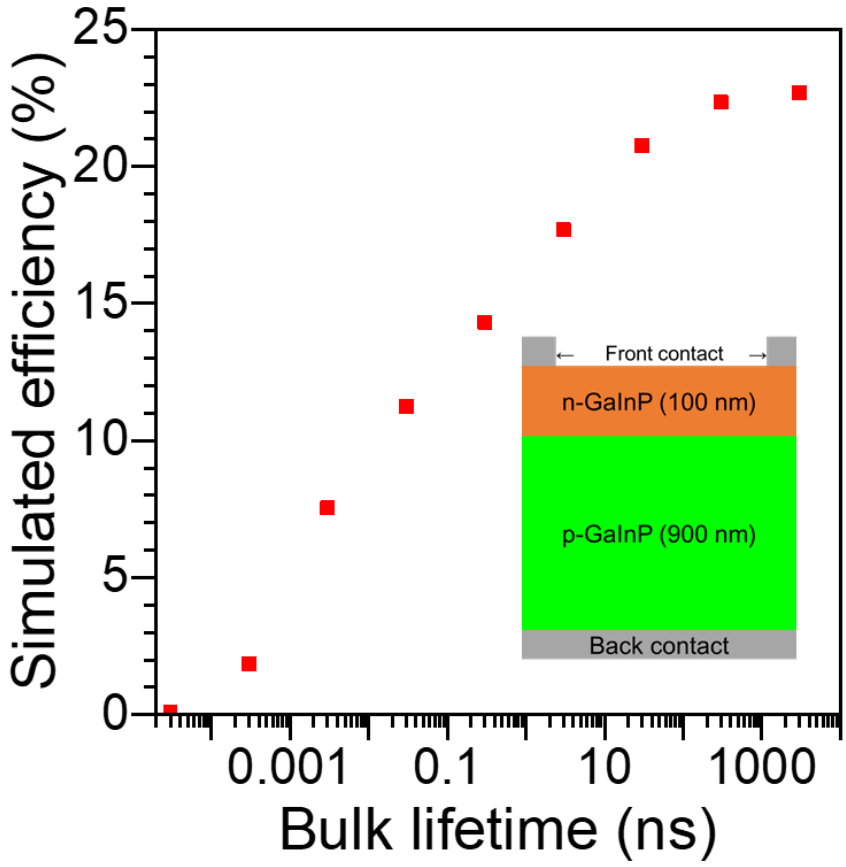

Fig. 3.8 Simulated effect of carrier lifetime on power conversion efficiency of GaInP solar cell with 1.88 eV bandgap under AM 1.5G illumination.

much larger than 3 micrometers. Solar spectrum AM 1.5G that has a total power density of 100 mW.cm^{-2} is incident on the device.

As seen in Fig. 3.8, simulated solar cell performance is a strong function of minority carrier lifetime. Simulated efficiency value varies from ~0% at carrier lifetime of 10^{-14} seconds to nearly 22% at carrier lifetime of 3 μs.

The effect of grain size on power conversion efficiency of solar cell is estimated for a sample structure shown in Fig. 3.9(a). Assumptions to estimate the effect of grain size on power conversion efficiency of solar cell are:

1. Grains are assumed to be tetragonal in shape with a thickness of 1000 nm. Grain size (d) is the length of side of the square that is varied from 1 nm to 1 mm.
2. Recombination velocity at grain boundaries is exactly same as that at the front surface.
3. No recombination happens in GaInP bulk.

Since it is assumed that the recombination rate at the grain boundary is assumed to be equal to that at the front and back surface, change in the total recombination rate is proportional to the change in total surface area due to the presence of grain boundaries.

$$Recombination\ rate = \frac{(4dw + 2d^2) \cdot S \cdot n}{d^2 w} \tag{3.12}$$

$$Recombination\ rate = \frac{n}{\tau_{eff}}$$

$$\frac{1}{\tau_{eff}} = \left(\frac{4}{d} + \frac{2}{w}\right) \cdot S \qquad (3.13)$$

Assuming that the effective carrier lifetime has contribution only from the recombination at the surface and grain boundary, the effective carrier lifetime is given by Eq. (3.13). If a value of recombination velocity is assumed, effective carrier lifetime for variable grain sizes can be estimated. Assuming that the dependence of simulated solar cell performance on effective carrier lifetime is similar to that simulated in Fig. 3.8, effect of varying grain size on solar cell performance can be simulated for a given value of surface recombination velocity.

Figure 3.9(b) shows the change in simulated power conversion efficiency of the GaInP-based solar cell with increase in grain size for different recombination velocities. It is observed from the graph that if the recombination velocity of surface and grain boundaries is 1×10^{1} cm.sec^{-1}, a grain size of even a 100 nm theoretically demonstrates power conversion efficiency of over 20%. For a grain size of 1 μm, surface recombination velocity of at least 1×10^{3} cm.sec^{-1} is needed to demonstrate more than 20% power conversion efficiency. Any recombination velocity higher than 1×10^{3} cm/sec critically reduces the performance.

While this chapter presented simulation results that study the effect of surface recombination velocity on overall cell performance, the next chapter experimentally quantifies the surface recombination rate at GaInP surface after deposition of dielectric

layers with different associated fixed charge using time resolved photoluminescence decay measurements.

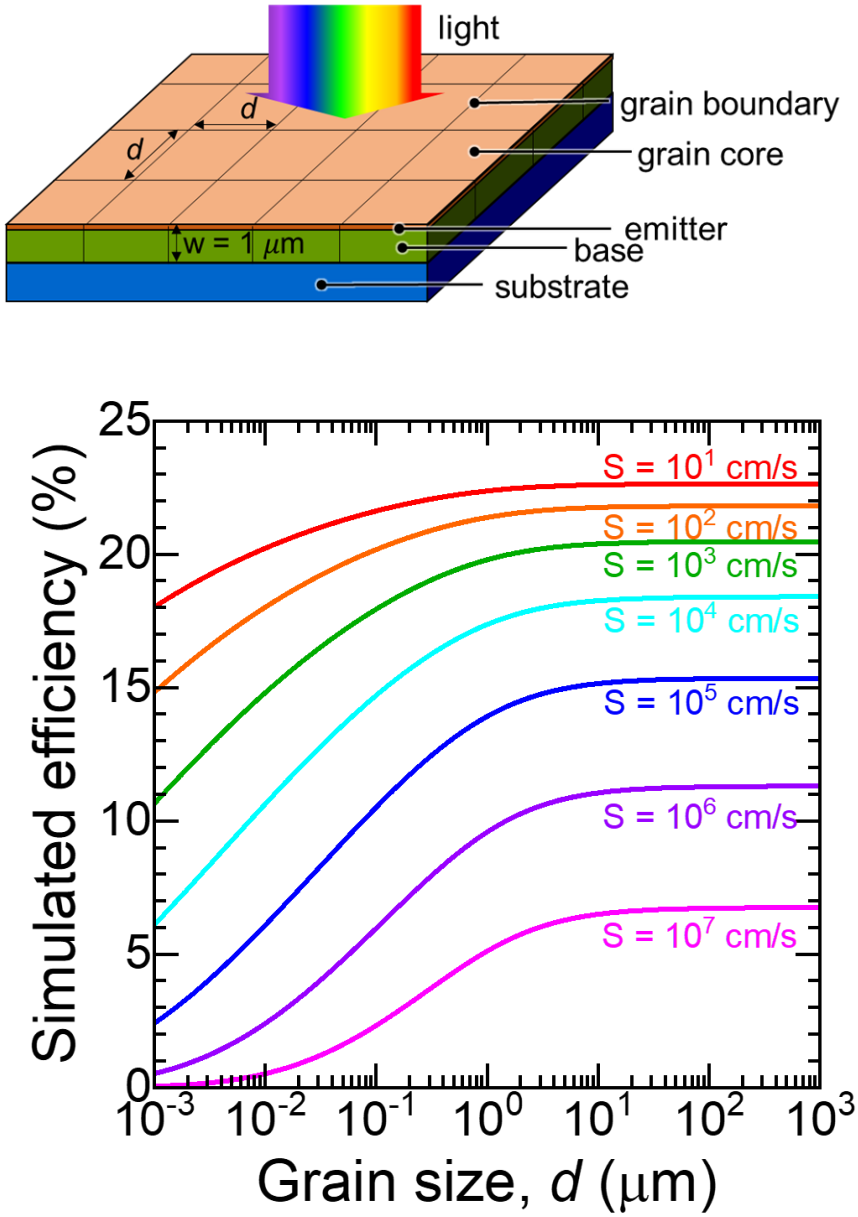

Fig. 3.9 Effect of grain size on device efficiency for different assumed values of surface recombination velocities.

CHAPTER 4

RECOMBINATION KINETICS AT INTERFACES AND GRAIN BOUNDARIES

4.1. Introduction

Passivation of III-V compound semiconductors with bandgap larger than 1.8 eV has far reaching impacts in many fields related to power electronics and opto-electronics. Effectiveness of passivation can be quantified by measuring recombination velocity of minority charge carriers at various surfaces and interfaces of the structure. Finding ways to reduce surface recombination velocity of semiconductors has been an active area of research. One of the most effective ways to passivate a III-V compound semiconductor surface has been the epitaxial growth of a barrier layer that forms an appropriate type of heterointerface with the base layer. This barrier layer is usually of a higher bandgap than the base layer and is expected to reduce the density of dangling bonds at the surface. Formation of appropriate type of heterostructure also helps in repelling minority charge carriers away from the surface. This region is usually expected to have highest density of active defects in an epitaxially grown device structure. Passivation of surface of this higher bandgap barrier layer may further reduce the surface recombination velocity.

Single crystal GaAs is commonly passivated with GaInP and AlInP as barrier layers. GaInP is the first barrier layer that is grown on GaAs and AlInP is the second barrier layer that is grown on GaInP. Recombination velocity of GaInP-GaAs interface are reported to be <2 cm/s indicating excellent passivation [37]. In comparison, the surface recombination velocity of minority charge carriers in GaInP is usually <1000 cm/s [38, 39]. This value is reported for AlGaInP-GaInP interface. It is difficult to effectively passivate GaInP using multiple barrier layers because of many reasons. AlInP has the highest known bandgap amongst the III-V compound semiconductor that can be grown

lattice-matched to GaInP. This restricts the maximum valence band and conduction band offset at GaInP surface to 0.22 eV and 0.39 eV respectively [40]. It is also difficult to heavily dope AlInP. Also, aluminum containing compounds have affinity to water vapor, and therefore have a propensity to degrade in air over time. It is due to these reasons that a thick AlInP layer is needed to effectively passivate GaInP surface. Increasing the thickness of barrier layer increases the parasitic absorption of light. This is one of the unavoidable sources of efficiency losses in optical devices. With the advent of indoor low power electronic devices, there is an increase in need to improve the efficiency of indoor photovoltaic devices. Since the indoor light spectrum usually has a much larger share from shorter wavelengths than in sunlight, optical loses due to AlInP are amplified. This has led to exploration of various cap-passivation layers that may or may not be perfectly lattice matched to the underlying structure.

Other methods that passivate surfaces of III-V compound semiconductors like GaAs and InP are: 1) chemical bath deposition of electronegative elements like sulfur, fluorine, and iodine, and 2) growth of high-k dielectrics like Al_2O_3, SiO_2, TiO_2, HfO_2, etc. using atomic layer deposition. These alternate passivation techniques are hypothesized to reduce defect density and/ or minority charge carrier concentration at the surface. While these techniques have been used to passivate surfaces of semiconductors like silicon, gallium arsenide, and indium phosphide, less is known about their effect on surfaces of high-bandgap phosphide materials like GaInP and AlInP. In this chapter, we investigate the effect of such surface treatments on recombination velocity at GaInP surface.

4.2. Experimental Details

4.2.1. Processing details

A set of four GaInP-based double heterostructures with varying base thicknesses – 709 nm, 460 nm, 320 nm or 250 nm – was used in this study. Samples which have not undergone any etching are hereafter called as-grown samples. To study the effect of various passivation techniques, first, the GaAs cap layer in the as-grown samples is etched using $NH_4OH:H_2O_2:H_2O$::10:4:500 solution for 60 seconds. Hereafter, these samples are referred as GaAs-etched samples. These GaAs-etched samples are expected to have Al, In, and P dangling bonds at the surface. Parts of GaAs-etched samples are treated with $HCl:H_2O$::1:1 solution for 30 seconds. This treatment is expected to preferentially etch the top AlInP barrier layer and leave behind bare GaInP surface. These samples are hereafter referred to as AlInP-etched samples. All the as-grown, GaAs-etched, and AlInP-etched samples undergo identical passivation treatments.

Selectivity of the etchants used to remove the GaAs cap layer and AlInP barrier layer was ensured by measuring the height of the step between the etched and un-etched region. Two sets of samples were created for this study. One set of samples were etched using only $NH_4OH:H_2O_2:H_2O$::10:4:500 solution for 30, 60 and 300 seconds. Etching reaction was stopped by immediately rinsing the samples with deionized water for 60 seconds. This set of samples is used to study the selectively etching of the GaAs cap layer. Second set of samples were used to ensure the selective etching of AlInP layer using $HCl:H_2O$::1:1 solution. These samples underwent two etching steps: $NH_4OH:H_2O_2:H_2O$::10:4:500 solution for 60 seconds followed by $HCl:H_2O$::1:1 solution for 10, 30, 60 and 300 seconds. Samples were rinsed after each etching step to ensure that etching stops completely after each step. Height of step between the etched and unetched region was measured using atomic force microscopy.

A set of studied GaInP double heterostructures has 12 samples – the as-grown, GaAs-etched, and AlInP-etched samples each with four GaInP-base thicknesses. This chapter presents the effect of different dielectric layers on surface recombination velocity of GaInP. The studied passivation layers are aluminum oxide and hafnium oxide deposited using atomic layer deposition, and silicon nitride layer deposited using plasma enhanced chemical vapor deposition. These layers are expected to vary the surface charge, and/ or defect energy state density at the GaInP surface.

4.2.2. Characterization details

The effect of the various passivation treatments on bulk minority carrier lifetime (τ_{bulk}) and interface recombination velocity (IRV) is quantified using time resolved photoluminescence spectroscopy (TRPL). TRPL is used to measure effective minority carrier lifetime (τ_{eff}). This τ_{eff} depends on base thickness w through: [41, 42]:

$$\frac{1}{\tau_{eff}} = \frac{1}{\tau_{bulk}} + \frac{1}{\frac{w^2}{\pi^2 D} + \frac{w}{S_{front} + S_{back}}} \tag{4.1}$$

here D is the minority carrier diffusion coefficient. In many cases, $\frac{(S_{front}+S_{back})w}{\pi^2 D} \ll 1$, so the equation is simplified to:

$$\frac{1}{\tau_{eff}} = \frac{1}{\tau_{bulk}} + \frac{S_{front} + S_{back}}{w} \tag{4.2}$$

τ_{bulk} has contributions from radiative recombination, and trap-assisted recombination.

Change in radiative efficiency of double heterostructures due to the various passivation treatments is qualitatively measured using steady-state photoluminescence spectroscopy.

4.2.3. Equipment details

The epitaxial DH-structures were grown in a metal organic vapor phase epitaxy reactor. Each growth was carried out on two 4" GaAs wafers that were loaded on a planetary substrate rotation assembly. GaInP-based double heterostructures with 20nm thick AlInP barrier layers were grown on 400 nm thick GaAs buffer layer. The active GaInP base layer thickness was varied (709 nm, 460 nm, 320 nm or 250 nm) to separate the influence of interface recombination velocity to bulk lifetime. Triethylgallium (TEGa), trimethylindium (TMIn), trimethylaluminum (TMA) and tertiarybutylphosphine (TBP) were employed as III-V precursors and diethyltellurium was used for doping the films n-type. GaInP and AlInP were doped to the levels of 8×10^{16} cm^{-3} and 6×10^{18} cm^{-3} respectively.

Aluminum oxide was deposited as a 10 nm layer using Cambridge savannah atomic layer deposition (ALD) tool. Trimethylaluminum (TMA) and water vapor is used for deposition and oxidation of aluminum. Nitrogen with flowrate of 20 sccm is used as the carrier gas. TMA and H_2O exposure steps are for 15 milliseconds each. There is also a 15-second pause after every TMA exposure step and H_2O exposure step. Each deposition/oxidation cycle deposits 0.1 nm of aluminum oxide film.

A custom-built TRPL setup is used to measure the decay of photogenerated minority charge carrier concentration in DHs. Electron and holes were generated using femtosecond pulses of photons with wavelength of 532 nm. This TRPL setup is capable of measuring decay lifetimes above 40 picoseconds and has an instrument response function with a full width at half maximum value of approx. 100 picoseconds.

4.3. Results and analysis

4.3.1. Baseline measurements

Selectivity of the etchants used to remove the GaAs cap layer and AlInP barrier layer is illustrated in Fig. 4.1. Step height between the etched and unetched regions is approx. 50 nm after removal of GaAs and is approx. 75 nm after removal of the cap GaAs layer and the barrier AlInP layer. Step heights are independent of the duration for which the films are dipped in the etching solutions. This confirms that the etchants used in this study selectively etch each layer. Based on the growth parameters, the expected thickness of GaAs and AlInP layers is 50 nm and 20 nm respectively. The step heights measured after etching GaAs and AlInP layers align well with the expected values.

Effect of etching the cap-GaAs layer and the barrier-AlInP on steady state photoluminescence (PL) response is shown in Fig. 4.2. The integrated PL peak intensity

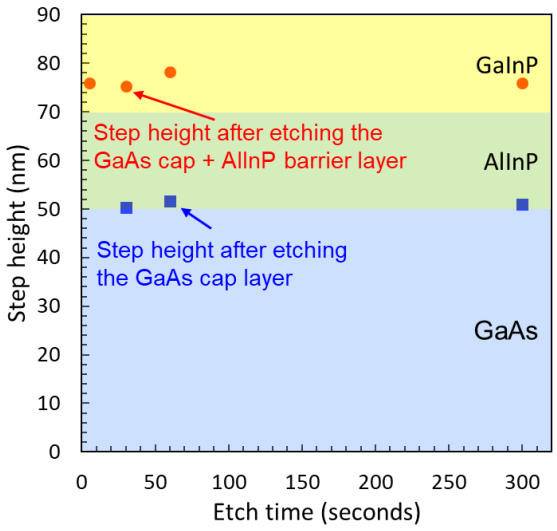

Fig. 4.1 Selective etching of GaAs cap layer and AlInP barrier layer was confirmed by measuring step height between etched and unetched region.

of as-grown sample, GaAs-etched sample and AlInP-etched sample are 1.56×10^5, 1.98×10^5, and 6.29×10^3 respectively.

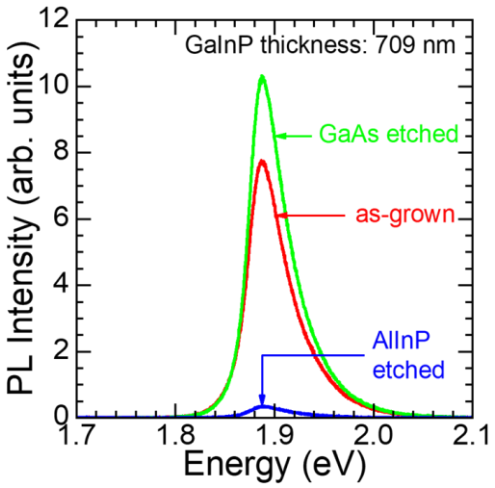

Fig. 4.2 Baseline steady state photoluminescence spectroscopy after etching the GaAs-cap and AlInP-barrier layer

For a constant incident photon flux of the 532 nm laser, GaAs-etched sample is 1.3× more luminescent than the as-grown sample while the AlInP-sample is just ~4% as luminescent as the as-grown sample. The cap-GaAs layer affects the luminescence of heterostructure in two ways:

1. Removal of the cap-GaAs layer is expected to increase the photoluminescence response of the GaInP-DH because GaAs absorbs almost half of the total incident and radiated photons. Etching the GaAs cap layer is expected to increase the photogenerated electron and hole pair by a factor of 2 if the surface recombination velocity remains constant.
2. Removal of the cap-GaAs layer may reduce the intensity of the photoluminescence response from GaInP if the barrier-AlInP is not doped high

enough or is not thick enough. Removal of GaAs could increase the surface recombination velocity. This would reduce the equilibrium electron and hole carrier concentration and therefore reduce the photoluminescence intensity.

An increase in photoluminescence of GaInP only by a factor of 1.3 suggests an increase in the GaInP surface recombination rate after GaAs removal.

Since AlInP layer has an indirect bandgap of 2.33 eV, it is not expected to absorb any incident or emitted photons. Therefore, removal of AlInP is expected keep the incident photon flux constant. Change in photoluminescence intensity is expected to be controlled to a large extent by the change in surface recombination velocity. Reduction in photoluminescence intensity by almost 96% indicate – amongst other things – a drastic increase the surface recombination velocity.

A direct measurement of the effective minority charge carrier lifetime τ_{eff} helps to ascertain the reason for the decrease in the integrated photoluminescence intensity. τ_{eff} is extracted from the photoluminescence decay curves, and are shown in Fig. 4.3 for n-

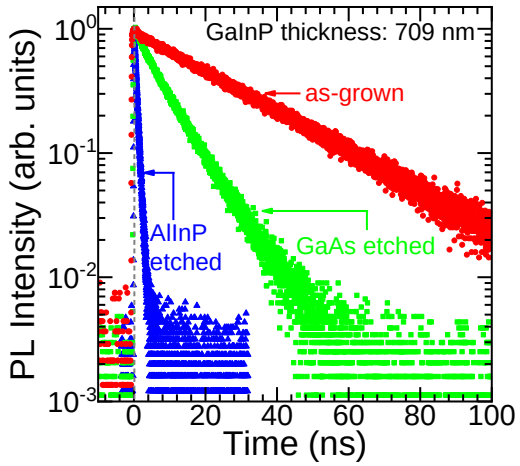

Fig. 4.3 Baseline time resolved photoluminescence spectroscopy after etching various layers.

type AlInP/GaInP/AlInP DH. Since the FWHM of the laser pulse used for excitation of charge carriers is much less than the lowest measured lifetime values, the effective carrier lifetime can be directly extracted from the single-exponential part of the decay curve. The as-grown, GaAs-etched and AlInP-etched GaInP DH sample with a base thickness of 709 nm has effective carrier lifetime of 26.9 ns, 10.5 ns and 0.77 ns respectively.

Carrier lifetime is a direct measure of recombination rate in a double heterostructure. Decrease in effective carrier lifetime after etching the GaAs cap layer indicates increase in the rate of non-radiative rate of recombination. Removal of the AlInP barrier layer reduces the effective carrier lifetime further. This suggests that AlInP layer is either not thick enough or doped high enough to effectively shield the minority charge carriers from recombining at the defect sites on AlInP surface.

Surface recombination velocity is related to the effective carrier lifetime through Eq. (4.1). It is expected that the etching processes would not affect the diffusivity and decay lifetime of minority charge carriers in GaInP-base layer. Therefore, effective carrier lifetime can be expressed as a function of surface recombination velocity. SRV for all the cases could be estimated using SRV value for any one case, the bulk carrier lifetime and hole diffusivity in GaInP-base layer (expected to remain same for the samples), and the effective carrier lifetime values measured using PL decay curves.

To extract the bulk carrier lifetime using the as-grown AlInP/GaInP/AlInP DH structures, it can be assumed that $S_{front} = S_{back} = S$. Eq. (4.2) simplifies to

$$\frac{1}{\tau_{eff}} = \frac{1}{\tau_{bulk}} + \frac{2S}{w} \tag{4.3}$$

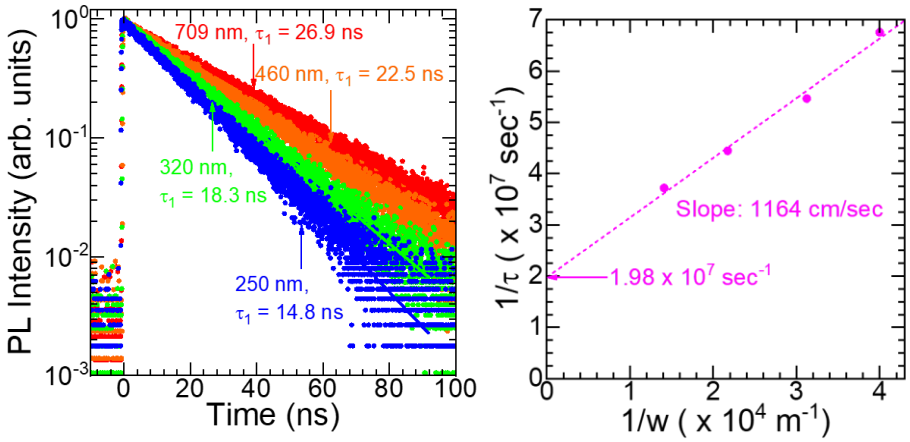

Fig. 4.4(a) PL decay plots of as-grown GaInP-based double heterostructures, and (b) measured effective carrier lifetime data from TRPL and base thicknesses of the samples.

Figure 4.4(a) shows photoluminescence decay plots of the as-grown GaInP DH structures with varying base thickness. Effective carrier lifetimes of 26.9 ns, 22.5 ns, 18.3 ns, and 14.8 ns are extracted for sample with base thickness of 709 nm, 460 nm, 320 nm and 250 nm respectively. Fig. 4.4(b) plots the measured effective carrier lifetime data from TRPL and base thicknesses of the samples on axes of $\frac{1}{\tau_{eff}}$ *vs.* $\frac{1}{w}$. The data falls on a straight line. A straight-line fit to these data points is used to extract $\frac{1}{\tau_{bulk}}$ (y-intercept at x=0) and S (slope of the line). For as-grown samples, τ_{bulk} is measured to be 50.5 ns and front- and back-surface recombination velocity is measured to have a value of 582 cm/s.

A similar analysis is carried out on AlInP-etched samples. In these cases, it is assumed that S_{back} is same as that extracted in as-grown samples. For AlInP-etched samples, PL decay curves shown in Fig. 4.5(a) are primarily governed by minority carrier recombination at the bare unpassivated GaInP surface. Measurement of effective carrier

lifetime in samples with varying GaInP thickness is used to extract the recombination velocity of the front surface and diffusivity value of the minority charge carrier (holes) in the bulk region of GaInP using Eq. (4.1). Eq. (4.1) can be rearranged as:

$$\left(w.\left(\frac{1}{\tau_{eff}}-\frac{1}{\tau_{bulk}}\right)\right)^{-1} = \frac{w}{\pi^2 D}+\frac{1}{S_{front}} \tag{4.4}$$

On the left-hand side of the equation, τ_{eff} is measured from the single-exponential part of the PL decay curve, thickness of the base GaInP layer is known from the well optimized growth parameters, and τ_{bulk} is assumed to be same as that measured in the as-grown sample. For sake of convenience, hereafter the left side of Eq. (4.4) is referred to as modified effective charge carrier lifetime. Variation in modified effective charge carrier

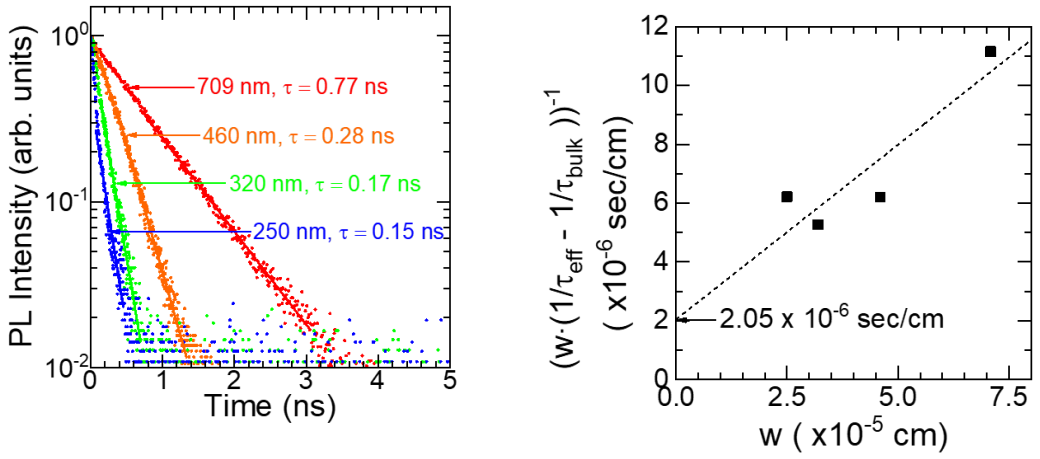

Fig. 4.5(a) Photoluminescence decay curves GaInP-AlInP heterostructure with no top barrier layer and with varying thickness of the base GaInP layer, and (b) modified carrier lifetime is plotted with respect to width of the GaInP base layer to extract recombination velocity at the GaInP surface (y-intercept of the linear-fit line to the data) and diffusivity of minority charge carriers in the GaInP-base layer (extracted from the slope of the linear-fit line to the data)

lifetime due to change in the thickness of GaInP-base layer is plotted in Fig. 4.5(b). A least-square regression straight line is fit to the four data points. The y-intercept of the fit line and its slope can be used to extract the surface recombination velocity S_{front} and diffusivity of minority charge carriers in GaInP bulk region.

S_{front} for bare GaInP surface is measured to be 4.5×10^5 cm/s and the diffusivity of minority charge carrier is measured to have a value of 0.85 cm^2/s. Effect of all the surface treatments – presented in the following section – on recombination velocity at GaInP surface will be compared to the baseline value of the bare-GaInP surface calculated here.

4.3.2. Surface treatments

30 nm silicon nitride layer is grown on as-grown, GaAs-etched, and AlInP-etched samples using plasma enhanced chemical vapor deposition. No change in carrier lifetime is observed in as-grown samples. Fig. 4.6(a) shows the layer structure expected before and after silicon nitride deposition. A typical change in PL decay curve after deposition of silicon nitride on GaAs-etched samples is shown in Fig. 4.6(b). These curves are used to extract effective carrier lifetimes for various GaInP-base layer thicknesses that are summarized in Fig. 4.6(c). The figure indicates a consistent reduction in effective carrier lifetime after silicon nitride deposition on AlInP surface. Silicon nitride deposition on bare GaInP surface showed only marginal reduction in effective carrier lifetime. Since the surface recombination velocity is so high that it is governed by the diffusivity of holes towards the surface, Eq. (4.4) is used to extract its exact value. Plot of modified effective carrier lifetime against base-layer thickness of silicon nitride-deposited AlInP-etched samples is shown in Fig. 4.7 (b).

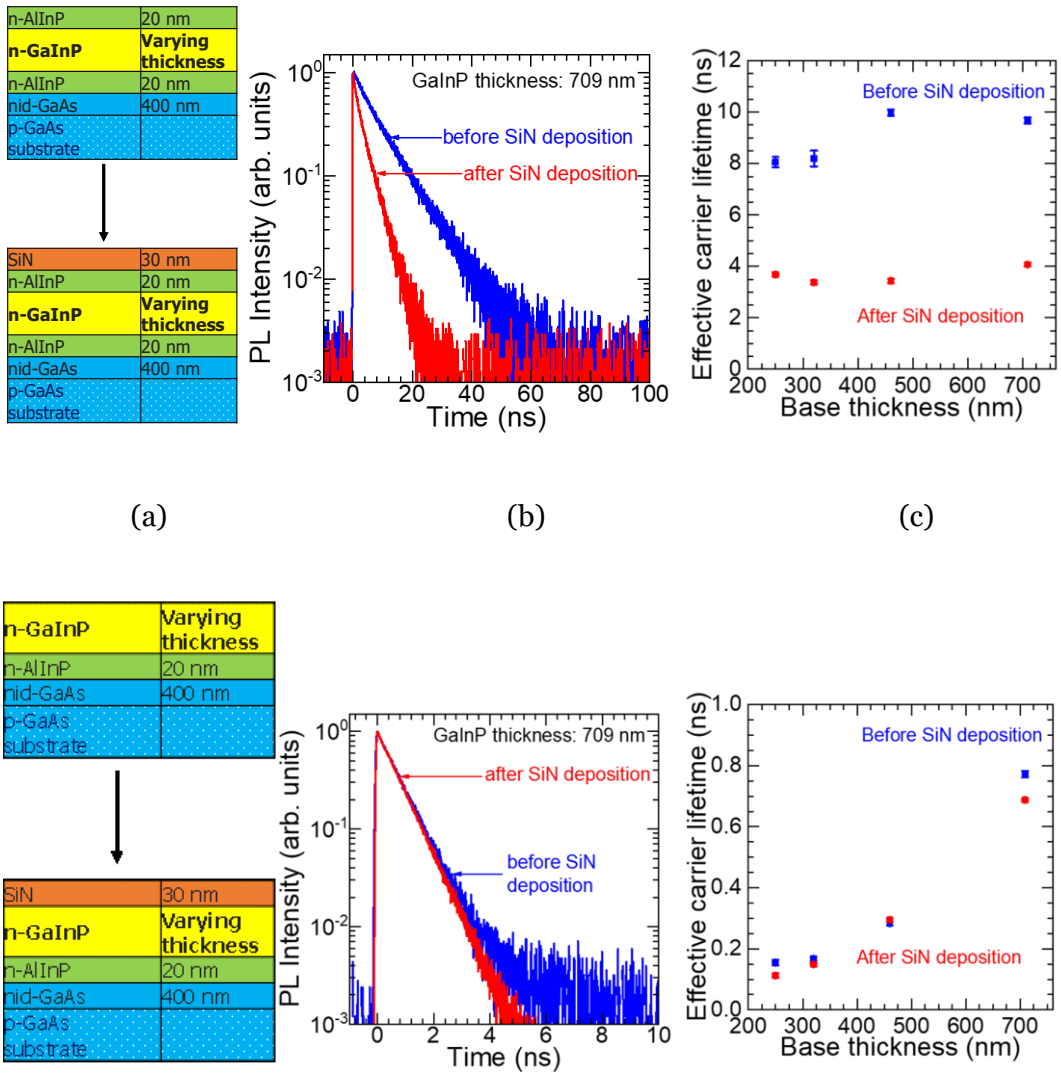

Fig. 4.6 Structure of (a) GaAs-etched samples and (d) AlInP-etched samples before and after silicon nitride deposition; PL decay curves of (b) GaAs-etched sample and (e) AlInP-etched sample with a GaInP-base thickness of 709 nm, and summary of change in effective carrier lifetime after silicon nitride deposition on (c) GaInP-etched and (f) AlInP-etched samples

PL decay curves after deposition of 10 nm thick Al_2O_3 and 10 nm thick HfO_2 using atomic layer deposition of AlInP-etched samples are shown in Fig. 4.7 (c) and (e) respectively. Since the effective carrier lifetimes are similar to that measured in the case of free GaInP-surface measurements, modified effective carrier lifetime is used to extract the surface recombination velocity of GaInP after deposition of the high-k dielectric layers. Plots of modified effective carrier lifetimes against base-layer thickness for Al_2O_3 and HfO_2 deposited AlInP-etched GaInP DH structures are shown in Fig. 4.7 (d) and (f) respectively.

4.4. Discussion

Surface recombination velocities (SRVs) after deposition of various high-k dielectric films on GaInP are summarized in Fig. 4.8. Also plotted is the SRV of the GaInP double-heterostructure with AlInP as the barrier layer and GaAs as the cap layer. SRV values for the case of dielectrics is very similar to that of the bare GaInP-surface. SiN_x and HfO_2 layer is expected to have a positive fixed charge, whereas Al_2O_3 is expected to have a negative fixed charge associated with it. In addition, oxidation of the GaInP surface before deposition of these dielectric films on the GaInP surface is also expected to impart a negative charge at the dielectric-GaInP interface. The minority charge carrier concentration at the dielectric-GaInP would only begin to invert if the effective surface charge is changed. Since the defect density at the dielectric-GaInP is much greater than the fixed charge present in the dielectric films, the recombination rate remains relatively unaffected with change in the polarity of the fixed charge of the dielectric films.

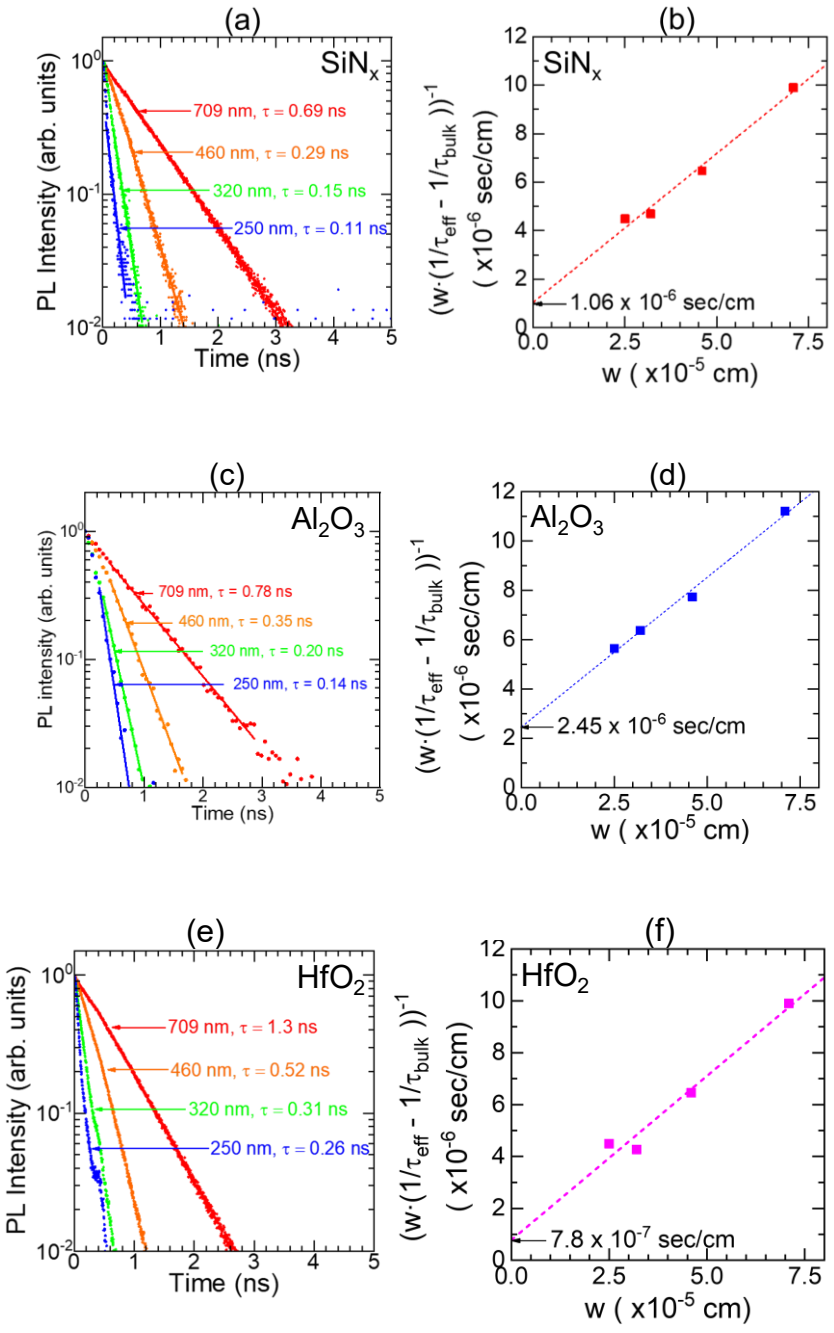

Fig. 4.7 Modified lifetime vs. base thickness for SiN coated AlInP-etched GaInP double-heterostructures.

4.4.1. Conclusion

AlInP layer demonstrated excellent passivation ability when capped with GaAs. Surface recombination velocity of 584 cm/sec and a bulk lifetime of 50 ns was measured using time resolved photoluminescence decay measurements. Decrease in the effective minority charge carrier lifetime on removal of the cap-GaAs layer suggests that the AlInP needs to be either thicker or more heavily doped to shield the effect of defect at its surface from affecting the charge carrier distribution in GaInP. Recombination velocity at the free GaInP surface is measured to be 4.5×10^5 cm/s. The recombination velocity appears to be

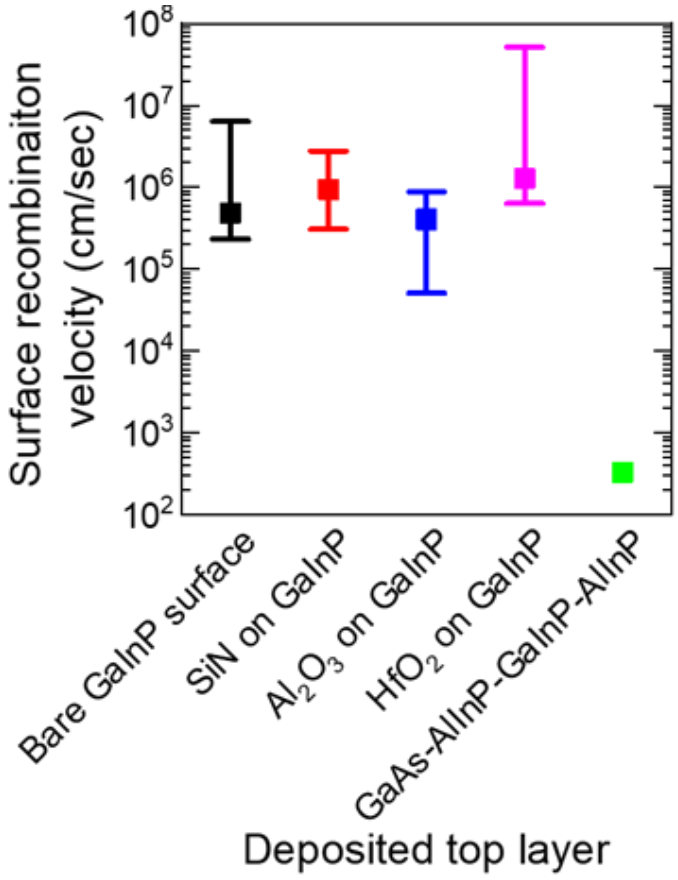

Fig. 4.8 Summary of the extracted surface recombination velocities after deposition of various layers.

governed by the diffusivity of minority charge carriers towards this surface. Diffusivity of minority holes was measured to be 0.85 cm^2/s. Deposition of high-k dielectric layers did not appreciably change the recombination velocity. This is conjectured to be due to the high defect density at the dielectric-GaInP interface. Reducing the defect density at the interfaces using other ionic or organic compounds could compensate for the surface defects, and therefore reduce the recombination at GaInP surface.

CHAPTER 5

DEFECT ENERGY STATE DENSITY AND BAND BENDING IN POLYCRYSTALLINE COMPOUND SEMICONDUCTORS

This chapter explores the defect characteristics of three material systems. In the past, these material systems – CdTe, $CuIn_{1-x}Ga_xSe_2$ and InP – have been used to fabricate solar cells with high power conversion efficiency.

5.1. Evolution of surface potential across CdTe grain boundaries with varying $CdCl_2$ post deposition treatment temperature

5.1.1. Introduction

CdTe based solar cells are one of the most widely used thin film polycrystalline solar cells for terrestrial applications with an estimated market share of ~5% by total sales and has a highest reported conversion efficiency of 22.1%. One of the critical steps in the fabrication of CdTe based solar cells is the $CdCl_2$ post deposition treatment. This step is reported to have increased the total power conversion efficiency by over 10% in absolute number. The effect this step has on the grains and grain boundaries of CdTe thin film and the various interfaces in the device has been a subject for many studies in the past. This treatment has shown to aid CdTe recrystallization and improve the macroscopic properties like photoluminescence and carrier lifetime[43]. Studies using atom probe tomography and electron energy loss spectroscopy have found evidence of chlorine segregation at the grain boundaries [44, 45]. This is predicted to lower the valence band edge near the grain boundaries in the process creating a local n-type region at and around the grain boundaries. McCandless et. al. studied the cross section of a working CdTe cell using KPFM technique [46]. The study has found strong evidence that suggests a reduction in majority charge carriers near the grain boundary region. While there have

studies have suggested a critical role this band bending at CdTe grain boundaries and $CdCl_2$ post deposition treatment plays in improving the power conversion efficiency of the cells, little is known about the effect of $CdCl_2$ post deposition treatment temperature on band bending at the grain boundaries. This study presents a study of evolution of surface potential distribution in CdTe with varying $CdCl_2$ post deposition treatment temperature.

5.1.2. Experimental details

To qualitatively understand band bending at the grain boundaries, Kelvin probe force microscopy (KPFM) is used to measure the local work functions. CdTe absorber layers were grown using the standard closed space sublimation method [47] on a TCO coated soda-lime glass (TEC10). The films were then processed at varying temperatures during the $CdCl_2$ post deposition treatment. The $CdCl_2$ PDT temperatures were 380°C, 390°C, 400°C, 420°C, 440°C and 460°C.

To protect the surface properties of the grown films, the samples were then stored in a vacuum seal until just before the KPFM and C-AFM studies. KPFM and cAFM studies were carried out using a Bruker Multimode 8 atomic force microscope. A standard Pt-Ir coated tip with tip diameter of approx. 25 nm and a spring constant of 2.8 N/m was used to carry out these measurements. Amplitude modulated KPFM studies were carried out using a dual pass technique in which during the first scan topography line profile is mapped. The topography is traced with a lift height of 20 nm in the second pass during which time an AC-bias voltage is applied at the resonant frequency of the cantilever. The applied V_{DC} to the tip to offset the surface potential is the contact potential difference (V_{CPD}). This could be used to determine the relative change in the surface potential across grain boundaries. A standard sample of Au-Si was used as calibration standard before every run. cAFM studies were carried out in the contact mode. Same tip is used for KPFM and cAFM studies.

5.1.3. Results and discussion

At low processing temperatures of 380°C and 390°C the contact potential difference at the grain core is observed to be lower than that at grain boundaries. With increase in post deposition treatment to up to 440°C, the contact potential difference becomes more uniform. At 460°C it was observed that the contact potential difference at grain cores was higher than that at the grain boundaries. It is at these processing temperatures that CdTe solar cells demonstrate high device performance, photoluminescence intensity and

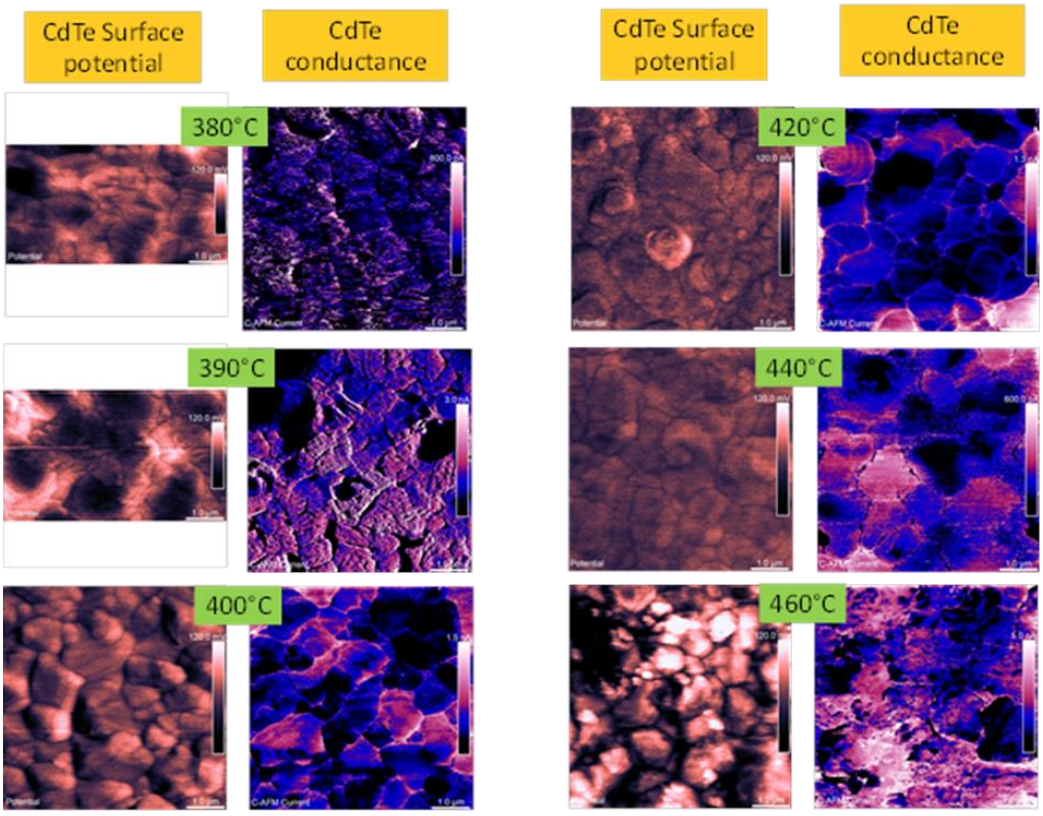

Fig. 5.1 Surface potential and conductance plots of CdTe films having undergone $CdCl_2$ PDT treatments at various temperatures.

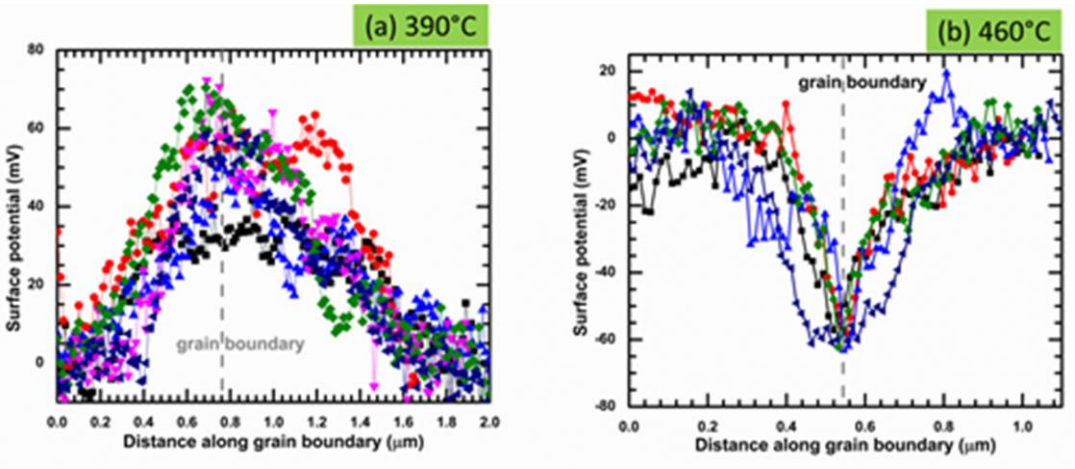

Fig. 5.2 Surface potential line scans for samples undergoing $CdCl_2$ PDT at (a) 390°C and (b) 460°C are averaged. The net change in potential difference between grain boundary & grain core is observed to be +56 mV and -62 mV respectively.

minority carrier lifetime. It needs to be noted that the variation in contact potential difference could be a result of multiple factors, some of them being: (i) variation of electron affinity (due to surface dipole or variation in doping or charge carrier concentration), (ii) variation of work function or bandgap(due to change in bonding at interfaces) or (iii) variation in strains (particularly at the grain boundary relative to grain core). The overall effect is a combination of all these factors. Since past CdTe passivation studies have found evidence of chlorine at the grain boundaries after $CdCl_2$ post deposition treatment, a major contributor to the inversion of relative contact potential difference between grain core and grain boundaries could be attributed to variation in doping or equivalently electron affinity near the grain boundaries.

5.2. Surface potential measurements of polycrystalline indium phosphide thin films grown using thin film vapor liquid solid method.*

5.2.1. Introduction

Indium phosphide (InP) is a III-V semiconductor with a direct band gap of 1.34 eV, near the optimum value for a single-junction solar cell. Furthermore, it has relatively low unpassivated surface recombination velocity and high electron mobility. These properties make InP a very promising material for concentrator solar cell applications [48]. Efficiency as high as 22.1% has been reported for single crystal InP cells [49], but the higher capital cost of conventional III-V growth technology compared to silicon technology has inhibited scale up of III-V solar cells.

In addition to the properties above, a high absorption coefficient ($> 10^4$ cm^{-1}) makes InP thin film an attractive option for solar cells [50]. A recently developed thin film vapor-liquid-solid (TF-VLS) growth technique presents a cost effective and scalable way to synthesize high quality polycrystalline InP thin film with grain sizes as large as several hundred microns [48, 51, 52, 8, 53]. A solar cell efficiency of 12.1% at 1-sun intensity (AM 1.5G) has been reported for a single junction cell using TF-VLS grown InP as absorber layer [53].

---

*Parts of this section have been published as

A. Chikhalkar, A. Fischer, M. Hettick, A. Javey, and R. R. King, "Investigation of InP defect characteristics grown using novel TF-VLS technique," IEEE 44th Photovoltaics Specialists Conference Proceeding (2017).

To improve the efficiency further and to understand the limitations of this technique, it is important to understand the role of grain boundaries and defects on the optoelectronic properties of the TF-VLS material. Photoluminescence (PL) imaging and electron beam induced current (EBIC) have been carried out previously to show grain structure and grain boundaries [48] at the micron scale.

5.2.2. Experimental details

Figure 5.3 shows a schematic of the TF-VLS process for the growth of InP. A 3-µm-thick pure indium film is evaporated on molybdenum coated glass. A 40 nm SiO_2 layer is then deposited on the indium before phosphorization at high temperatures. The as-grown InP samples show n-type behavior. The n-type samples being characterized were obtained by skipping the Zn doping stage, and continuing etching of the capping SiO_2 layer. The p-type samples were obtained by incorporating Zn in InP using vapor-phase liquid-source doping.

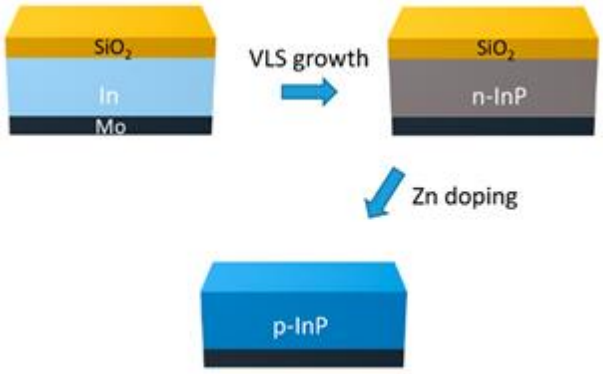

Fig. 5.3 Schematic of TF-VLS process for the growth of Zn doped InP

In this study, grain boundary conductivity and surface potential at grain boundaries is studied using conductive atomic force microscopy (cAFM) and Kelvin probe force microscopy (KPFM). cAFM and KPFM were carried out using a 20-nm Pt-Ir tip in a Bruker Multimode 8 AFM system.

5.2.3. Results and Discussion

It is observed that current through the grain core changes with voltage, following the expected semiconductor behavior of InP. Grain boundaries appear to be very insulating. This behavior may be due to band bending near the grain boundaries which could create

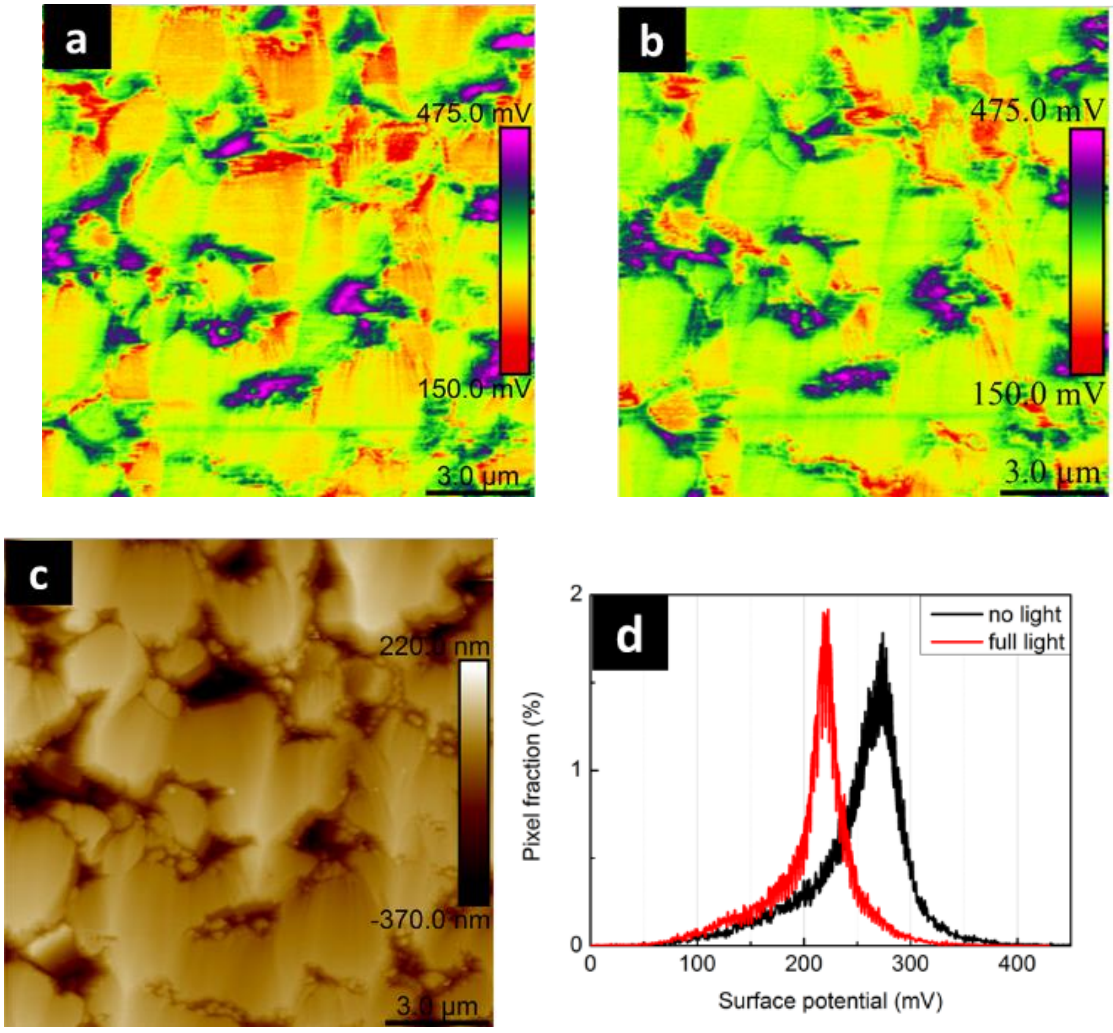

Fig. 5.4 Surface potential (a) without illumination and (b) with illumination. (c) surface morphology and (d) change in the distribution of electric potential across the surface resulting from illumination.

a local intrinsic region, thereby reducing the conductivity around grain boundaries drastically.

Surface potential measurements of polycrystalline InP film before Zn doping is plotted in Fig. 5.4. Part (a) is the surface potential in dark and part (b) is the surface potential map with white light illumination. Fig. 5.4(d) shows the distribution of We observe that the surface potential is approximately 220 meV. Using work function values of the Pt/Ir AFM tip (φ_m~5.4eV) and the surface potential value, the Fermi level at the surface is estimated to be ~5.62eV. We observe that the potential near grain boundaries increases to approximately 270 meV, suggesting that the bands bend by 50 meV at the grain boundaries. These number are only qualitative as the defects at the surface and the finite distance between tip and surface change the effective force felt by the tip.

Incidence of white light has shown to reduce the potential over most of the surface area as well as the average grain boundary potential. This behavior is expected since the material is lightly n-doped, and addition of equal number of electrons and holes will move the Fermi level toward the valence band. We also observe that the change in potential in the grain core is much more pronounced than near the boundary, indicating that the trap state density tends to pin the Fermi level at the grain boundary.

5.2.4. Conclusion

Drop in the conductivity near grain boundaries as measured by conductive AFM may be caused by the formation of a depleted region near the grain boundaries due to band bending. However, measurements analysis of band bending at grain boundaries by Kelvin probe force microscopy indicate only a 50 meV rise in conduction and valence bands at the grain boundaries, typically not enough to cause the dramatic contrast between conduction in the grain cores and insulating behavior at the grain boundaries. The

measured ΔCPD_{gb} thus needs to be corrected considering the averaging effect of KPFM. A correction factor of 2-5 needs to be applied considering a lift height of 5 nm [54]. Engineering the grain boundary structure to increase the band bending could be used to shield photogenerated carriers from recombining readily, improving solar cell performance in this polycrystalline InP material.

5.3. Probing defect distribution in CuInSe2-based polycrystalline semiconductors using drive level capacitance profiling.*

Copper indium gallium diselenide (CIGS) based thin film solar cells have demonstrated power conversion efficiency of over 22% with a single-junction architecture [55]. CIGS compounds have a tunable bandgap from 1.0 eV (CIS) to 1.7 eV (CGS), and hence are one of the most suitable candidates for tandem cell architecture. However, addition of gallium beyond approximately 35% is found to degrade the device performance significantly. Understanding and engineering defects in CIGS compounds with higher gallium concentration could help realize the potential of CIGS-based solar cells as efficient top cell absorbers in low-cost tandem cells.

Previous research has found that the addition of silver significantly reduces the defect density in CIGS compounds with various gallium concentrations [14]. While addition of

---

* *Parts of this section have been published as

A. Chikhalkar, M. Goryll, W. Shafarman, and R. R. King, "Study of wavelength-resolved light-induced metastable defects in (Ag,Cu)(In,Ga)Se_2 thin films using capacitance based methods," IEEE 46th Photovoltaics Specialists Conference Proceeding (2019).

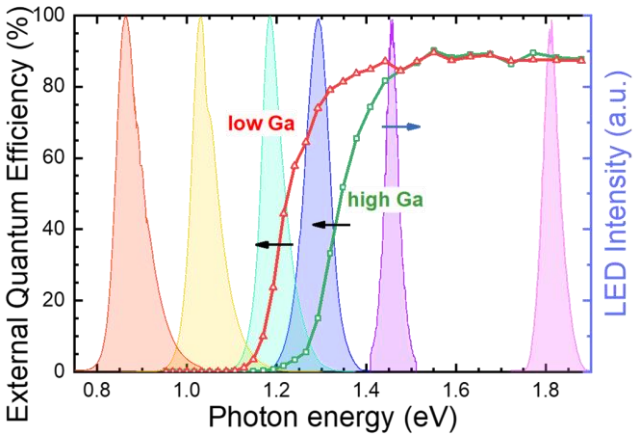

Fig. 5.5 Plot of External Quantum Efficiency of the studied cells with higher and lower gallium content along with the normalized spectrum of LEDs used to illuminate the sample.

silver – which substitutionally replaces copper – slightly increases the bandgap of the CIGS alloy, the reduction in defect density is attributed to the lower melting temperature of the silver alloy than its counterpart [56]. Earlier studies using drive level capacitance profiling (DLCP) indicate the free carrier density can be as low as 10^{14} cm^{-3} [57], and that the spatial location of defects is near the CdS/CIGS interface.

These studies also suggest that the defect formation mechanism in (A)CIGS alloys involve a bimolecular reaction [14, 58]. This was concluded by measuring the rate of increase in the drive level density after exposure to white light with the AM1.5G spectrum. The rise in the N_{DL} was observed to be proportional to (exposure time)$^{1/3}$. While the study quantified the role of white light exposure on the rise of overall defect density, the contribution of photons of various energies on defect creation is still unknown.

In this section, we investigate the light-induced creation of defects further, by exposing ACIGS samples to light with specific wavelengths, to examine the effect of defect formation measured by drive level capacitance on photon energy. The dependence of defect density

and free carrier concentration on photon flux and energy would enable the extraction of energy of formation of these metastable defects.

5.3.1. Experimental Details

The CIGS and ACIGS devices for this study were grown and fabricated at the Institute of Energy Conversion (IEC) at the University of Delaware. The $(Ag_yCu_{1-y})(In_{1-x}Ga_x)Se_2$ (ACIGS) films were grown by co-evaporating the five elements using a 3-stage process [56] on Mo-coated glass substrates, and are approximately 2 μm thick. No intentional silver gradient was introduced during the growth of the base layer and all the films were grown group-I poor with [Cu+Ag]/[Ga+In] = 0.8 – 0.9. To study the effect of gallium and silver concentration on the energy of formation of the light-induced defects, ACIGS films with ~37% and ~60% gallium were grown either with or without ~20% silver concentration. The area of all the devices studied was 0.4 cm^2.

An HP 4284A precision LCR meter having a frequency range of 20Hz – 1MHz was used to carry out both the admittance and drive level capacitance measurements. A Janis closed-cycle helium cryostat with a temperature range of 20K – 340K was used to vary the temperature. The schematic of the setup used is shown in Fig. 2.5. The cryostat is sealed in a vacuum chamber to avoid water condensation on the sample during capacitance measurement at low temperatures. The viewports of the vacuum chamber are shielded so that the sample does not get exposed to any stray light. Light-emitting diodes (LEDs) with varying wavelength ranges were used to expose the ACIGS samples to photons of different energies through the top window of the vacuum chamber, using a shutter to control exposure time. The top window has a transmittance of over 90% for all the photon energies used in this study. Multiple LEDs with peak emission energy of 0.86 eV to 1.81

eV are used, as shown in Fig. 5.5. The intensity of light incident on the samples from the LEDs was 10-15 mW/cm^2.

In this study, all the samples are annealed in dark at 330K for 3 hours before each series of temperature-dependent capacitance measurements. This annealing step resets the active defects. After annealing, the samples are cooled down to 60K and then gradually heated up in steps of 10 or 20K. At every step, the capacitance and conductance are measured at multiple frequencies between 20Hz to 1MHz. The DC bias voltage used during capacitance measurement is 0V with an AC signal amplitude of 50 mV. Upon detecting a step-like feature in the capacitance vs. frequency plot, the temperature is held constant, and drive level capacitance profiling is then used to measure the drive level defect density and spatial distribution of defects by varying the AC amplitude and the DC

Table 5.1. Summary of devices studied using admittance spectroscopy and drive level capacitance profiling.

Sample ID	**Ag%** $\left(\frac{Ag.100}{Ag+Cu}\right)$	**Ga%** $\left(\frac{Ga.100}{Ga+In}\right)$	**Jsc (mA/cm2)**	**Voc (mV)**	**Fill factor**	**Eff. (%)**	**Activation energy (E_{act})**
S00	0	37	31.5	672	74.5	16.2	47
S10	0	63	24.9	751	61.6	13.3	29
S01	24	37	31.1	704	77.6	17	138
S11	21	59	27.3	797	71.8	15.6	32

bias voltage at various frequencies. The AC amplitude and the DC bias voltage are varied in such a manner that $V_{dc} + V_{rms}$ remains constant. This measures the baseline defect state density before any light illumination. The sample is then exposed to light from one LED of a specific narrow wavelength range, with 10-15 mW/cm^2 optical intensity for 10 minutes. The capacitance with no DC bias and the drive level capacitance profile is then measured to quantify the effect of each narrow distribution of photon energy on the defect density. If a significant difference from the baseline is observed in the defect density, the sample is annealed again at 330K for 3 hours and the same process is followed again with an LED having a higher peak photon energy. The measured external quantum efficiency of the high and low gallium content films is also plotted in Fig. 5.5, showing the photon energies of the LEDs are both above and below the bandgaps of the devices studied.

The drive level density (N_{DL}) as obtained from the first two coefficients of capacitance dependence on amplitude of voltage signal (Eq. (2.11)) is the sum of the free carrier concentration and the defect density located at position $\langle x \rangle = \varepsilon A/C_o$ having an emission energy of $E_e = k_B T \, ln(\nu/2\pi f)$ is given by Eq. (2.12):

$$N_{DL} = -\frac{C_0^3}{2q\varepsilon A^2 C_1}$$

5.3.2. Results

The composition and performance summary for each of the devices studied are listed in Table 5.1. Fig. 5.6(a) shows the evolution of capacitance vs. frequency with increasing temperature. A step feature is visible in all the samples at temperatures below 180K. This step is observed to shift to higher frequencies with increasing temperature. The evolution of the inflection point frequency (f_i) in the capacitance profile with temperature is used to

extract the activation energy of the defects. Fig. 5.6(c) shows the Arrhenius plot of the inflection frequencies measured from the capacitance spectra of ACIGS sample S01 with

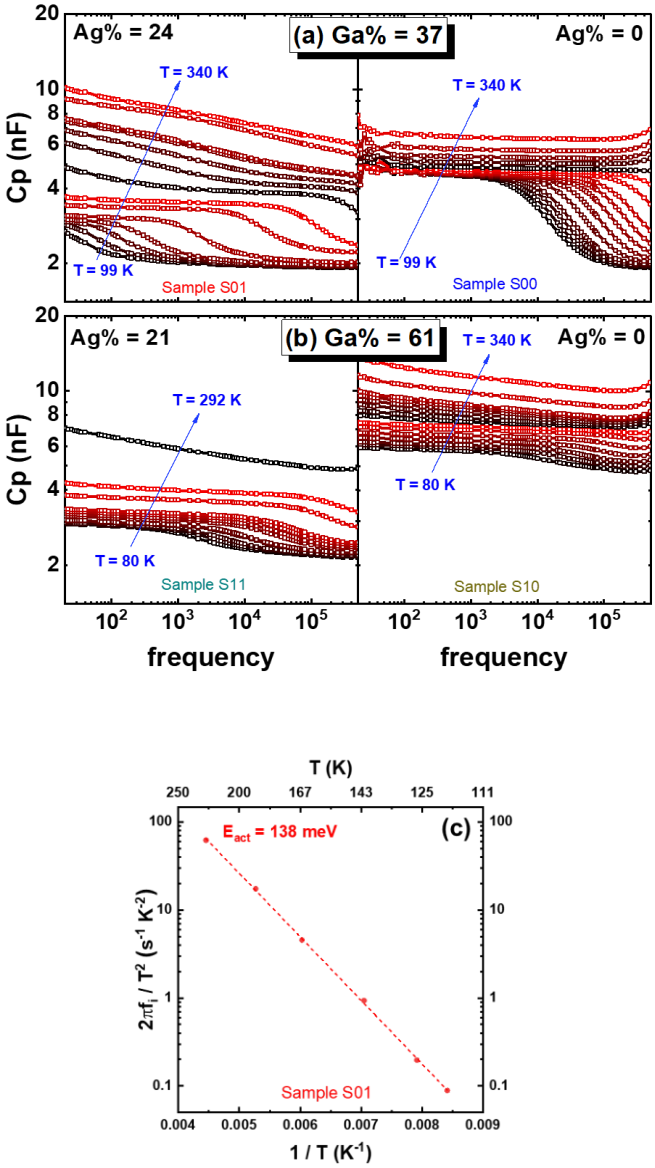

Fig. 5.6 (a, b) Capacitance vs. frequency plots of a matrix of ACIGS device compositions, highlighting step evolution with temperature consistent with the presence of bulk defects. (c) Arrhenius plot of the inflection frequencies from the capacitance spectra of sample S01 with 24% Ag, 37% Ga.

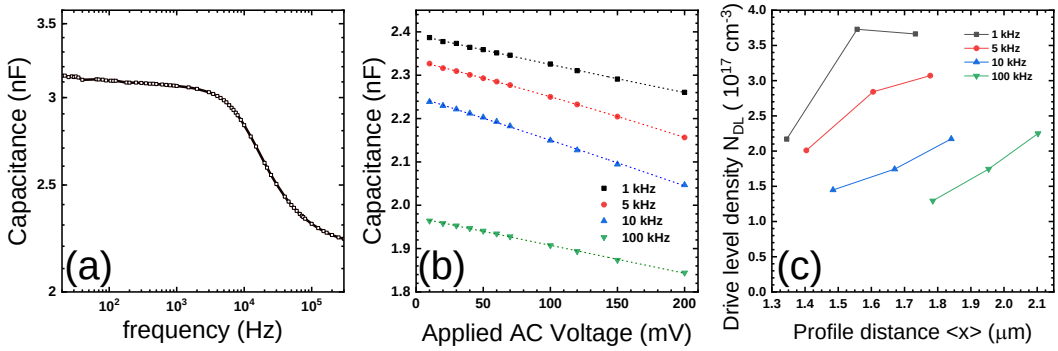

Fig. 5.7 (a) Capacitance vs. frequency plot of Sample S11 with V_{dc} = 0V and V_{ac} = 50mV. (b) Variation in capacitance with applied AC voltage, and (c) deep level density

24% Ag and 37% Ga. The compositions, light I-V measurements, and activation energies extracted are summarized for all the studied samples in Table 5.1

Figure 5.7 (a) shows a typical capacitance vs. frequency plot of the device with 24% Ag and 59% Ga 90K with no DC bias and an AC amplitude (V_{rms}) of 50 mV. In Fig. 5.7(b), capacitance vs. amplitude of the AC signal, at a nominal voltage ($V_{tot} = V_{dc} + V_{rms}$) of -500 mV. Equation (2.11) is used to fit the data in the capacitance vs. $V_{rms} = \delta V$ plot. The extracted values of C_0 and C_1 are then used to calculate the drive level density. The DLCP measurement at various voltages is used to estimate the spatial distribution of defects as shown in Fig. 5.7 (c). The difference in drive level density at low and high frequency for a nominal voltage of -400mV is ~1.0×10^{17} cm^{-3} which corresponds to the defect density in the material. Fig. 5.8 summarizes the baseline defect densities and their depth profile in various ACIGS devices. It is observed that the drive level defect density in CIGS devices is at least two orders of magnitude higher than their silver containing counterparts. Also, the defects responsive to the capacitance measurements are closer to the front surface in CIGS cells, while they are closer to the back surface in the silver alloys. The minimum

defect density measured using DLCP in various samples is summarized in the table below Fig. 5.8.

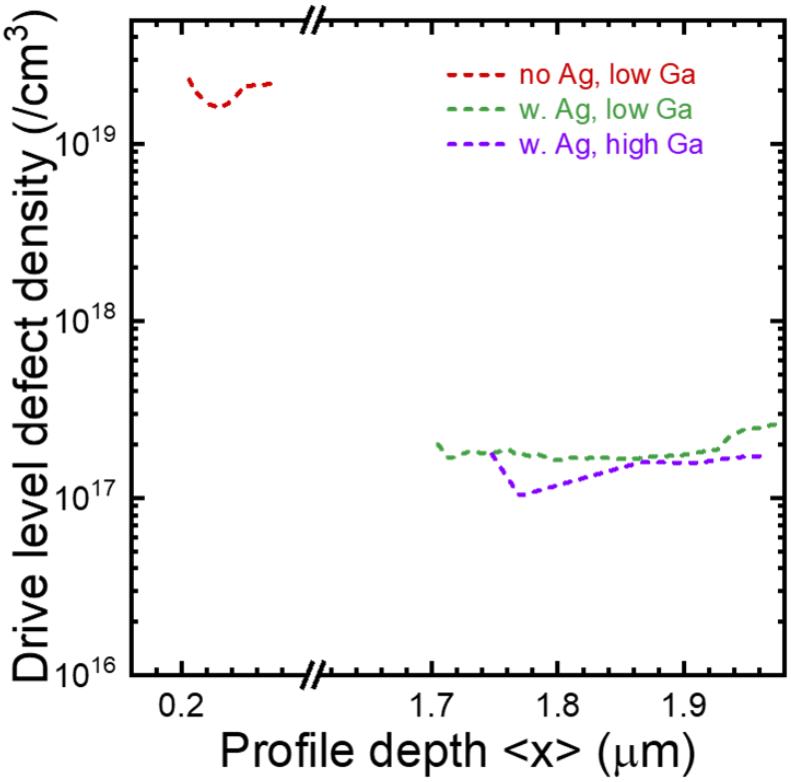

N_D (cm^{-3})	Ag: 0%	Ag: 22%
Ga: 37%	1.6×10^{19}	1.6×10^{17}
Ga: 60%		1.0×10^{17}

Fig. 5.8. Baseline drive level densities of silver alloys of CIGS cells with higher and lower levels of gallium

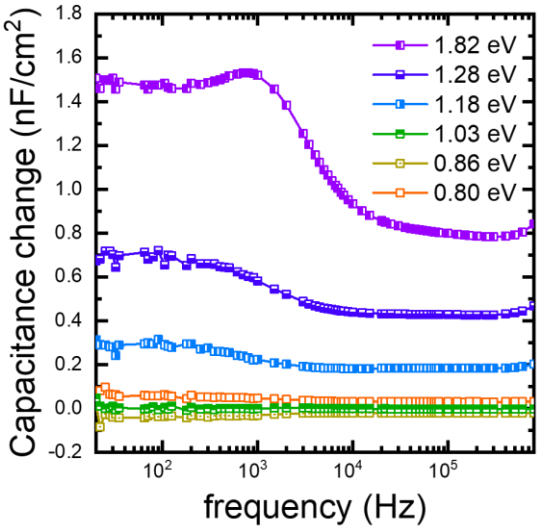

(a)

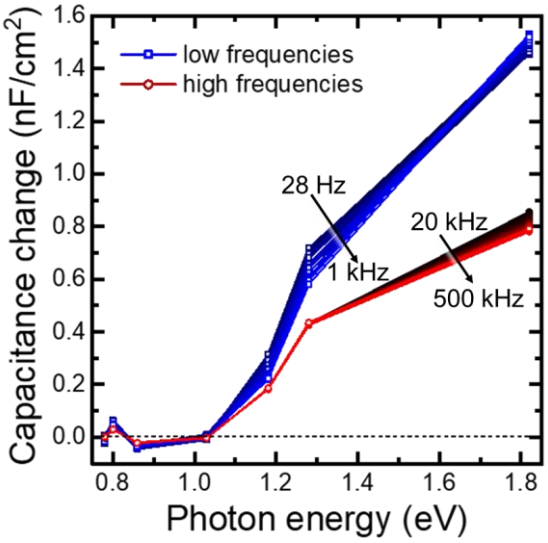

(b)

Fig. 5.9 (a) Change in the dark capacitance of the annealed $(Ag_{0.24}Cu_{0.76})(In_{0.63}Ga_{0.37})Se_2$ device due to exposure to photons of different energies as a function of capacitance measurement frequency. (b) The capacitance increases much more at lower frequencies than at higher frequencies after exposure to above-bandgap energy photons.

The change in capacitance – the difference between capacitance post annealing and post light exposure – is plotted in Fig. 5.9(a). It is observed that there is no significant change in the capacitance profile after exposure to sub-bandgap light. Photons with energy above the bandgap showed significant increase in the capacitance profile. The increase in the capacitance is much greater at lower frequencies than at higher frequencies. The change in capacitance with photon energies measured at high and low frequencies is plotted in Fig. 5.9(b).

5.3.3. Discussion and Conclusions

Experimental and modeling studies on various alloys of CIGS in the literature [14, 15, 16] indicate that the defect step observed below 200K corresponds to bulk defects. Not surprisingly, the presence of bulk defects was observed in all alloys. Observation of a step indicates the presence of defects which can charge and discharge at lower frequencies, but for which the response time of the defect is too slow to charge and discharge at higher frequencies. Measuring the drive level density at low and high frequencies can therefore be used to isolate the free carrier concentration and the defect density. This study confirms that addition of silver reduces the drive level defect density by over two orders of magnitude in CIGS solar cells.

While there is little change in capacitance observed after exposure to sub-bandgap photons, a pronounced increase in capacitance is observed after exposure to photons with energy higher than the bandgap. The rise in capacitance can be reversed by annealing the sample at 320K for 2-3 hours. The step in the capacitance vs. frequency plot is attributed to the defect states in the sample – the larger change in capacitance at lower frequencies than higher frequencies indicate an increase in defect states that cannot charge and discharge at higher frequencies.

The change in capacitance and associated defect density occurs only when the narrow range of photon energies used to illuminate the sample contains a substantial portion of photons above the bandgap energy. Since electron-hole pairs are generated for photon energies above the bandgap, it is possible that the energy from electron-hole recombination is involved in defect formation, in addition to, or instead of, direct absorption of the photon to create the defect. This measurement thus deconvolutes the earlier observation of white-light-induced defect creation by the AM1.5G spectrum in CIGS-based solar cells, showing that photons with energies above the cell absorber bandgap appear to be responsible for the observed defect creation.

In addition to the analysis carried out on the capacitance-frequency measurements in this work, further analysis could be carried on the same measured data. One notable analysis method involves the dielectric loss tangent. The dielectric loss tangent of a material quantifies electrical losses due to various physical processes like electric conduction, dielectric relaxation and any other non-linear processes. Theory reviewed by Gurevich and Tagantsev [59] summarizes the dependence of intrinsic dielectric losses on the crystal symmetry, ac field frequency and temperature. The calculations set a lower limit of losses in defect-free single crystals or pure ideal materials. Any deviation could then be attributed to imperfections in the crystal lattice like grain boundaries, porosity, vacancies, dopant atoms, etc. Amongst other ways, this method could be used to develop further understanding of the nature of defects in the studied material systems.

5.4. Conclusion

This chapter explored the bulk and grain boundary properties in polycrystalline compound semiconductors. These material systems were particularly of interest because they have demonstrated solar cells with high conversion efficiency. Even though these

material systems have high density of defects – some of which could act as recombination centers – the structure, and atomic composition around the defects seem to restrict their interaction with the minority charge carriers.

In the study of surface potential near the grain core and the grain boundaries of CdTe material system, chlorine is reported to diffuse through the grain boundaries. There are many theories to explain the passivation of CdTe grain boundaries after $CdCl_2$ annealing treatment. All of them seem to suggest that presence of chlorine near the grain boundary region reduce recombination rate and improve current collection in a solar cell device. The work presented here suggests that there is a creating of some form a barrier near the grain boundaries at the temperatures known to be most effective for grain boundary passivation.

The work on indium phosphide focused on measurement of conductivity and surface potential near the grain boundaries. The measured contact potential difference though of the right polarity may have been partially shielded due to formation of surface oxide. Nonetheless, this study does suggest that band-bending at InP may shield minority charge carriers from interacting with the dangling bonds and therefore demonstrate good device performance.

The final study was on evolution of defects in silver alloys of CIGS solar cell. While formation of light induced defects in this material system was known, this study studied the wavelength range of photons that created these light induced defects. The origin of defect creation is suggested to be from electron-hole recombination that are formed on absorption photons above the bandgap of the studied material, in addition to, or instead of, the direct absorption of the photon to create the defect.

CHAPTER 6

STRUCTURAL AND ELECTRO-OPTICAL PROPERTIES OF POLYCRYSTALLINE GAINP[*]

6.1. Introduction

In this chapter, we investigate polycrystalline GaInP as a potential top-cell absorber material. Polycrystalline GaInP does not require precise lattice matching or epitaxial growth equipment, and it can be grown monolithically on a silicon bottom cell to form tandem solar cells. However, little information is available in the literature on the growth of polycrystalline GaInP with a 1.6-1.8 eV bandgap [60], or on post-deposition treatment to passivate grain boundaries and interfaces in polycrystalline GaInP through the formation of wider bandgap regions. Suppressing interface recombination at the grain boundaries and at the film surface are key requirements needed to achieve minority-carrier lifetimes consistent with efficient solar cell operation. Here we report on the structural and recombination properties of polycrystalline GaInP over a range of compositions, bandgaps, and growth temperatures.

---

[*]Parts of this chapter have been published as

A. Chikhalkar, A. Gangopadhyay, H. Liu, C. Zhang, F. A. Ponce, D. J. Smith, C. Honsberg, and R. R. King, "Investigation of polycrystalline $Ga_xIn_{1-x}P$ for potential use as a solar cell absorber with tunable bandgap," Journal of Applied Physics 127, 7 (2020).

6.2. Experimental details

GaInP thin films with thicknesses of 0.8-1.0 μm were prepared by co-evaporation of Ga, In and P on thermally-grown (amorphous) SiO_2 films on crystalline Si substrates. Two sets of films were grown at substrate temperatures of 360°C and 435°C, at growth rates of 1 μm/hour in a Veeco Gen III MBE system. Growth without lattice matching at a high deposition rate results in polycrystalline films. Although co-evaporation in an MBE system as implemented here is not a low-cost growth method, we used this approach to accurately control composition and other growth conditions for polycrystalline films that could be deposited by lower cost methods. In contrast, the eventual growth process in a manufacturing environment is envisioned to use a large-area growth chamber with low capital cost, and growth rates of 1 to 2 orders of magnitude higher than the 1 μm/hr used here. Polycrystalline GaInP films were grown with Ga/(Ga + In) composition ratios of 0, 0.05, 0.1, 0.15, 0.25, 0.37 and 0.5, without intentional doping. A ratio of 0.37 is expected to correspond to the desired 1.7-eV bandgap for a GaInP top cell in tandem with a silicon bottom cell.

The as-grown samples were structurally characterized by X-ray diffraction (XRD) using a PANalytical X-pert Pro MRD high-resolution X-ray diffractometer with a Cu-Kα X-ray source operating at 45 kV and 40 mA. The XRD data were background-corrected using spline curves and treated with the Rachinger correction [61] to remove contributions from Cu $K\alpha_2$ X-rays. The morphology of the films was studied using a Philips XL30 environmental scanning electron microscope equipped with a field emission gun, operated at an accelerating voltage of 10-20 kV with electron beam current of 10 pA.

Some of the $Ga_{0.37}In_{0.63}P$ films were coated with a 50-nm Al layer using DC sputtering, in preparation for aluminum-assisted post-deposition treatment. Films with and without

the Al layer were annealed for 10 minutes at 750°C, 800°C or 850°C in inert nitrogen atmosphere using an AST Model 280 rapid thermal processing (RTP) system. To avoid out-diffusion of phosphorus from the GaInP films without an Al cap, a 1-micron GaP film deposited on a Si wafer was placed on top of the samples during the RTP treatment, creating an overpressure of phosphorus. After post-deposition treatment, the excess aluminum was removed by etching in an $HCl:H_2O$ (1:1) solution for 30 seconds. The $HCl:H_2O$ solution selectively etches the Al-rich metal alloy and the Al-rich regions near the top surface of the AlGaInP layer with variable Al composition.

Steady-state photoluminescence (PL) spectroscopy used a green (532 nm) laser as the excitation source with an Andor 750 spectrometer, and the sample temperature was controlled using a cryostat cooled with liquid nitrogen (Linkam Scientific THMS350V). Time-resolved photoluminescence (TRPL) spectroscopy was measured using a time-correlated single-photon counting system (Becker and Hickl). A supercontinuum white light laser source (Fianium, SP450) with 6-ps pulses, was tuned using a diffraction grating and filter to form excitation light, also at 532 nm wavelength. The tool has a 40-ps instrument response. Cross-sectional cathodoluminescence (CL) was measured in spot mode in a scanning electron microscope (SEM) at room temperature, with an electron beam current of 2.0 nA and an accelerating voltage of 7 kV. Two-dimensional (2D) elemental composition maps were acquired using a probe-corrected JEOL ARM-200F scanning transmission electron microscope (STEM) equipped with an energy-dispersive X-ray spectroscopy (EDS) detector. EDS line scans were smoothed using a 10-point adjacent-averaging method. Cross-sectional samples suitable for STEM analysis were prepared by focused-ion-beam milling using a FEI Nova 200 instrument.

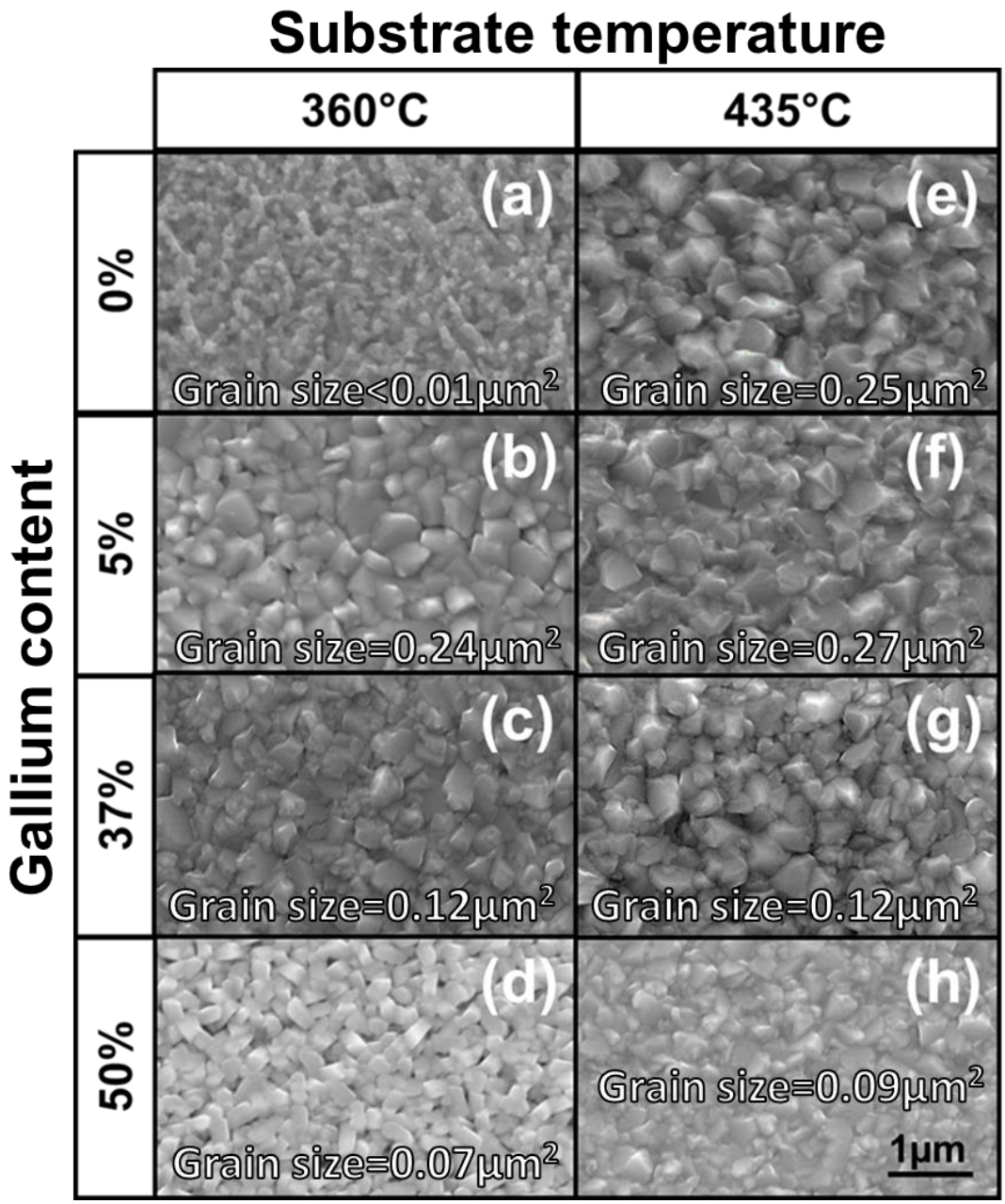

Fig. 6.1 Changes in polycrystalline GaInP morphology with increasing Ga content at growth temperatures of 360°C (a-d) and 435°C (e-h), imaged by scanning electron microscopy.

The morphologies of two sets of $Ga_xIn_{1-x}P$ films grown at 360°C and 435°C, with varying Ga/(Ga + In) composition (x values of 0, 0.05, 0.37 and 0.50) are shown in Fig. 6.1. The images confirm a uniform surface morphology across the 2-inch SiO_2/Si substrate. The average grain size, measured using the line intercept method, increases with increasing growth temperature.

Moreover, the grain size at a fixed growth temperature generally decreases with increasing Ga/ (Ga + In) ratio from 5% to 50% (Fig. 6.1). This decrease may be due to a higher nucleation rate in films with higher Ga content. Since the bond-strength of Ga–P is higher than that of In–P, it is expected that Ga–P is a more energetically favorable reaction product and that Ga surface mobility may be lowered, leading to a greater density of growth nuclei for higher Ga/(Ga + In) ratio, giving higher grain density and therefore smaller grain size [62].

Figure 6.2 shows the evolution of the X-ray diffraction pattern of polycrystalline $Ga_xIn_{1-x}P$ film grown at 435°C, with increasing Ga/(Ga + In) ratio. The indices of the Bragg reflection peaks (*i.e.*, hkl) labeled in black correspond to the $Ga_xIn_{1-x}P$ phase. Assuming that the crystal structure of the polycrystalline $Ga_xIn_{1-x}P$ is zincblende – similar to that of its single crystal counterpart – the reflection peak positions are consistent with those expected for planes (111), (200), (220), (311) and (222). An example of the analysis carried out on the green curve is shown in Table 6.1. The lattice constant extracted from this analysis is used to estimate the Ga content of the film using Vegard's law [11]. Other

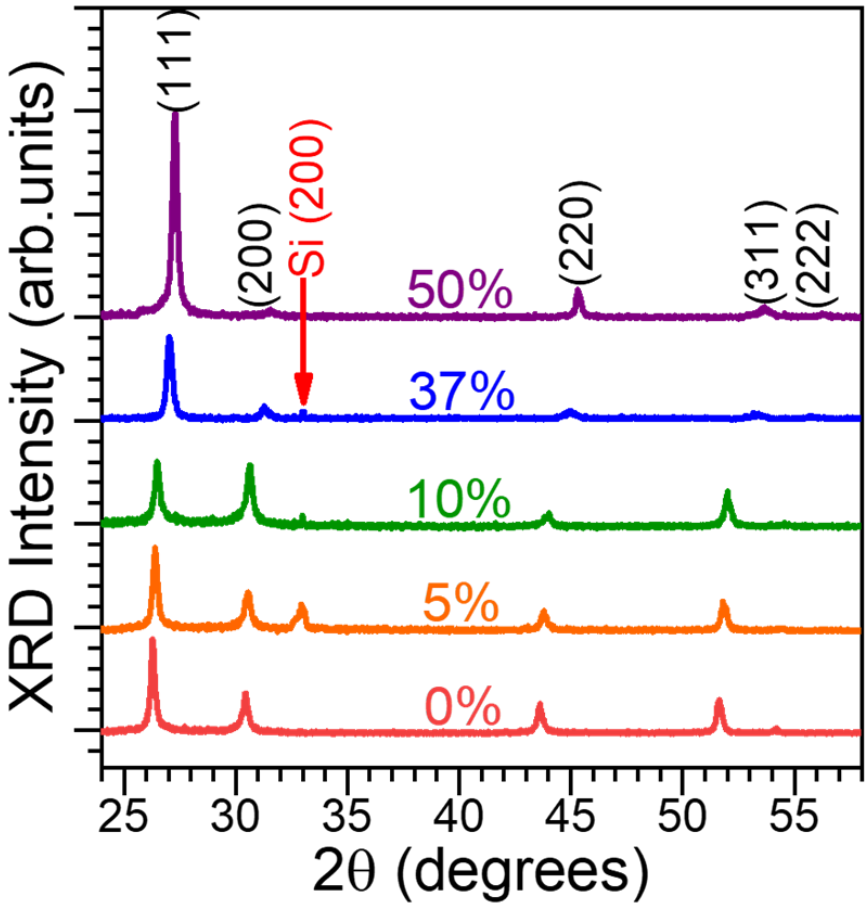

Fig. 6.2 XRD profiles for polycrystalline $Ga_xIn_{1-x}P$ grown at 435°C substrate temperature with varying x = Ga/(Ga + In) ratio. Black indices of the Bragg reflection peaks (*i.e.*, hkl) indicate the $Ga_xIn_{1-x}P$ phase; red hkl indices represent the Si substrate.

Table 6.1. Steps taken to extract the planes responsible for XRD reflection peaks and the lattice constant of the grown compound.

Peak #	2θ (degree)	θ (degree)	$\sin^2\theta$	normalized	integer	plane
1	26.49	13.25	0.053	1.00	3	(111)
2	30.62	15.31	0.070	1.33	4	(200)
3	43.95	21.98	0.140	2.67	8	(220)
4	52.00	26.00	0.192	3.66	11	(311)
5	54.56	27.28	0.210	4.00	12	(222)
6	63.82	31.91	0.279	5.32	16	(400)

factors like strain and substitutional defects may introduce a small uncertainty, for instance, resulting in the negative Ga/(Ga + In) ratio extracted for InP. The full-width at half-maximum (FWHM) of the peaks remains less than 0.4° for compositions of x = 0.37 and lower, suggesting a relatively low density of bulk defects [63].

The XRD reflection positions align well with the allowed planes for FCC Bravais lattice. Lattice constant is extracted using Braggs equation:

$$\lambda = 2\frac{a}{\sqrt{h^2+k^2+l^2}}\sin\theta$$

$$a = \frac{\lambda\cdot\sqrt{h^2+k^2+l^2}}{2\sin\theta} \tag{6.1}$$

Average of the lattice constant extracted for each of the peaks is used to estimate the gallium content of the film.

Figure 6.3 shows the evolution of the (200) XRD peak with Ga composition. The XRD peak position shifts to higher angles as the lattice constant decreases with increase in

gallium content. No new peaks appear with increased Ga content, indicating that a miscible GaInP alloy is formed without phase separation. The Ga beam flux ratio, lattice constant measured from the (311) XRD peak positions, Ga/(Ga + In) ratio and measured

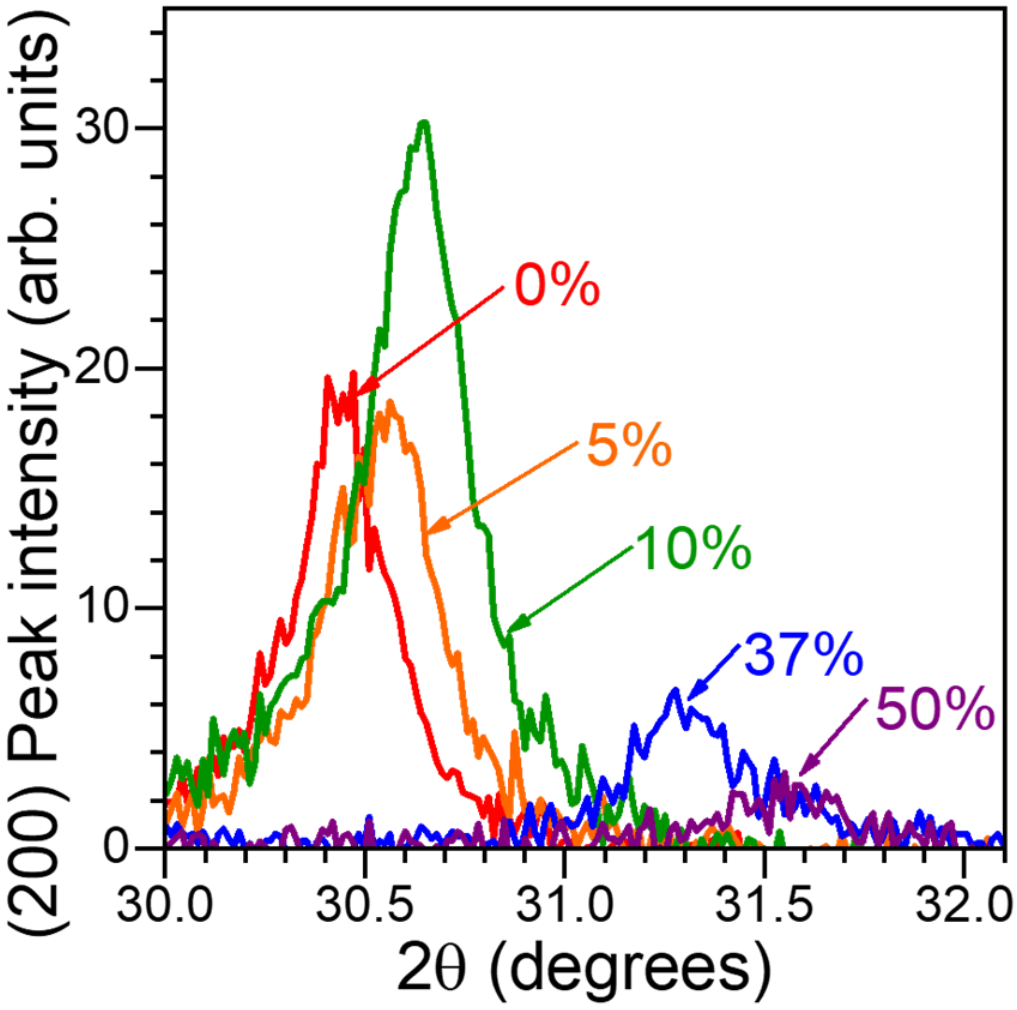

Fig. 6.3 Evolution in polycrystalline X-ray diffraction with increasing Ga content.

grain size are summarized in Table 6.2.

Table 6.2. Summary of structural and photoluminescence characteristics of polycrystalline $Ga_xIn_{1-x}P$ thin films grown at a substrate temperature of 435°C with varying composition. The Ga beam flux ratios are based on calibrations with single-crystal GaInP. The calculated ga content is the [Ga]/([Ga]+[In]) ratio consistent with single-crystal GaInP with the lattice constant a_o that was measured on the polycrystalline GaInP films.

Target $\frac{[Ga]}{[Ga]+[In]}$ **(%)**	**Beam flux** $\frac{p_{Ga}}{p_{Ga}+p_{In}}$ **(%)**	**Lattice constant** a_o **(Å)**	**Calculated** $\frac{[Ga]}{[Ga]+[In]}$ **using meas.** a_o **(%)**	**Grain size (nm)**
0	0.00	5.869	-0.08	374
5.7	3.43	5.846	5.45	386
15	9.67	5.803	15.61	365
25	16.37	5.764	25.09	340
37	26.27	5.694	41.77	289

The PL spectrum of single-crystal InP is compared to as-grown polycrystalline InP in Fig. 6.4. Both single-crystal and polycrystalline PL spectra were fitted with bi-gaussian curves. The inflection point in the PL spectrum, indicative of the bandgap, is also extracted as shown in Fig. 6.4. The extracted bandgap is observed to be very similar for the single-crystal and polycrystalline cases.

The PL spectra of as-grown polycrystalline $Ga_xIn_{1-x}P$ measured at room temperature for a range of Ga compositions are shown in Fig. 6.5. These PL spectra can have two

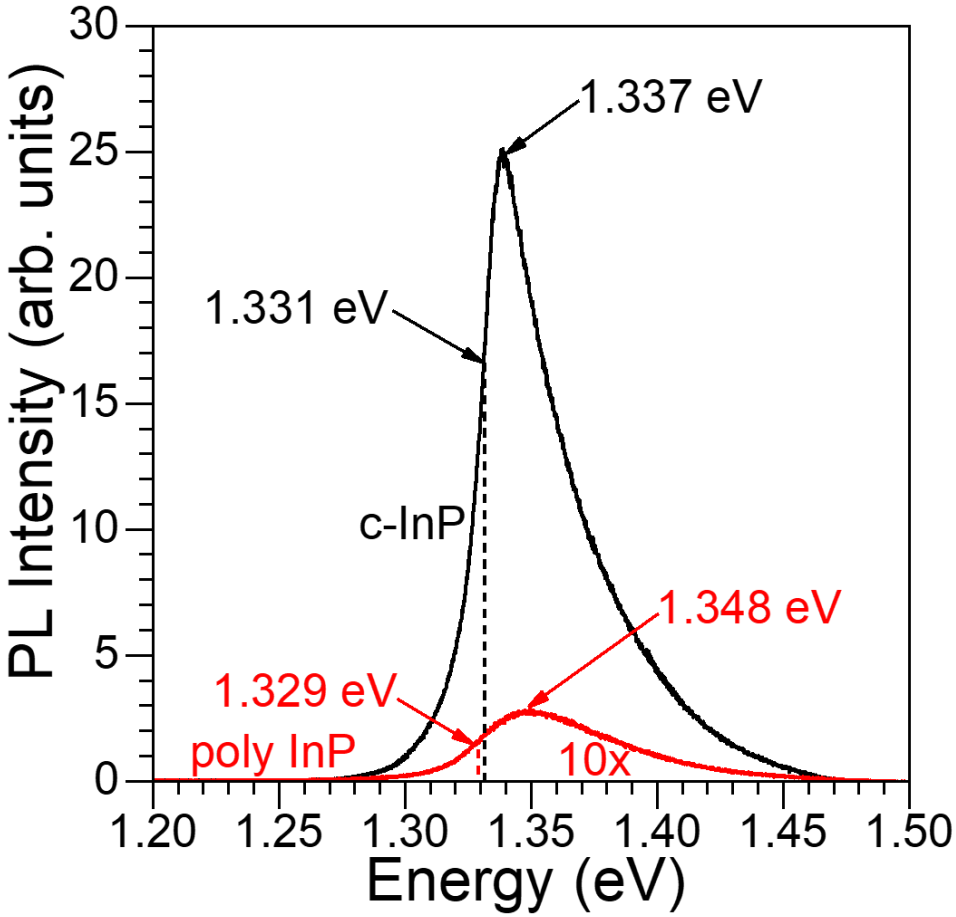

Fig. 6.4 Photoluminescence spectra of non-passivated single crystalline InP wafer and as-grown 1-micron polycrystalline InP. The PL peak positions and the inflection points – indicative of the bandgap of the material – are also highlighted.

overlapping peaks for the higher Ga composition films and were deconvoluted into a low-energy bi-gaussian curve 1, and a high-energy bi-gaussian curve 2. Experimental E_g values were extracted from the inflection point (where $d^2(PL)/dE^2 = 0$) on the low energy side of both the low-energy and high-energy curves, at each Ga composition. These experimental E_g values are plotted in Fig. 6.6, together with calculated curves for the bandgap of single-crystal GaInP with group-III sublattice ordering, and with full group-III sublattice disordering, for comparison. The bandgaps extracted from the low-energy PL curve 1 for

each Ga composition appear to correspond roughly to the calculated ordered GaInP bandgaps, and those extracted from the high-energy PL curve 2 correspond approximately to disordered GaInP calculations, suggesting a bimodal distribution of ordered and disordered regions in the polycrystalline GaInP films. However, it cannot yet be ruled out that one of the PL peaks at each Ga composition could be due to constructive interference at a particular wavelength, caused by the specific thicknesses of the layers in the structure.

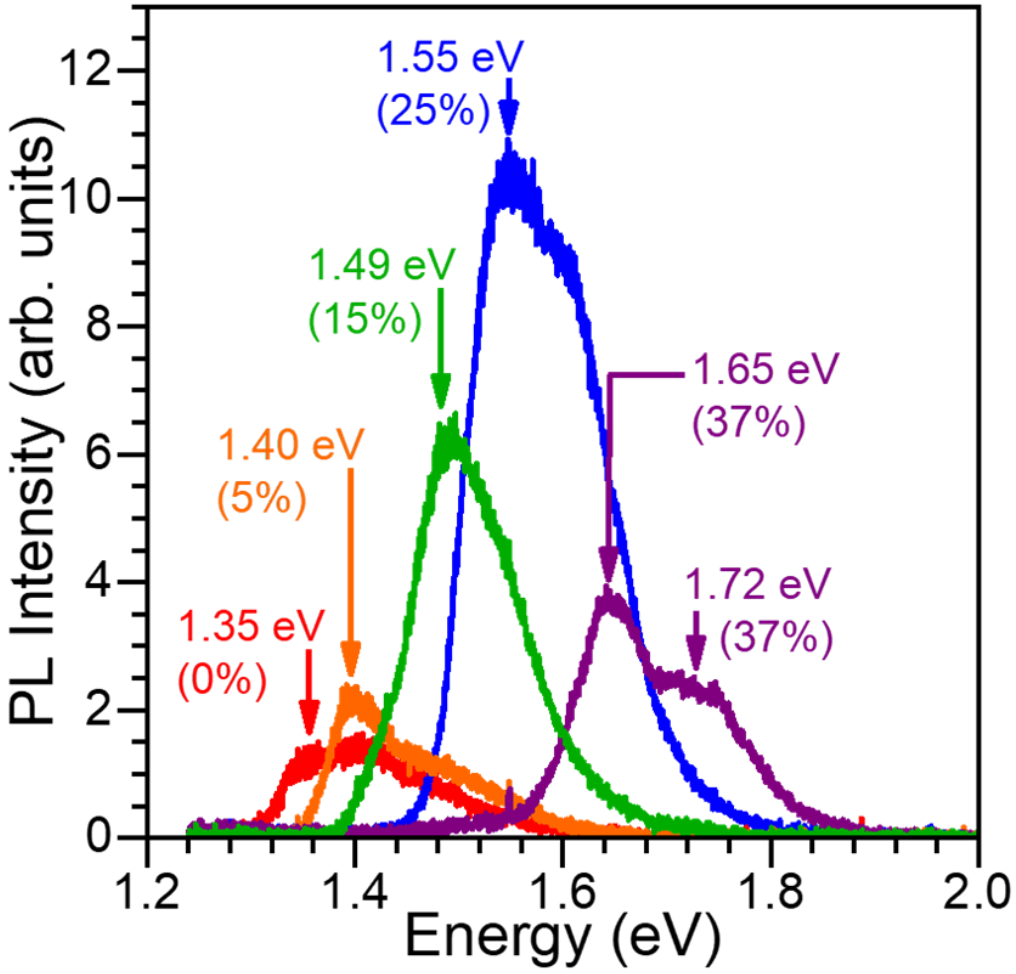

Fig. 6.5 Evolution of polycrystalline GaInP photoluminescence spectrum with change in Ga composition.

The Ga compositions of experimental samples plotted in Fig. 6.6 are determined from the XRD measurements. The bandgap extracted from the high-energy PL curve 1 for

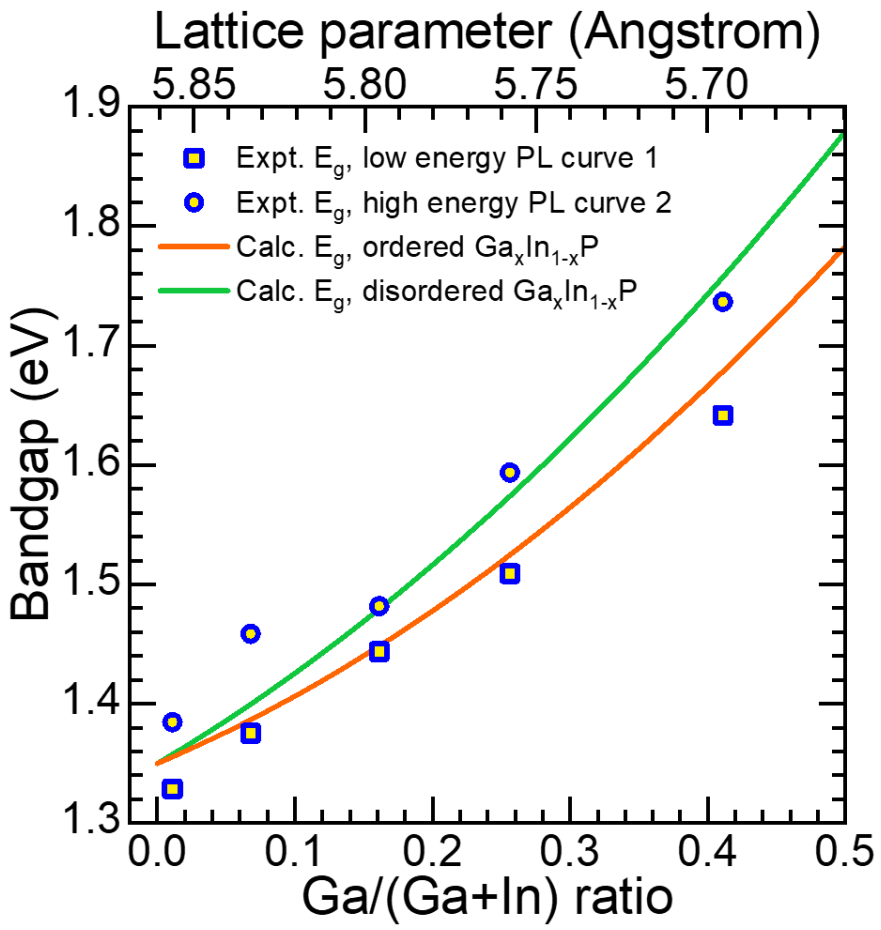

Fig. 6.6. Experimental bandgap E_g values for polycrystalline GaInP with varying Ga composition, extracted from photoluminescence measurements at room temperature. The PL spectrum at each Ga composition was deconvoluted into a low-energy bi-gaussian curve 1, and a high-energy bi-gaussian curve 2. The E_g values were extracted from the inflection point (where $d^2(PL)/dE^2 = 0$) on the low energy side of both the low-energy and high-energy curves, at each Ga composition. Calculated curves for the bandgap of single-crystal GaInP with group-III sublattice ordering, and with full group-III sublattice disordering, are shown for comparison. The Ga composition was determined from XRD measurements on the films.

px-GaInP film with x = 0.37 is 1.72 eV, close to the theoretical optimum top-cell bandgap of ~1.7-eV for a Si-based tandem solar cell. Summary of the variation in material properties with change in Ga content of the GaInP thin films is shown in Fig. 6.7. The integrated intensity under the PL spectrum increases with rising Ga mole fraction x from 0.0 to 0.25. For x = 0.37, the integrated intensity drops sharply and for x = 0.50 it is not detectable at room temperature. Thus, the increase in PL intensity from pure InP to low-Ga mole fraction GaInP, at least up to 25% Ga, and the subsequent decline in PL intensity from 25% to 37% Ga composition, occurs in polycrystalline $Ga_xIn_{1-x}P$ (this work), as well as in $Ga_xIn_{1-x}P$ nanowires [64,65]. The decrease in quantum yield in nanowires at higher Ga content has been attributed to faster trapping of electrons and holes, as well as more rapid non-radiative recombination at higher Ga content [64]. It is not yet known whether this phenomenon is caused by a similar mechanism in the largely wurtzite GaInP nanowires and the predominantly zincblende polycrystalline GaInP. It is also not yet clear how the defect energies and capture cross sections evolve with increasing Ga composition and bandgap, or indeed whether the defect states primarily responsible for the change in PL with composition reside in the bulk semiconductor region of the nanowires and px-GaInP grains, or at the nanowire surfaces and px-GaInP grain boundaries. However, the observations reported in this study that the Al PDT surface treatment can reduce non-radiative recombination rate by 720-fold, as described in the next section, indicates the surface is a dominant region for recombination in unannealed px-GaInP.

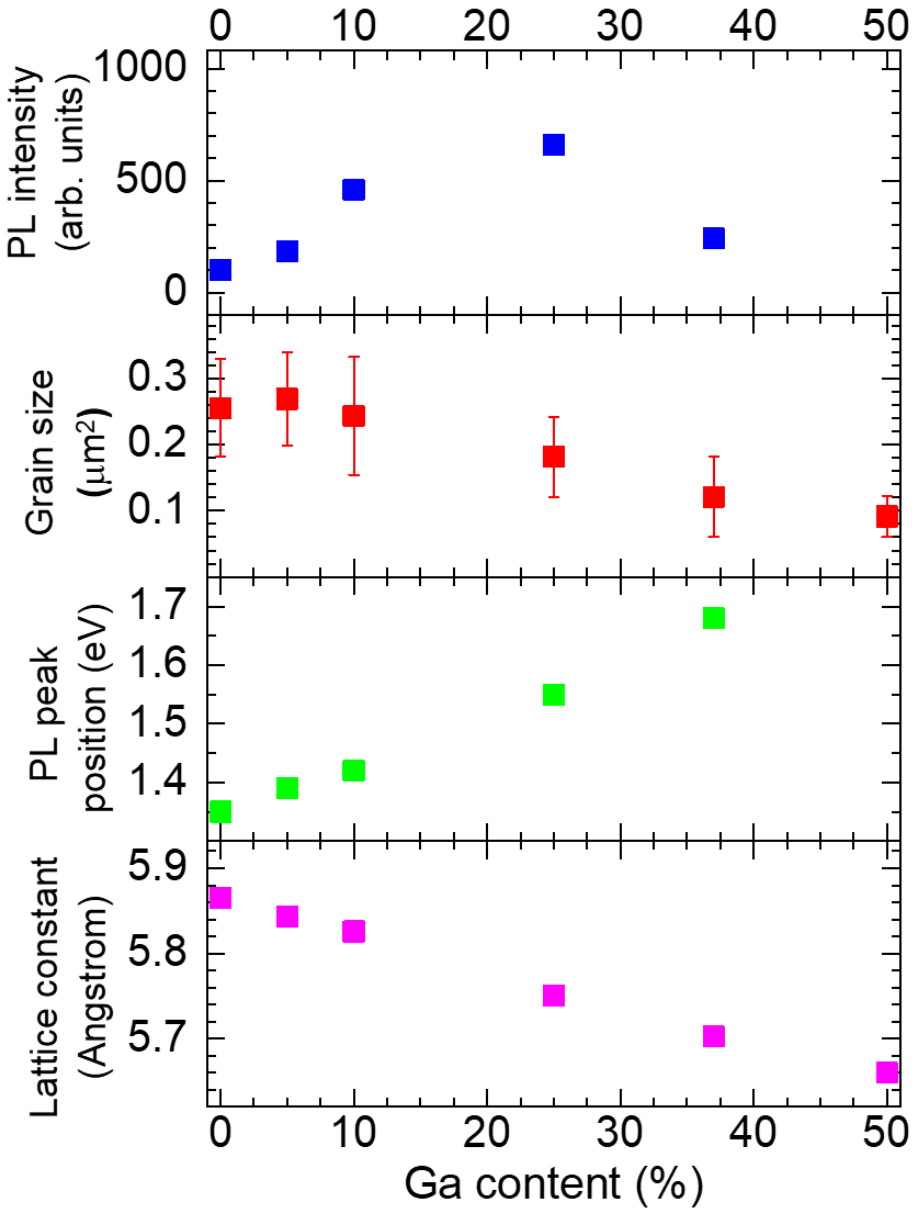

Fig. 6.7. Summary of the variation in material properties with change in Ga content of the GaInP thin films. The growth temperature is 435°C. Lattice constant is extracted from XRD reflections. PL peak position and integrated PL intensity is measured using Raman spectrophotometer at room temperature and grain size is extracted from the scanning electron microscopy images.

6.4. Passivation treatments

6.4.1. Annealing treatments

Post-deposition treatments can be remarkably effective at reducing minority-carrier recombination in polycrystalline semiconductors. Here we use the term post-deposition treatment (PDT) to refer to thermal or plasma treatment of a semiconductor layer after it has been formed rather than during growth, often in the presence of another chemical species that reacts with the semiconductor. PDTs can achieve their passivating effect on recombination by: 1) tying up dangling bonds to lower mid-gap interface state density; 2) reducing the density or activity of bulk defects in the grain core; 3) increasing grain size to reduce the grain boundary area per unit volume; and 4) creating a new material phase at the grain boundaries and surfaces with higher bandgap or doping, which induces band bending at these interfaces. For example, the $CdCl_2$ post-deposition treatment in II-VI semiconductors [66] is essential to form high quality solar cells from polycrystalline CdTe, and seems to have beneficial effects through a combination of mechanisms 2, 3, and 4. Post-deposition treatment of polycrystalline silicon can cause dopants and other atomic species to segregate at grain boundaries (mechanisms 1 and 4), and can cause passivation, gettering, and dissolution of defects in the grain core (mechanism 2), improving solar cell voltage and current collection [67-70]. Post-deposition treatment with aluminum has been studied to increase grain size in polycrystalline Si [71] and Ge [72] solar cells (mechanism 3). Non-epitaxial, post-deposition sulfide treatments [73-75] have been successful in reducing interface state density and recombination at GaAs surfaces. Aluminum contacts on GaAs and InP, formed at low temperature (< 365°C) such that little Al diffusion or alloying takes place, and metal and semiconductor phases remain largely distinct, can alter the surface states which induce band bending at the interface, affecting barrier heights and carrier recombination at the contact [76].

To improve the minority-carrier properties of 1.7-eV GaInP films, post-deposition treatments with and without a surface aluminum layer are explored. A cross-sectional transmission electron microscopy (TEM) image and schematic diagram of polycrystalline GaInP after annealing with an Al surface layer are shown in Fig. 6.8.

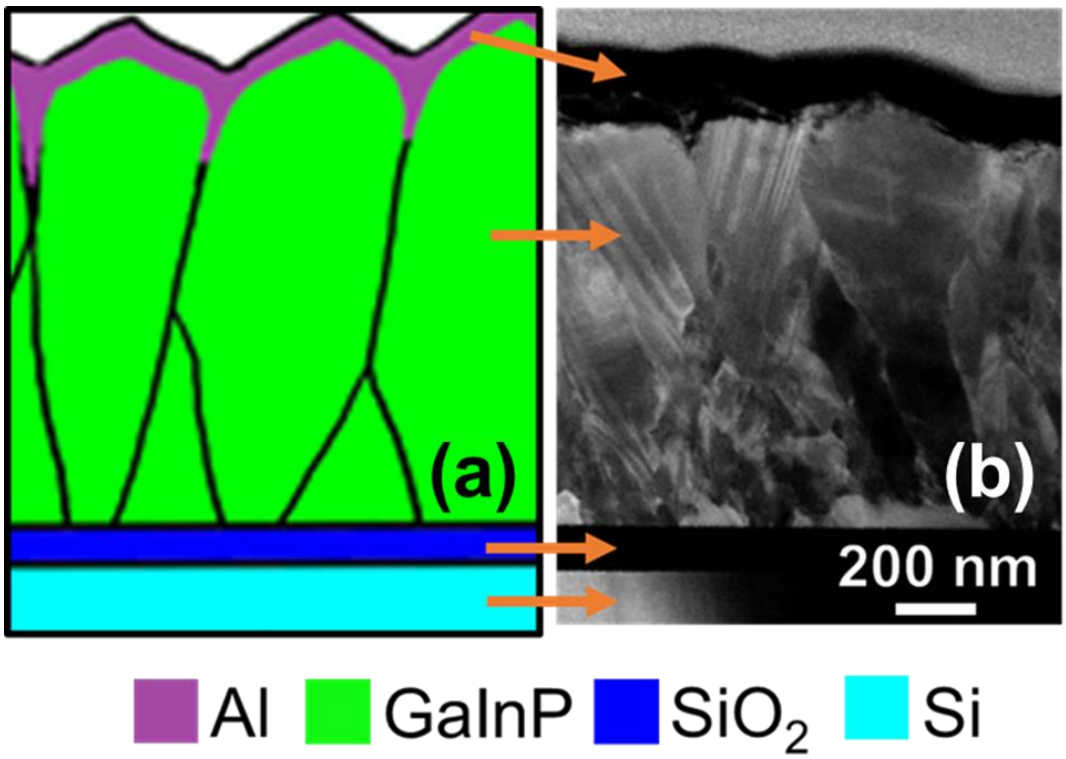

Fig. 6.8. Experimental (a) Schematic diagram and (b) cross-sectional TEM image of polycrystalline GaInP after Al-assisted post-deposition treatment.

The measured PL spectra for polycrystalline GaInP films annealed for 10 minutes with and without aluminum are shown in Fig. 6.9, for 532-nm laser excitation intensity of 4718 W/cm^2. For control samples without Al, the peak PL intensity for a 750°C anneal was approximately 0.7× that of the as-grown case, and was 1.5× higher for an 800°C anneal.

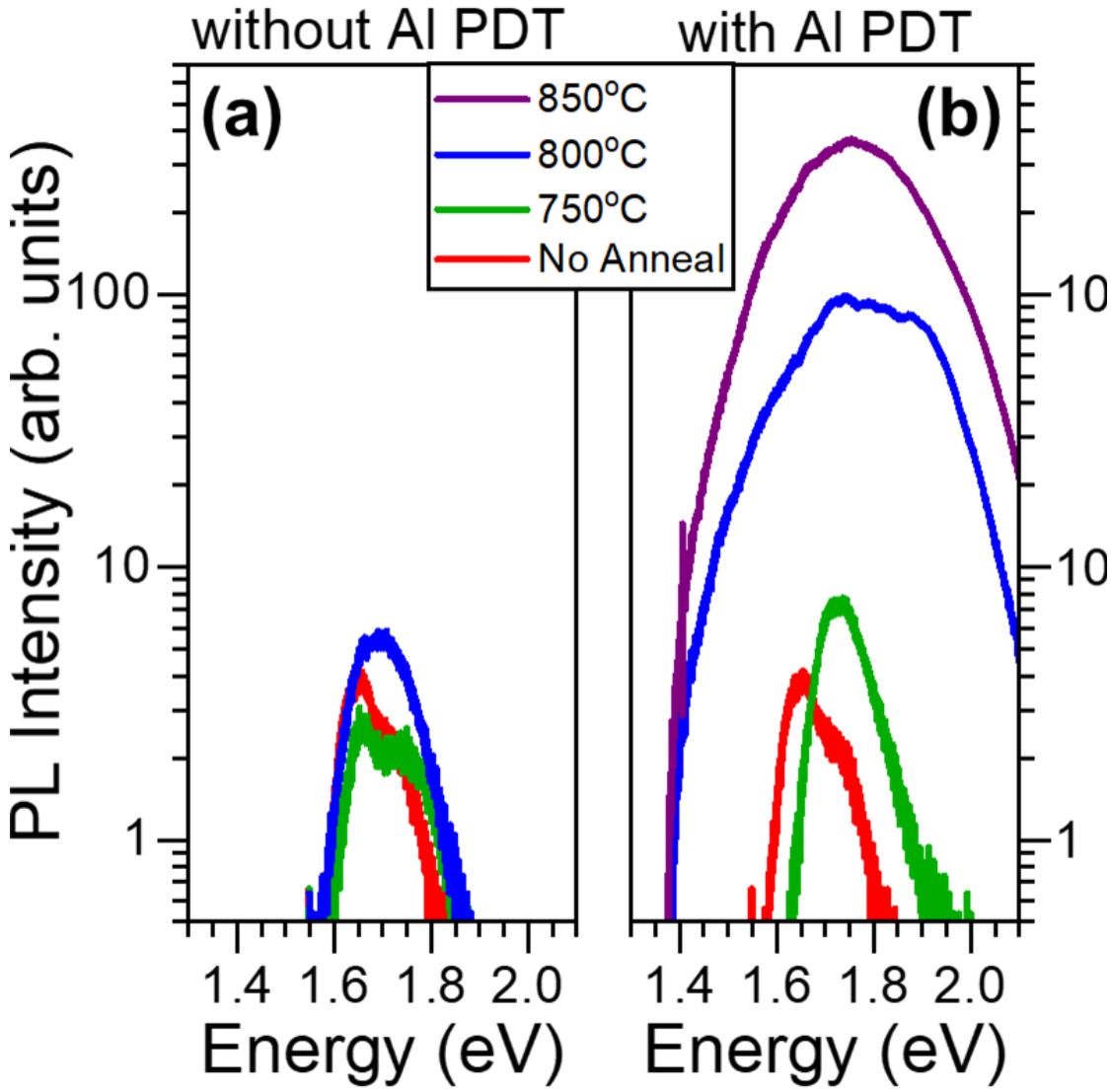

Fig. 6.9. PL spectrum evolution of $Ga_{0.37}In_{0.63}P$ thin films (a) without and (b) with Al-assisted post-deposition treatment (PDT). The peak intensity after Al PDT at 850°C is approximately 90 times higher than for as-grown samples. Without an Al cap, samples decomposed when annealed at 850°C and the PL could not be measured.

The films without an Al cap layer decomposed at 850°C, forming metallic droplets on the surface, and no PL could be detected. In contrast, polycrystalline GaInP after post-deposition treatment with an aluminum cap layer, was stable when annealed at 850°C. As shown in Fig. 6.9 the peak PL signal of the sample annealed at 850°C in the presence of Al increased by 250-fold, and the integrated area under the PL peak increased by up to 720-fold with respect to the non-annealed case.

The integrated area under the PL spectrum is proportional to the total photon flux from radiative recombination in the bulk GaInP grain core and is thus the preferred figure of merit rather than simple peak height for comparing recombination activity in the samples with and without Al-PDT. An increase in integrated PL intensity from semiconductor samples is typically indicative of an increase in radiative recombination rate $R_{rad} = Bpn$, where B is the radiative recombination coefficient, and p and n are the hole and electron concentrations, respectively. Provided that the polycrystalline GaInP behaves similarly in this way to single-crystal GaInP, the increase in integrated PL intensity after Al-PDT indicates an increase in quasi-Fermi level splitting, and potentially in the solar cell voltage that could be achieved.

6.4.2. Formation of higher-bandgap AlGaInP region

In the leading hypothesized mechanism for the observed 90× increase in peak PL intensity with Al-assisted post-deposition treatment, aluminum can form a graded AlGaInP quaternary phase at elevated temperatures on the GaInP front surface, creating a graded wide-bandgap layer, and passivating the front surface of the 1.7-eV GaInP. Further, aluminum is a small atom, which is expected to have greater diffusivity along grain boundaries than through grain cores [77]. Preferential Al diffusion along grain boundaries would form a wide-bandgap AlGaInP phase passivating the GaInP grain

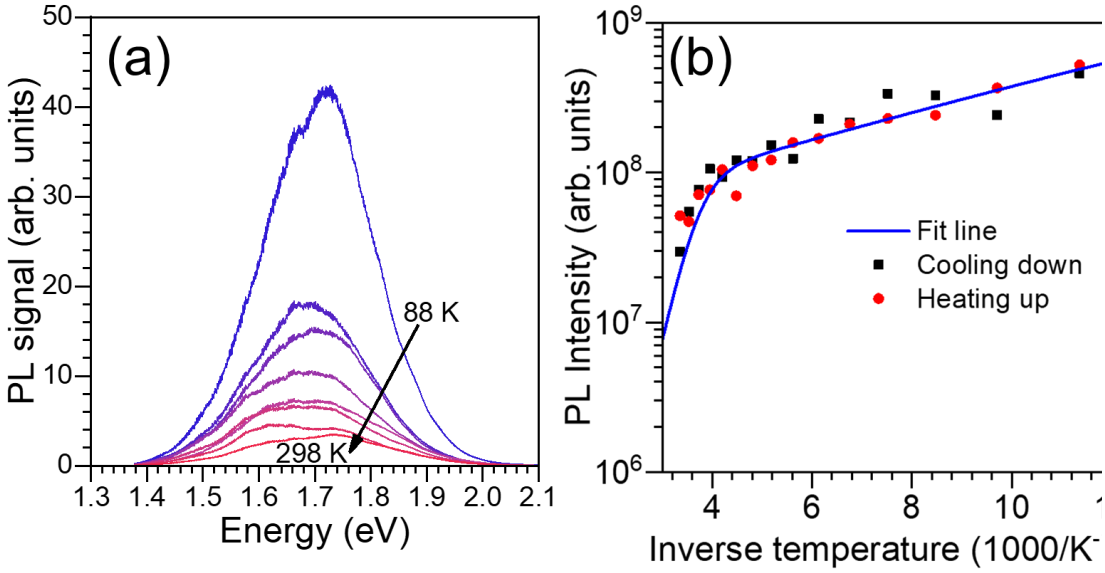

Fig. 6.10. (a) PL spectra of polycrystalline $Ga_{0.37}In_{0.63}P$ after aluminum-assisted annealing at 850°C for 10 min., measured at temperatures from 88 K to 298 K, (b) Plot of change in integrated PL intensity against inverse of temperature to extract energy of activation.

boundaries near the surface as well as at the surface itself. Measurements consistent with this hypothesis are outlined below.

The intensity of the PL spectrum of polycrystalline GaInP after post-deposition treatment with Al, increases as the temperature during measurement is decreased from room temperature to 78 K, as shown in Fig. 6.10.

$$I = \frac{I_0}{1 + C_1\, exp(-E_1/k\,T) + C_2\, exp(-E_2/k\,T)} \qquad (6.2)$$

The plot of integrated PL intensity against inverse of temperature follows a trend that is consistent with trap-assisted form of recombination that has two defect activation energies. Change in PL intensity with temperature that includes such a form of

recombination is given by Equation (6.2) Slopes close to room temperature and 78K are used to estimate the activation energies of 19 meV and 300 meV respectively.

The PL signal at 78K was strong enough to measure time-resolved photoluminescence (TRPL) decay of polycrystalline GaInP after Al-PDT as shown in. The TRPL decay curves, which indicate decay of minority-carrier concentration as the photoexcited carriers recombine, typically have a rapid exponential decay constant (short lifetime τ_1) just after

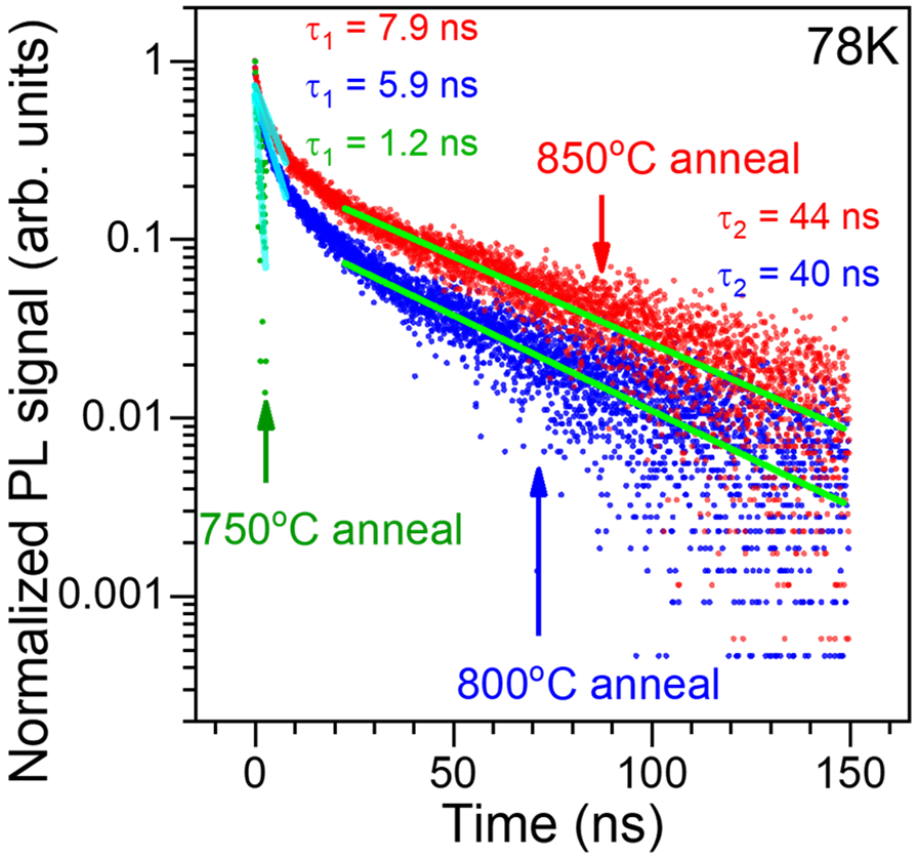

Fig. 6.11. Time-resolved photoluminescence decay (TRPL) of polycrystalline $Ga_{0.37}In_{0.63}P$, measured at 78 K, after aluminum-assisted annealing at various temperatures for 10 minutes. The TRPL decay curves are resolved into a short lifetime τ_1 near the beginning of the decay curve, and a longer lifetime τ_2 at later times in the decay. Lifetimes of up to 44 ns were observed in undoped polycrystalline GaInP films.

the excitation light pulse is switched off, and a slower decay constant (longer lifetime τ_2) for the remainder of the decay. In epitaxial films, the shorter lifetime toward the beginning of the curve is largely controlled by recombination at the front surface where the excitation light pulse is incident, and the longer lifetime at later times in the decay curve are more characteristic of bulk lifetimes in epitaxial films [78]. The longer lifetime τ_2 is thus a key indicator of the bulk quality of the semiconductor film. In these polycrystalline GaInP samples, the short lifetime τ_1 may be controlled by recombination at the front surface upon which the excitation light is incident, and the long lifetime τ_2 characteristic of minority-carrier recombination in the grain bulk, but this has not yet been confirmed in these samples.

For polycrystalline GaInP samples with Al-PDT at 750°C, the TRPL intensity was low, and the lifetimes were very short, approximately 1.2 ns. For px-GaInP with Al-PDT at temperatures of 800 and 850°C, the TRPL signal was much brighter, and lifetimes were longer, indicating slower minority-carrier recombination, and higher quasi-Fermi level splitting that can be sustained at a given illumination level, necessary for high solar cell voltage. For both 800 and 850°C, the short lifetime τ_1 increased to approximately 6-8 ns.

For samples with Al-PDT at 800°C, the longer lifetime τ_2 characteristic of later times in the decay curve increased markedly to ~40 ns, while the τ_2 time constant for polycrystalline GaInP films with Al-PDT at 850°C increased further to ~44 ns, as shown in Fig. 6.11.

Fig. 6.12 shows the CL spectra measured in spot mode on a cleaved cross section of a polycrystalline GaInP film after Al-PDT, in regions near the surface (Spot 1) and in the bulk film farther from the surface (Spot 2). A distinct CL signal at 2.0 eV is observed when

the electron beam is incident near the surface: this region is postulated to be AlGaInP. No such peak was observed from the bulk region, which is expected to be predominantly

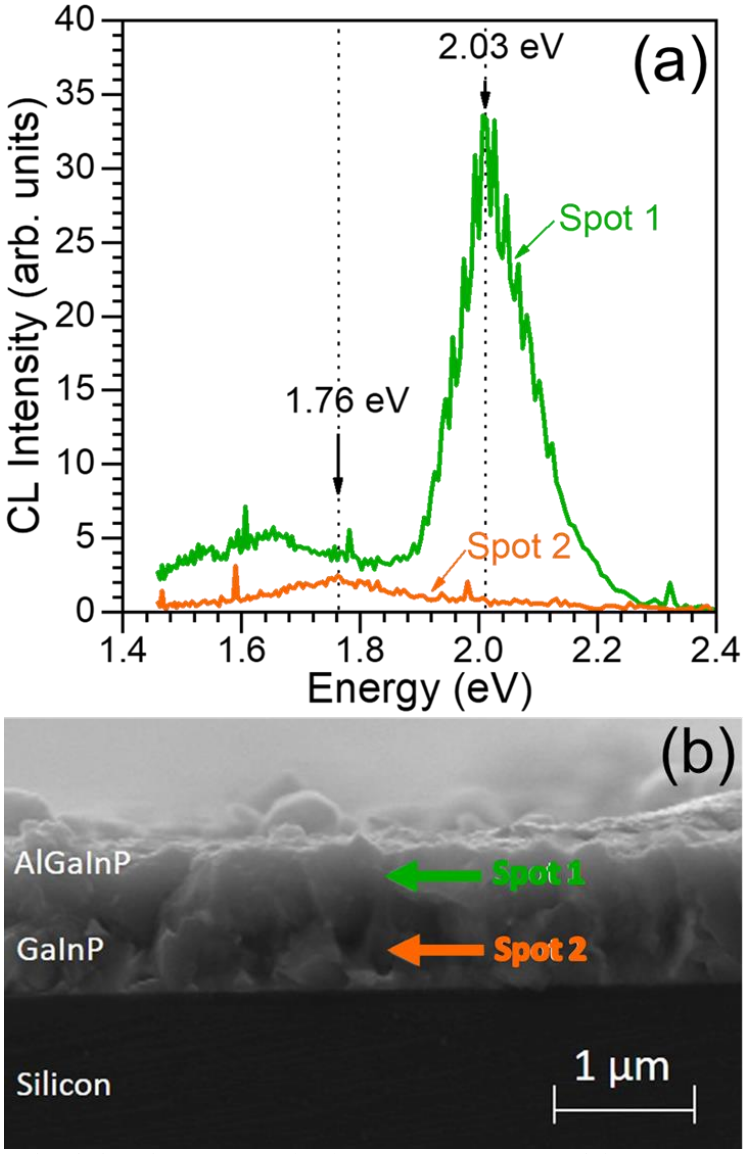

Fig. 6.12. (a) Cathodoluminescence (CL) spectra measured in spot mode on a cross section of a polycrystalline GaInP film after Al-PDT, for regions near the surface (Spot 1) and in the bulk film farther from the surface (Spot 2). (b) Secondary electron image of a different but representative area of the film cross section, indicating approximate distances from the surface of the regions measured by CL.

GaInP. To further investigate the origin of the 2.0-eV signal at the surface, an EDS line

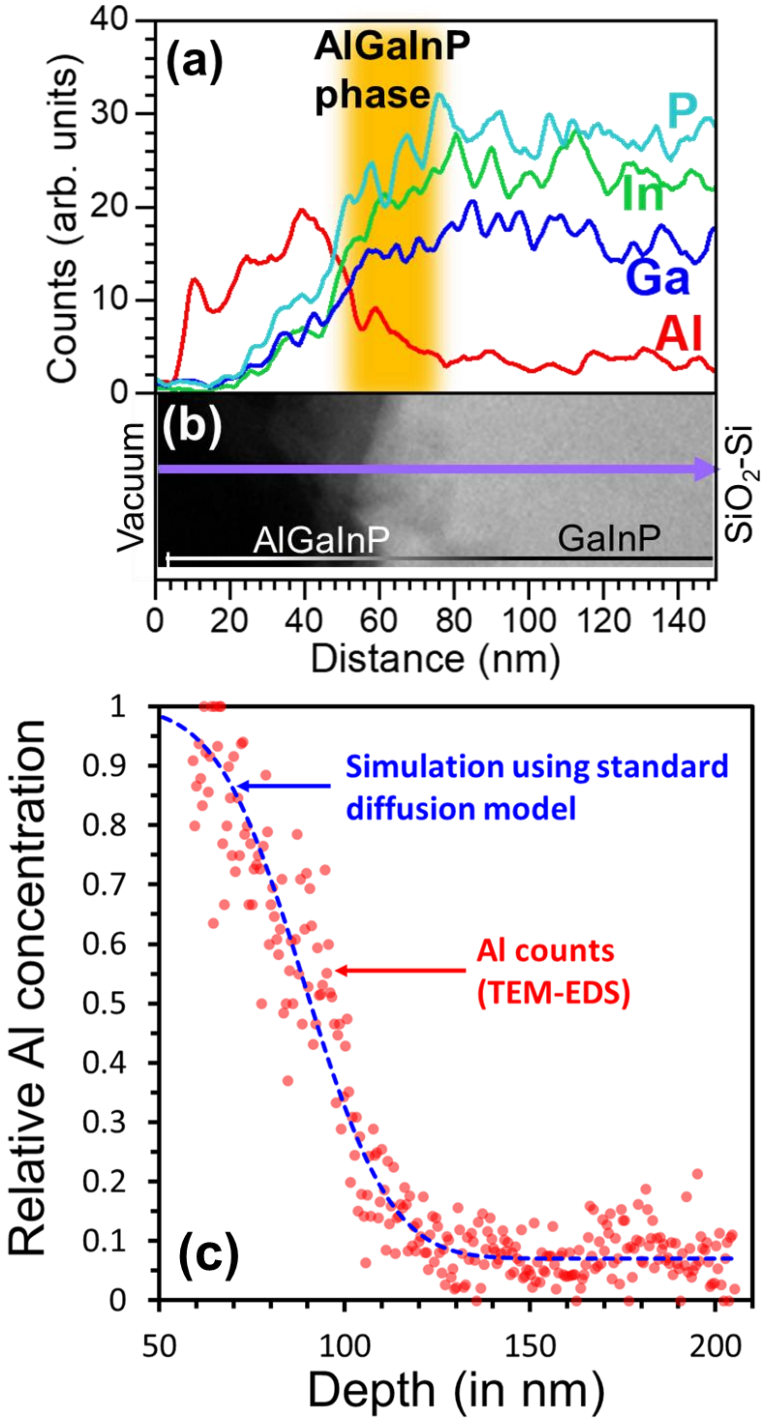

Fig. 6.13. (a) EDS line scan from top surface towards the bottom Si substrate plotting the variation of Al, Ga, In and P concentrations near the top surface of one GaInP grain. (b) TEM image of GaInP highlighting the region along which EDS line scan was measured.

scan of polycrystalline GaInP annealed with Al at 850°C is plotted in Fig. 6.13. This shows high Al concentration near the top surface consistent with alloying followed by crystal regrowth and decreasing Al concentration moving into the GaInP film, consistent with Al diffusion.

$$c(x,t) = c_s[1 - erf\ (\frac{x}{2\sqrt{Dt}})] \tag{6.3}$$

A solution for the Fick's second law of diffusion with a boundary condition of constant flux is given by Equation (6.3). This solution fits well with the EDS counts for aluminum. Assuming that the ratio of Al concentration is proportional to the EDS counts of aluminum, diffusivity of aluminum in GaInP is estimated to be 2.8×10^{-15} $cm^2 sec^{-1}$. This is lower than the rough estimate by Beernink *et al.* [79].

Furthermore, EDS maps of the grain boundary region near the surface, as shown in Fig. 6.14, suggest preferential Al migration along grain boundaries, possibly by diffusion, near the film surface.

The CL and EDS measurements in Fig. 6.12, Fig. 6.13, and Fig. 6.14 are consistent with a compound containing Al, Ga, In, and P at the front film surface, with decreasing composition of Al progressing deeper into the px-GaInP film. One possibility is formation of an AlGaInP/GaInP graded heterostructure at the film surface and at grain boundaries near the top surface, which in single-crystal GaInP would shield minority carriers from the defect states at the front surface.

Metal-organic vapor-phase epitaxy (MOVPE) and molecular beam epitaxy (MBE) studies have shown that AlGaInP can be grown at and near the GaAs lattice constant with continuously variable Al composition, without miscibility gaps, at temperatures below that of the post-deposition treatments used here. However, the uniformity and chemical bonding configuration of the Al-containing compound at the surface of these polycrystalline films after Al-PDT are not presently known. It seems plausible that AlGaInP could form by Al solid-state diffusion into GaInP, or by Ga, In, and P solid-state diffusion into metallic Al followed by regrowth of AlGaInP when the temperature decreases and the solid solubility of these elements in Al is reduced. However, we have

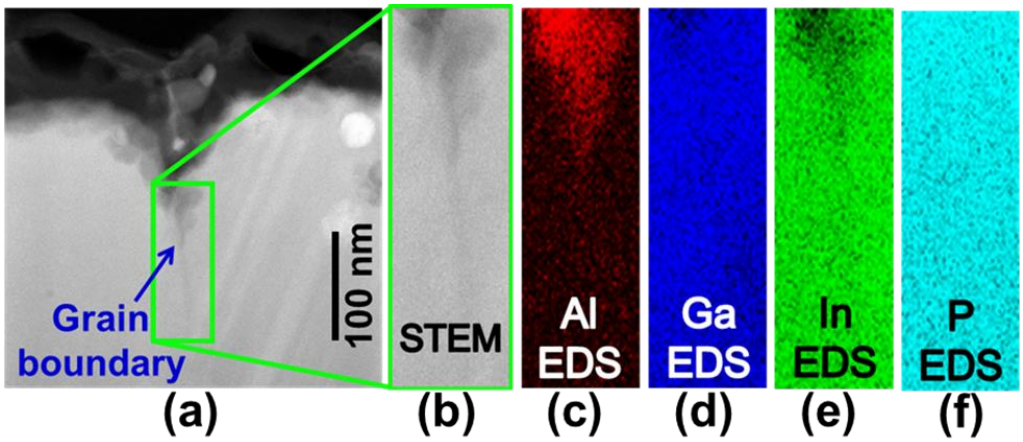

Fig. 6.14. (a, b) STEM image of GaInP after aluminum post-deposition treatment, and EDS mapping (c-f) of Al, Ga, In and P along the indicated grain boundary.

not yet confirmed the bonding of these elements to form AlGaInP after Al-PDT, only the presence of these 4 elements in the surface layer and an increase in PL photon energy that would be expected if an AlGaInP layer were present.

Although the observation of a 2.0-eV CL peak, and of PL photon energies >1.8-eV are consistent with the hypothesis of band-to-band radiative recombination in a surface layer of AlGaInP, we note that it is not the only possible structure that could give rise to higher luminescent photon energies. While surface passivation of px-GaInP with a higher bandgap AlGaInP layer may explain the increase in 1.7-eV PL after Al-PDT, a uniform AlGaInP layer at the surface with, say, a 2.0-eV bandgap, would still have an unpassivated top surface, and thus would not necessarily show a strong increase in PL at 2.0 eV. One possible explanation for this is the gradient in Al composition near the front surface of the AlGaInP region that is measured and shown in Fig. 6.13. Portions of the AlGaInP formed by Al-PDT would have higher Al content and higher bandgap as one moves toward the front surface, suppressing minority-carrier concentration and recombination near the front surface at least, thereby increasing PL intensity from the lower bandgap regions of the graded AlGaInP layer. However, the interface with GaInP on the side of the AlGaInP layer away from the front could still be a high recombination site for carriers in the AlGaInP.

In the AlGaInP layer, since this is formed by introducing a 4th element to the relatively homogeneous px-GaInP composition, there is opportunity to form regions of variable composition and bandgap. Non-uniformities in the polycrystalline AlGaInP layer near the surface may also result in grains with a higher Al composition and bandgap near the grain surface boundary than in the grain core, which would similarly increase the PL intensity at the photon energy corresponding to the grain core bandgap. In this case, minority

carriers could be confined in the grain core in 3 dimensions with high bandgap regions passivating all surfaces, resulting in the observed increase in minority-carrier concentration and PL intensity. Non-uniformity in Al composition and bandgap in the polycrystalline grain structure is also one possible explanation for our observation that the PL intensity near 2.0 eV is more variable among different samples than in the 1.6-1.8 eV range associated with the px-GaInP region. It should be noted that although 3-dimensional non-uniformity of AlGaInP composition near the surface may explain some of the experimental observations, it is presently an untested hypothesis.

During CL measurements, the cross-sectional surface of the px-GaInP is unpassivated with AlGaInP, and furthermore may have some surface damage from the process used to form the cross-sectional sample. This may suppress the 1.76-eV CL peak from the px-GaInP region in Spot 2 as shown in Fig. 6.12. The postulated, but untested, 3-dimensional non-uniformity of AlGaInP composition near the surface would allow carrier confinement in regions that still luminesce brightly as shown in Fig. 6.12, even in the presence of the unpassivated cross-sectional surface of the CL sample. Alternatively, the AlGaInP regions near the surface may be doped by the Al-PDT process, resulting in stronger CL intensity. Alternative explanations for the strong increase in PL intensity after Al-PDT as shown in Fig. 6.9 could contribute to the PL response either alone or in conjunction with formation of a wider bandgap passivation layer.

For example, Al annealing could introduce defects or impurities that increase doping in the GaInP, resulting in a marked increase in PL intensity. However, additional polycrystalline GaInP samples grown in this study with extrinsic Si *n*-type doping showed only 3× increase in PL intensity compared to not-intentionally-doped (nid) polycrystalline GaInP samples (Fig. 6.15), far less than the PL increase measured after Al-PDT. The same Si dopant flux during single-crystal GaInP growth yielded 1×10^{17} cm^{-3} n-type dopant concentration. Similarly, polycrystalline GaInP samples with Be *p*-type extrinsic doping at 8×10^{17} cm^{-3} nominal concentration showed only 2× higher peak PL intensity than nid samples.

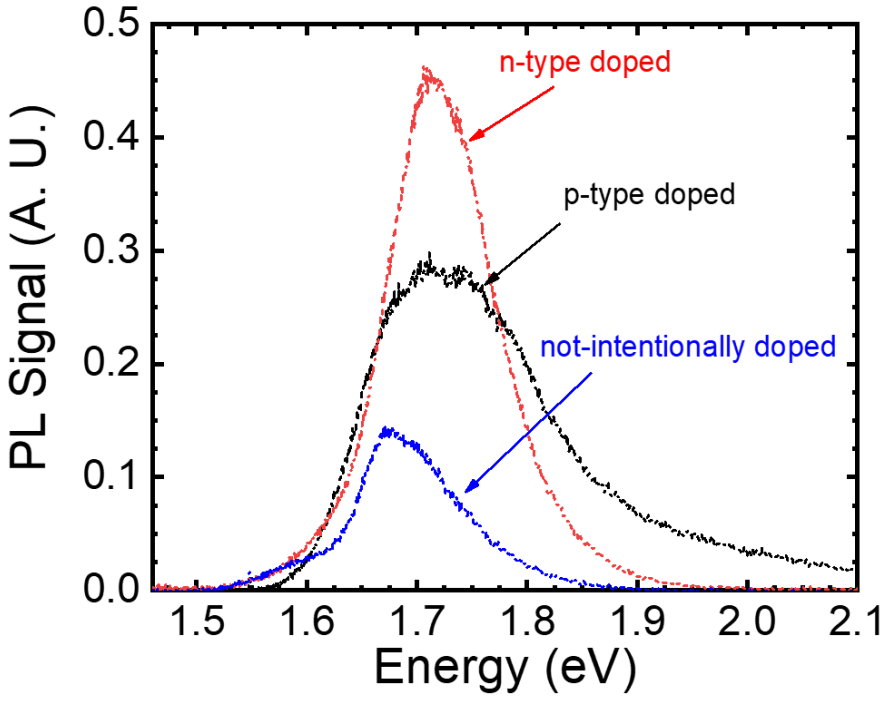

Fig. 6.15. Effect of doping poly GaInP thin film during growth on its photoluminescence response at room temperature.

In another potential mechanism for the observed increase in PL with Al-PDT, thermal annealing may help to remove defects even in the absence of Al, as long as desorption of phosphorus from the film is suppressed by a barrier film on top. To test this possibility, a SiO_2 cap was deposited by plasma-enhanced chemical vapor deposition (PECVD) on polycrystalline GaInP samples to prevent phosphorus loss from the film, and the samples were then annealed at 850°C. However, the peak PL intensity showed only a 10× increase for these samples, far less than that observed for the Al-PDT treatment.

These observations support the presence of a high-bandgap phase formed near the surface of polycrystalline GaInP resulting from Al-PDT. This phase is expected to act as a wide-bandgap passivation layer, by reducing the minority-carrier concentration and recombination at surfaces and interfaces. This would increase the overall minority-carrier lifetime and the steady-state minority-carrier concentration under illumination in the bulk region of polycrystalline GaInP grains, away from surface and grain boundary regions, and therefore increase PL emission in the grain core. When used as the absorber layer in a solar cell, the higher minority-carrier concentration in steady-state would be expected to result in higher quasi-Fermi level splitting and solar-cell voltage, increasing the conversion efficiency.

6.5. Conclusion

This study presents an investigation of polycrystalline GaInP growth and passivation. An aluminum-assisted post-deposition treatment (Al-PDT) introduced in this study for passivation of surfaces and grain boundaries in GaInP improves the minority-carrier properties. The Al-PDT of polycrystalline $Ga_{0.37}In_{0.63}P$ films with 1.7-eV bandgap results in a 90-fold increase in the peak photoluminescence, a 720-fold increase in integrated PL intensity, and an increase in time-resolved PL lifetime from <2 ns to 44 ns. This process

may also be able to be extended to other polycrystalline III-V materials. A higher-bandgap region of AlGaInP results from this Al-PDT, based on photoluminescence, cathodoluminescence, and energy dispersive X-ray spectroscopy measurements. The higher-bandgap AlGaInP regions at the film surface and near-surface grain-boundary regions are thought to suppress minority-carrier concentration at these interfaces, reducing recombination rates, and increasing the steady-state minority-carrier concentration under illumination, photoluminescence intensity, and implied open-circuit voltage in the polycrystalline GaInP films. Next steps to create solar cells from this material include characterizing n-type and p-type extrinsic doping, and contact formation to the films. Further improvements in post-deposition treatments to increase PL intensity along the path established in this study may enable polycrystalline GaInP to serve as a stable, low-cost, and environmentally benign top-cell absorber in Si-based tandem solar cells, and in other applications requiring a 1.6-2.0 eV direct gap, low-cost thin film semiconductor.

CHAPTER 7

SUMMARY AND FUTURE WORK

7.1. Contributions to knowledge

This work is the first study that has characterized the dependence of grain size, crystal structure and morphology features on growth temperature and Ga content of polycrystalline GaInP thin films. The decrease in grain size of the polycrystalline GaInP with increase in gallium content is associated with the increase in the melting point of the GaInP alloy. The crystal structure of polycrystalline GaInP thin films grown on amorphous substrate is determined to be zincblende for all the explored gallium contents between 0% and 50%. There is no evidence of phase separation in the grown polycrystalline GaInP thin films. The two binary subsystems of InP and GaP – that make up the GaInP – appear to be completely miscible within the studied range of compositions (Fig. 6.2).

Recombination properties due to electrically active grain boundaries and other defects in poly GaInP are also studied using photoluminescence spectroscopy. Changing the gallium content from 0% to 50% moves the PL peak position from 1.35eV to 1.88 eV. It is observed that the integrated PL intensity decreases beyond gallium content of 25%. No correlation is observed between other structural properties and the integrated PL peak intensity (Fig. 6.7).

To passivate the surface and grain boundary defects in poly GaInP thin films, a novel passivation method is developed and explored. The novel, low-cost aluminum-assisted post-deposition treatment (Al-PDT) is hypothesized to passivate the surface and grain boundary regions of polycrystalline GaInP by forming a high-bandgap layer near these regions, and experimental evidence is gathered and analyzed that is consistent with this

hypothesis. The Al-PDT has experimentally demonstrated a 220-fold increase in the integrated, room-temperature PL intensity, an increase in the PL peak intensity over 90-fold (Fig. 6.9). This improvement in steady state PL response is also associated with a measured increase in the minority-carrier lifetime from < 2 ns to 44 ns measured by time-resolved photoluminescence in polycrystalline GaInP thin films at 80 K (Fig. 6.11).

During the development of the Al post deposition treatment, an initial estimate of Al diffusivity in GaInP was determined (Fig. 6.13) to be $2.8 \times 10^{-15} cm^2 sec^{-1}$. This work has further explored the physical mechanism of grain boundary passivation by aluminum diffusion through grain boundaries to improve the optoelectronic response of polycrystalline GaInP.

Introduction, development, and refinement of this novel Al-PDT passivation mechanism in polycrystalline GaInP could potentially initiate the development of a new family of passivation treatments to improve the optoelectronic response of other polycrystalline compound semiconductors.

This dissertation has also explored the effect of defect characteristics at the surface, and layer properties like doping and thickness on recombination rate in GaInP-based double heterostructures. Recombination velocities measured at the GaInP surfaces after deposition of dielectric layers and measurement of recombination velocities at these surfaces guided the expectation for the performance of polycrystalline GaInP solar cells (Fig. 3.9). In the process, hole diffusivity in GaInP using photoluminescence decay method was measured to be 0.85 $cm^2 sec^{-1}$.

The marked reduction in the recombination velocity due to formation of AlInP-GaInP heterostructures in single-crystal double heterostructures is informative and illustrative of an effective passivation method that was developed for polycrystalline GaInP thin films.

7.2. Future work opportunities

Developing the understanding of the defect energy states and densities at GaInP interfaces could help to further engineer the properties of grain boundaries and surfaces in GaInP. Epitaxial growth of GaInP on polycrystalline GaAs substrates with grain size greater than 1 cm could enable study of individual grain boundaries. Estimate of defect density can be obtained by temperature dependent I-V, C-V and C-f measurements. Misorientation between grains can also help quantify the lower limit of density of dangling bonds at the grain boundaries of the epitaxially grown polycrystalline GaInP thin films.

Treating single-crystal GaInP-based double heterostructures with aluminum-assisted post deposition treatment or sulfur-based chemical baths could help quantify the effectiveness of the passivation processes by direct measurement of the change in recombination velocity of the GaInP surface.

Single-crystal GaInP and polycrystalline GaInP grown on GaAs could also be used to quantify the diffusivity of various dopants in the bulk of GaInP. This could further open opportunities to selectively dope grain boundaries of polycrystalline semiconductor compounds.

Further work needs to be carried out to form ohmic contacts to polycrystalline GaInP and incorporate the process of contact formation with the developed surface passivation processes like aluminum-assisted post-deposition treatment (Al-PDT).

Development of polycrystalline GaInP-based pn-junction with ohmic contacts would further facilitate measurement of electron and hole properties in GaInP and their interaction with interface defects. Growth of polycrystalline GaInP on metal substrates that are expected to form ohmic contacts with GaInP could facilitate the formation of a polycrystalline GaInP-based pn-diode and eventually a functional solar cell.

Moving further, hopefully, this dissertation along with the studies outlined in this section could contribute towards the realization of high-efficiency polycrystalline GaInP-based single and multijunction solar cells.

REFERENCES

[1] DRAFT Inventory of U.S. Greenhouse Gas Emissions and Sinks: 1990–2019," U.S. EPA Report, 2021.

[2] U. S. Energy Information Administration, Electric Power Monthly, February 2021.

[3] Feldman D. *et. al.*, "U. S. Solar Photovoltaic System and Energy Storage Cost Benchmark: Q1 2020,", National Renewable Energy Laboratory, 2021.

[4] J. F. Geisz, M. A. Steiner, I. Garcia, S. R. Kurtz, and D. J. Friedman, "Enhanced external radiative efficiency for 20.8% efficient single-junction GaInP solar cells," Applied Physics Letters 103, 041118 (2013).

[5] B. M. Kayes, H. Nie, R. Twist, S. G. Spruytte, F. Reinhardt, I. C. Kizilyalli, and G. S. Higashi, "27.6% Conversion efficiency, a new record for single-junction solar cells under 1 sun illumination," 37th IEEE Photovoltaic Specialists Conference Proceedings, 12710933 (2011).

[6] M. Wanlass, "Systems and methods for advanced ultra-high-performance InP solar cells," US Patent 9, 131 B1 (2017).

[7] R. Venkatasubramanian, "High efficiency GaAs solar cells on polycrystalline Ge substrates," Final Report NREL/SR-590-24820 (1998).

[8] M. Zheng, H. Wang, C. M. Sutter-fella, C. Battaglia, S. Aloni, X. Wang, J. Moore, J. W. Beeman, M. Hettick, M. Amani, W. Hsu, J. W. Ager, P. Bermel, M. Lundstrom, J. He, and A. Javey, "Thin-Film Solar Cells with InP Absorber Layers Directly Grown on Nonepitaxial Metal Substrates," Advanced Energy Materials 5, 1501337 (2015).

[9] "Epitaxial Crystal Growth: Methods and Materials," Springer Handbooks of Electronic and Photonic Materials, 2006.

[10] A. Maros, "Modeling, Growth and Characterization of III-V and Dilute Nitride Antimonide Materials and Solar Cells," Ph.D. Dissertation, Arizona State University (2017).

[11] L. Vegard, "Die Konstitution der Mischkristalle und die Raumfüllung der Atome," Z. Physik 5, 17–26 (1921).

[12] R. J. Nelson, and R. G. Sobers, "Minority carrier lifetimes and internal quantum efficiency of surface-free GaAs," Journal of Applied Physics 49, 6103 (1978).

[13] S. R. Johnson, D. Ding, J. -B. Wang, S. -Q. Yu, and Y. -H. Zhang, "Excitation dependent photoluminescence measurements of the nonradiative lifetime and quantum efficiencies in GaAs," Journal of Vacuum Sciences and Technology B:

Microelectronics and Nanometer Structures Processing, Measurements, and Phenomena 25, 1077 (2007)

[14] T. Walter, R. Herberholz, C. Müller, and H. W. Schock, "Determination of defect distributions from admittance measurements and application to Cu(In,Ga)Se_2 based heterojunctions," Journal of Applied Physics 80, 8 (1996).

[15] M. Turcu, I. M. Kotschau, and U. Rau, "Composition dependence of defect energies and band alignments in the $Cu(In_{1-x}Ga_x)(Se_{1-y}S_y)_2$ alloy system," Journal of Applied Physics 91, 3 (2002).

[16] J. T. Heath, J. D. Cohen, and W. N. Shafarman, "Bulk and metastable defects in $CuIn_{1-x}Ga_xSe_2$ thin films using drive-level capacitance," Journal of Applied Physics 95, 3 (2004).

[17] J. Dekker, A. Tukiainen, N. Xiang, S. Orsila, M. Saarinen, M. Toivonen, M. Pessa, N. Tkachenko, and H. Lemmetyinen, "Annealing of the deep recombination center in GaInP/AlGaInP quantum wells grown by solid-source molecular beam epitaxy," 86, 3709 (1999).

[18] H. J. von Bardeleben, D. Stiévenard, D. Deresmes, A. Huber, and J. C. Bourgoin, "Identification of a defect in a semiconductor: EL2 in GaAs," Physical Review B 34, 10 (1986).

[19] Z. C. Huang, C. R. Wie, J. A. Varriano, M. W. Koch, and G.W. Wicks, "Phosphorus-vacancy-related deep levels in GaInP layers," Journal of Applied Physics 77, 1587 (1995).

[20] S. B. Zhang, S. Wei, and A. Zunger, "Elements of doping engineering in semiconductors," Presented at National Center for Photovoltaics Program Review Meeting NREL/CP-590-25746 Denver, Colorado (1998).

[21] D. Colleoni, G. Miceli, and A. Pasquarello, "Fermi-level pinning through defects at GaAs/oxide interfaces: A density functional study," Physical Review B 92, 125304 (2015).

[22] W. Walukiewicz, "Fermi level dependent native defect formation: Consequences for metal–semiconductor and semiconductor–semiconductor interfaces," Journal of Vacuum Science & Technology B: Microelectronics Processing and Phenomena 6, 1257 (1988).

[23] W. Walukiewicz, "Mechanism of Fermi-level stabilization in semiconductors," Physical Review B 37, 9 (1988).

[24] D. K. Simon, P. M. Jordan, T. Mikolajick, and I. Dirnstorfer, "On the Control of the Fixed Charge Densities in Al_2O_3-Based Silicon Surface Passivation Schemes," ACS Appl. Mater. Interfaces 7, 51 (2015).

[25] V. L. Alperovich, A. G. Paulish, and A. S. Terekhov, “Domination of adatom-induced over defect-induced surface states on p-type GaA.s(Cs,o) at room temperature,” Physical Review B 50, 8 (1994).

[26] B. Gaury, Y. Sun, P. Bermel, and P. M. Haney, “Sesame: A 2-dimensional solar cell modeling tool,” Solar Energy Materials and Solar Cells 198, (2019).

[27] A. S. Gudovskikh, N. A. Kaluzhniy, V. M. Lantratov, S. A. Mintairov, M. Z. Shvarts, and V. M. Andreevab, “Numerical modelling of GaInP solar cells with AlInP and AlGaAs windows,” Thin Solid Films 20, 516 (2008).

[28] C.-S. Jiang, D. J. Friedman, H. R. Moutinho, and M. M. Al-Jassim, “Profiling the Built-In Electrical Potential in III-V Multijunction Solar Cells,” 2006 IEEE 4th World Conference on Photovoltaic Energy Conference Proceeding 1, 853 (2006).

[29] S.M. Sze, “Physics of Semiconductor Devices, 2nd Edition,” John Wiley & Sons, New-York (1981).

[30] I. Vurgaftman, J.R. Meyer, L.R. Ram-Mohan, “Band parameters for III–V compound semiconductors and their alloys,” Journal of Applied Physics 89, 5815 (2001).

[31] D. P. Bour, J. R. Shealy, G. W. Wicks, and W. J. Schaff, “Optical properties of $Al_xIn_{1-x}P$ grown by organometallic vapor phase epitaxy,” Applied Physics Letters 50, 615 (1987).

[32] S. -H. Wei and A. Zunger, “Calculated natural band offsets of all II–VI and III–V semiconductors: Chemical trends and the role of cation d orbitals,” Applied Physics Letters 72, 2011 (1998).

[33] J. Chen, J. R. Sites, and I. L. Spain, “Band offset of $GaAs/In_{0.48}Ga_{0.52}P$ measured under hydrostatic pressure,” Applied Physics Letters 58, 74 (1991)

[34] M. R. Brozel, and G. E. Stillman, “Properties of Gallium Arsenide (3rd Edition),” Institution of Engineering and Technology (1996).

[35] N. Newman, W. E. Spicer, T. Kendenlewicz, and I. Lindau, “On the Fermi level pinning behavior of metal/III–V semiconductor interfaces,” Journal of Vacuum Science & Technology B: Microelectronics Processing and Phenomena 4, 931 (1986).

[36] J. D. Dow, and R. E. Allen, “Surface defects and Fermi-level pinning in InP,” Journal of Vacuum Science and Technology 20, 659 (1982).

[37] J. M. Olson, R. K. Ahrenkiel, D. J. Dunlavy, B. Keyes, and A. E. Kibbler, “Ultralow recombination velocity at $Ga_{0.5}In_{0.5}P/GaAs$ heterointerfaces,” Applied Physics Letters 55, 1208 (1989).

[38] E. E. Perl, D. Kuciauskas, J. Simon, D. J. Friedman, and M. A. Steiner, “Identification of the limiting factors for high temperature GaAs, GaInP, and AlGaInP solar cells from device and carrier lifetime analysis,” Journal of Applied Physics 122, 233102 (2017).

[39] K. Domen, M. Kondo, and N. Tanahashi, “Gallium Arsenide and Related Compounds,” Institute of Physics Conference Series Bristol and Philadelphia 129, (1992).

[40] X. H. Zhang, S. J. Chua, and W. J. Fan, “Band offsets at GaInP/AlGaInP(001) heterostructures lattice matched to GaAs,” Applied Physics Letters 73, 1098 (1998).

[41] R. R. King, J. H. Ermer, D. E. Joslin, M. Haddad, J. W. Eldredge, N. H. Karam, B. Keyes, and R. K. Ahrenkiel. “Double heterostructures for characterization of bulk lifetime and interface recombination velocity in III-V multijunction solar cells,” 2nd World Conference on Photovoltaic Solar Energy Conversion, Vienna, Austria (1998).

[42] M. Boulou and D. Bois, "Cathodoluminescence Measurements of the Minority-Carrier Lifetime in Semiconductors," Journal of Applied Physics 48, 4713 (1977).

[43] W. K. Metzger, D. Albin, M. J. Romero, P. Dippo, and M. Young, “CdCl2 Treatment, S Diffusion, and Recombination in Polycrystalline CdTe,” Journal of Applied Physics 99, 103703 (2006).

[44] C. Li, Y. Wu, J. Poplawsky, T. J. Pennycook, N. Paudel, W. Yin, S. J. Haigh, M. P. Oxley, A. R. Lupini, M. Al-Jassim, S. J. Pennycook, and Y. Yan, “Grain-Boundary-Enhanced Carrier Collection in CdTe Solar Cells,” Physical Review Letters 112, 1 (2014).

[45] I. Visoly-fisher, S. R. Cohen, D. Cahen, I. Visoly-fisher, S. R. Cohen, and D. Cahen, “Direct Evidence for Grain-Boundary Depletion in Polycrystalline CdTe from Nanoscale- Resolved Measurements Direct Evidence for Grain-Boundary Depletion in Polycrystalline CdTe from Nanoscale-Resolved Measurements,” Appl. Phys. Lett. 82, 556 (2015).

[46] B. E. McCandless, and S. Rykov, “Cross-section potential analysis of CdTe/CdS solar cells by kelvin probe force microscopy,” 33rd IEEE Photovoltaic Specialists Conference Proceeding (2008)

[47] J. D. Cohen, J. T. Heath, and W. N. Shafarman, “New Junction Capacitance Methods for the Study of Defect Distributions and Carrier Properties in the Copper Indium Diselenide Alloys,” Materials Research Society Symposium Proceeding 763, 1 (2003).

[48] H. Wang, C. M. Sutter-fella, P. Lobaccaro, M. Hettick, M. Zheng, D. Lien, D. W. Miller, C. W. Warren, E. T. Roe, M. C. Lonergan, H. L. Guthrey, N. M. Haegel, J.

W. Ager, C. Carraro, R. Maboudian, J. He, and A. Javey, “Increased Optoelectronic Quality and Uniformity of Hydrogenated p-InP Thin Films,” Chemistry of Materials 28 (2016).

[49] C. J. Keavney, V. E. Haven, S. M. Vernon, “Emitter Structures in MOCVD InP solar cells,” 21st IEEE Photovoltaic Specialist Conference Proceeding 1, 141 (1990).

[50] H. Burkhard, H. W. Dinges, E. Kuphal, H. Burkhard, H. W. Dinges, and E. Kuphal, “Optical properties of $In_{(1-x)}Ga_{(x)}P_{(1-y)}As_{(y)}$, InP, GaAs, and GaP determined by ellipsometry,” Journal of Applied Physics 53, 1 (1982).

[51] R. Kapadia, Z. Yu, M. Hettick, J. Xu, M. S. Zheng, C. Y. Chen, A. D. Balan, D. C. Chrzan, and A. Javey, “Deterministic nucleation of InP on metal foils with the thin-film vapor-liquid-solid growth mode,” Chemistry of Materials 26, 3 (2014).

[52] R. Kapadia, Z. Yu, H. H. Wang, M. Zheng, C. Battaglia, M. Hettick, D. Kiriya, K. Takei, P. Lobaccaro, J. W. Beeman, J. W. Ager, R. Maboudian, D. C. Chrzan, and A. Javey, “A direct thin-film path towards low-cost large-area III-V photovoltaics,” Scientific Reports 3, 2275 (2013).

[53] M. Zheng, K. Horowitz, M. Woodhouse, C. Battaglia, R. Kapadia, and A. Javey, “III-Vs at scale : a PV manufacturing cost analysis of the thin film vapor–liquid–solid growth mode,” Progress in Photovoltaics: Research and Applications 24, (2016).

[54] R. Baier, C. Leendertz, M. C. Lux-steiner, and S. Sadewasser, “Toward Quantitative Kelvin Probe Force Microscopy of Nanoscale Potential Distributions,” Physical Review B 85, 165436 (2012).

[55] Y. Hishikawa, E. D. Dunlop, M. A. Green, J. Hohl, E. Anita, W. Y. H. Baillie, and D. H. Levi, “Solar Cell Efficiency Tables (Version 52),” Progress in Photovoltaics 26, 427 (2018).

[56] P. T. Erslev, J. Lee, G. M. Hanket, W. N. Shafarman, and J. D. Cohen, “The electronic structure of $Cu(In_{1-x}Ga_x)Se_2$ alloyed with silver,” Thin Solid Films 519, 21 (2011).

[57] J. D. Cohen, J. T. Heath, and W. N. Shafarman, “New Junction Capacitance Methods for the Study of Defect Distributions and Carrier Properties in the Copper Indium Diselenide Alloys,” Materials Research Society Symposium Proceeding 763, 1 (2003).

[58] R. Herberholz, M. Igalson, and H. W. Schock, “Distinction between Bulk and Interface States in $CuInSe_2$/CdS/ZnO by Space Charge Spectroscopy,” Journal of Applied Physics 83, 318 (1998).

[59] G.L. Gurevich, and A.K. Tagantsev, “Intrinsic dielectric loss in crystals,” Advances in Physics 40 (1991).

[60] A. Chikhalkar, C. Zhang, N. Faleev, C. Honsberg, and R. R. King, "Passivation of polycrystalline $Ga_{0.37}In_{0.63}P$ – an emerging 1.7 eV bandgap top cell candidate," Proc. IEEE 45th Photovoltaic Specialists Conf. and 7th World Conference on Photovoltaic Energy Conversion, Waikoloa, HI (2018).

[61] W.A. Rachinger, "A Correction for the α1 α2 Doublet in the Measurement of Widths of X-ray Diffraction Lines," Journal of Scientific Instruments 25, (1948) doi: 10.1088/0950-7671/25/7/125.

[62] S. Jung, S. Ahn, J.H. Yun, J. Gwak, D. Kim, and K. Yoon, "Effect of Ga contents on properties of CIGS thin films and solar cells fabricated by co-evaporation techniques," Current Applied Physics 10 (2010).

[63] P. M. Shafi, and A. C. Bose, "Impact of crystalline defects and size on X-ray line broadening: A phenomenological approach for tetragonal SnO_2 nanocrystals," AIP Advances 5 (2015) doi:10.1063/1.4921452.

[64] W. Zhang, X. Zeng, X. Su, X. Zou, P.-A. Mante, M.T. Borgström, and A. Yartsev, "Carrier Recombination Processes in Gallium Indium Phosphide Nanowires," Nano Letters 17 (2017) doi: 10.1021/acs.nanolett.7b01159.

[65] V. Dagytė, M. Heurin, X. Zeng, and M. T. Borgström, "Growth kinetics of $Ga_xIn_{(1-x)}P$ nanowires using triethylgallium as Ga precursor," Nanotechnology. 29 (2018) doi: 10.1088/1361-6528/aad1d2.

[66] S. P. Harvey, G. Teeter, H. Moutinho, M. M. Al-Jassim, "Direct evidence of enhanced chlorine segregation at grain boundaries in polycrystalline CdTe thin films via three-dimensional TOF-SIMS imaging: Chlorine segregation at grain boundaries in CdTe thin films," Progress of Photovoltaics: Research and Applications 23 (2015) doi:10.1002/pip.2498.

[67] L. A. Verhoef, P. Michiels, W. C. Sinke, C. M. M. Denisse, M. Hendriks, and R. J. C. van Zolingen, "Combined impurity gettering and defect passivation in polycrystalline silicon solar cells," Applied Physics Letters 57 (1990) doi:10.1063/1.103805.

[68] O. Schultz, S. W. Glunz, S. Riepe, and G. P. Willeke, "High-efficiency solar cells on phosphorus gettered multicrystalline silicon substrates," Progress in Photovoltaics: Research and Applications 14 (2006) doi:10.1002/pip.736.

[69] A. Chari, P. de Mierry, A. Menikh, and M. Aucouturier, "Impurity-defect interaction in polycrystalline silicon for photovoltaic applications : the role of hydrogen," Revue de Physique Appliquée 22 (1987) doi: 10.1051/rphysap:01987002207065500.

[70] C. H. Seager, and D. S. Ginley, "Passivation of grain boundaries in polycrystalline silicon," Applied Physics Letters 34 (1979) doi: 337–340. doi:10.1063/1.90779.

[71] O. Nast, S. Brehme, S. Pritchard, A. G. Aberle, and S. R. Wenham, “Aluminium-induced crystallisation of silicon on glass for thin-film solar cells,” Solar Energy Materials and Solar Cells 65, 1-4 (2001). doi: 10.1016/S0927-0248(00)00117-3

[72] I. Chambouleyron, F. Fajardo, and A. R. Zanatta, “Aluminum-induced crystallization of hydrogenated amorphous germanium thin films,” Applied Physics Letters 79 (2001) doi:10.1063/1.1415772.

[73] C. J. Sandroff, M. S. Hegde, L. A. Farrow, C. C. Chang, and J. P. Harbison, “Electronic passivation of GaAs surfaces through the formation of arsenic—sulfur bonds,” Applied Physics Letters 54 (1989) doi:10.1063/1.101451.

[74] B. A. Kuruvilla, S. V. Ghaisas, A. Datta, S. Banerjee, and S. K. Kulkarni, “Passivation of GaAs (100) using selenium sulfide,” Journal of Applied Physics 73 (1993) doi: 4384–4387. doi:10.1063/1.352775.

[75] V. N. Bessolov, E. V. Konenkova, and M. V. Lebedev, “A comparison of the effectiveness of GaAs surface passivation with sodium and ammonium sulfide solutions,” Physics of the Solid State 39 (1997) doi:10.1134/1.1129831.

[76] N. Newman, W. E. Spicer, and E. R. Weber, “Mechanism for annealing-induced changes in the electrical characteristics of Al/GaAs and Al/InP Schottky contacts,” Journal of Vacuum Science and Technology B: Microelectronics Processing and Phenomena 5, 1020 (1987).

[77] J. C. Fisher, “Calculation of Diffusion Penetration Curves for Surface and Grain Boundary Diffusion,” Journal of Applied Physics 22 (1951) doi:10.1063/1.1699825.

[78] R. K. Ahrenkiel, and S. W. Johnston, "An optical technique for measuring surface recombination velocity," Solar Energy Materials and Solar Cells 93 (2009).

[79] K. J. Beernink, D. Sun, D. W. Treat, and B. P. Bour, “Differential Al–Ga interdiffusion in AlGaAs/GaAs and AlGaInP/GaInP heterostructures,” Applied Physics Letters 66, 3597 (1995).